ANALYSIS AND TESTING OF A THUNDER™ PIEZOELECTRIC ACTUATOR AS A PRIME MOVER IN A GAS FLOW CONTROL VALVE

by

Jesse Cemil Rodgers

BS in Mechanical Engineering, University of Pittsburgh, 1999

Submitted to the Graduate Faculty of

School of Engineering in partial fulfillment

of the requirements for the degree of

Master of Science in Mechanical Engineering

University of Pittsburgh

2005

UNIVERSITY OF PITTSBURGH

SCHOOL OF ENGINEERING

This thesis was presented

by

Jesse Cemil Rodgers

It was defended on

January 10, 2005

and approved by

Dr. Jeffrey Vipperman, Associate Professor, Dept. of Mechanical Engineering

Dr. Roy Marangoni, Associate Professor, Dept. of Mechanical Engineering

Thesis Advisor: Dr. William Clark, Professor, Dept. of Mechanical Engineering

ANALYSIS AND TESTING OF A THUNDER™ PIEZOELECTRIC ACTUATOR AS A PRIME MOVER IN AN GAS FLOW CONTROL VALVE

Jesse Cemil Rodgers, MS

University of Pittsburgh, 2005

The target of this research was to conduct an experimental analysis in which a THUNDER™ (Thin Unimorph DrivER) actuator was used to adjust the flow of air through a specified cross sectional area inside a Plexiglas housing. The THUNDER™ actuator was developed over ten years ago as a high displacement piezoelectric actuator. It is a curved, bilayer actuator made up of a piezoelectric layer (PZT, lead zirconate titanate) and a stainless steel layer. In this study, the THUNDER™ is the prime mover in an air flow control valve. The valve is made up of a flow channel that allows air to pass over the top of the actuator. When voltage is applied to the actuator, causing the piezoceramic layer to expand or contract, the curvature of the actuator changes, thus changing the orifice area in the valve and causing a change in flow. Testing is done with single and dual flow loop arrangements. In the dual flow loop, one flow line contains the control valve while the other is a bypass line. The valve is used to balance flow between the lines. Both lines have adjustable outlet valves so that the valve can be tested under a wide range of flow conditions. Pressure transducers were placed along the experimental setup to observe various pressures conditions in the system. Two flow meters were used to measure either the single loop flow rate or the corresponding flow rate in each line of the dual flow loop. Several lids for the control valve were manufactured and tested to reveal that alternative channel

geometries could lead to increased performance over a specific range. The test results showed that the THUNDER™ control valve could modulate the air flow by as much as 16% at 4.4 SCFM (125 LPM) in single loop flow and 30% at 2.3 SCFM (65 LPM) in dual loop flow for inlet pressures up to 25 PSI (172 kPa).

TABLE OF CONTENTS

LIST OF TABLES

LIST OF FIGURES

ACKNOWLEDGEMENTS

I would like to thank Dr. Clark for his guidance during my term as a graduate student. We have known each other a long time and I look forward to the future working together.

I would like to thank my family, especially my brother Jeffrey, who has joined me for the quest of higher learning among siblings. Thank you.

1.0 INTRODUCTION

The objective of this research was to create a valve actuated by a piezoelectric actuator in a gas flow line to modulate the flow rate about a nominal value. The motivation for this work stems from applications in the energy industry in which a single gas source feeds multiple flow lines that must provide balanced flow during operation. Since such a setup is difficult to achieved with a fixed design, it is desirable to incorporate an electrically controllable valve in each line that allow a nominal flow in it's "off" state, but which can adjust the flow by a preset percentage of nominal. In this application, the gal is to provide ± 20% change in the nominal flow.

After analyzing commercially available flow control valves and their different modulation techniques, an alternate valve design was developed and tested, which is the primary focus of this thesis. Moreover, research on current piezoelectric valves that could be incorporated into a flow modulation environment was completed. In order to satisfy the need for a piezoelectric control valve, one was created and its performance tested to its highest range limited by the performance of the actuator. Test conditions were limited to room temperature and 25 pounds per square inch (PSI) or 172 kiloPascal (kPa) gas inlet pressure. Further implementation into harsher environments found in the energy industry, such as higher temperatures and larger flows will require future testing.

As described in the thesis, two different flow loops were used to test the valve. A single flow loop (single gas line with a piezoelectrically controllable valve) was used to determine baseline performance of the valve. To assess the ability to modulate and balance the flow in

multiple lines, a dual flow loop arrangement was used in which a single source fed two separate flow paths, one of which contained the test valve.

It was determined early in the project that the ± 20% modulation condition required the use of a high stroke actuator in the valve. One of the highest deflecting piezoelectric actuators today is the THUNDER™ actuator manufactured by Face, Inc. Figure 1 shows THUNDER™ actuators, are 5 layer unimporh actuators. The actuator has inherent mechanical advantage due to its curved surface resulting from cooling during manufacturing. This is an excellent actuator to consider since the actual thickness of the THUNDER™ is considerably less than that of a piezoelectric stack and the stroke available for modulating flow is much greater. There have been many devices that have made use of the THUNDER™ actuator; however it has not been implemented into a control valve for flow applications. This thesis incorporates the THUNDER™ actuator into a valve design.

The operating parameter for testing the control valve consisted of air inlet pressures up to 25 PSI (172 kPa) and volumetric flow rates up to 368 standard liters per minute (SLPM) or 13 standard cubic feet per minute (SCFM). The results showed the THUNDER™ actuator moving as much as 0.49mm (0.02 in), which produced flow variations by as much as 16% in single loop flow and 30% under dual flow loop conditions.

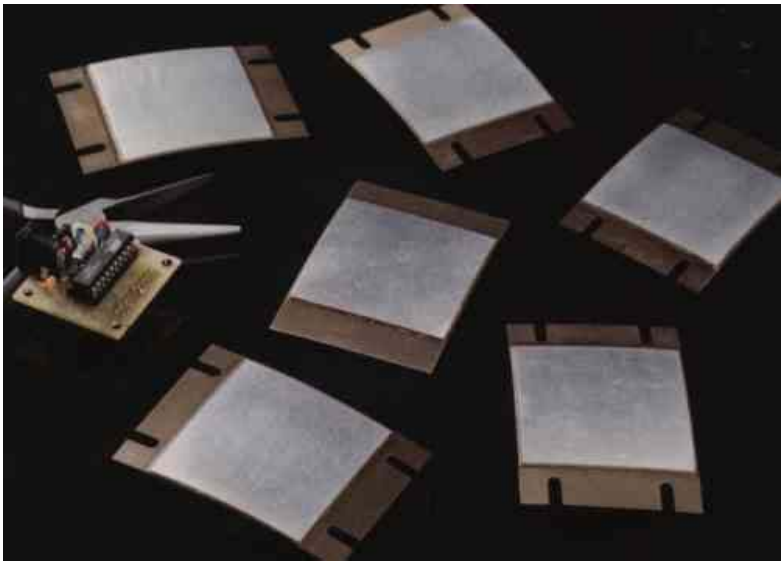

Figure 1. An array of THUNDER™ actuators (Face Co., 2004).

This thesis presents a literature review dealing with current prime movers in flow control valves as well as piezoelectricity and its applicability. The literature review will also cover current commercial piezoelectric gas flow control valves as well as the THUNDER™ actuator and past implementations. The experimental setup followed by results to show the gas control valve's performance in a variety of conditions. A discussion of each result section will follow with conclusions and future work to conclude.

2.0 LITERATURE SURVEY

The literature review is divided into four sections. The first section covers various valve configurations used for flow control. The second section provides information on the area of piezoelectricity since the THUNDER™ is a piezoelectric actuator in the control valve. The 3rd section covers current valve assemblies for flow control using piezoelectric actuated prime movers. Finally a summary focusing on the THUNDER™ actuator from its initial production to researched implementations will be presented.

2.1 FLOW CONTROL

Valves that regulate the flow or pressure of a fluid are called flow control valves. Control valves normally respond to signals generated by independent devices such as flow meters, temperature gauges, or limit switches. Control valves are normally fitted with actuators or positioners. Pneumatically actuated globe valves are widely used for control purposes in many industries, although quarter turn types such as ball and butterfly valves may be used. Table 1 summarizes various types of valves used for flow control along with their representations in Figure 2.

Table 1. Various valves used for flow control.

a. Needle Valves	e. Gate Valve
b. Ball Valves	f. Angle Valve
c. Butterfly Valves	g. Swing Check Valve
d. Globe Valves	h. Disc Valve

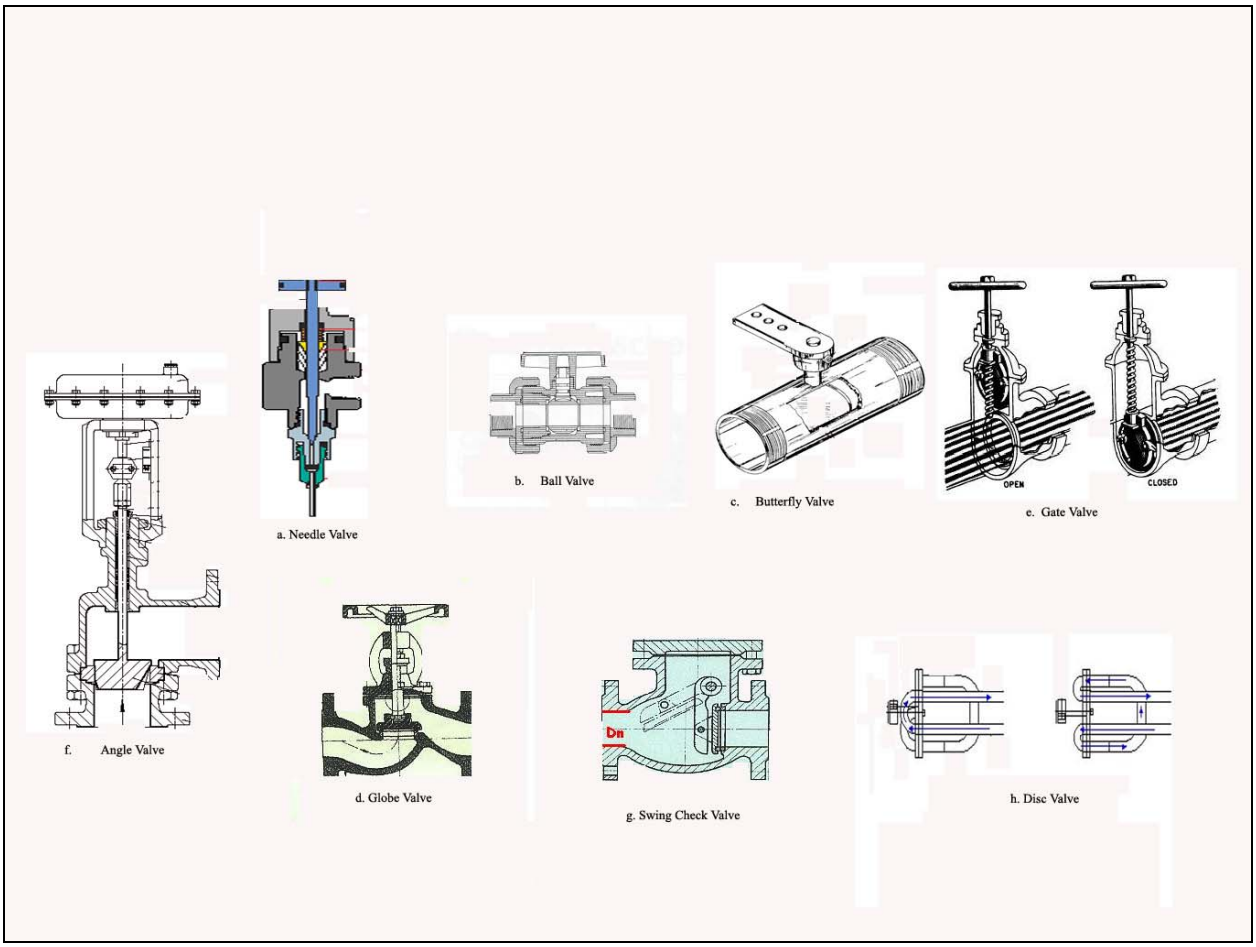

Figure 2. Various valves used for flow control (White 1996).

There are a variety of ways to actuate a control valve; however selecting the correct modulating orifice technique is important when one is dealing with actuators that compromise

force output to achieve their displacements. Another important characteristic of flow control valves is their ability to control a certain magnitude of modulation. For example a flow valve whose minimum flow rate is some nominal value will require much less force to close than a shut-off valve since a higher force is needed to push against the inlet pressure over a seal at the point of shut off. Thus less force is needed to modulate flow than to fully restrict it.

2.2 PIEZOELECTRICTY

The actuator is the modulating part of a control valve. It is the method by which the orifice area of the valve is fluctuated. In the valve design presented here, the THUNDER™ will be the actuator and will form part of the orifice. A search was completed for various types of valves containing piezoelectric actuation. Before discussing piezoelectric control valves, the realm of piezoelectric actuation must be interpreted. This is necessary in order to understand the overall behavior of the prime mover for the proposed control valve.

In the late 1800's, Pierre and Jacque Curie discovered that specific crystalline materials, when compressed, produced a voltage proportional to the applied pressure and that when an electric field is applied across the material, there is a corresponding change in shape (Electro-Ceramic, 2004). It is this characteristic that is called piezoelectricity. The characteristic was also referred to as pressure electricity. Moreover, the word Piezo is the Greek word for pressure.

Piezoelectric ceramics respond very rapidly to changes in the input voltage. Although high voltages are used to produce the piezoelectric effect, power consumption is low, and energy consumption is minimal in maintaining a fixed position with a fixed load. Although

piezoelectricity is found in several types of natural materials, most modern devices use polycrystalline ceramics such as lead zirconate titanate (PZT).

A material that has piezoelectric properties outputs electrical charge when mechanical stress is applied. This is commonly known as the generator or sensor effect. The reverse effect is exhibited when a mechanical stress is produced from an applied electric field also known as the motor or actuator effect.

Natural materials that have these properties are quartz and tourmaline. Some others are also manufactured materials known as Rochelle salt, ammonium dihydrogen phosphate (ADP) and lithium sulphate (LH). Moreover, current research companies are manufacturing their own piezoelectric ceramics materials. Current man made piezoelectric ceramics are barium titanate, lead zirconate titanate (PZT), and metaniobate.

These ceramic parts can be manufactured in a variety of shapes such as bars, plates, discs, rings, and cylinders. The formed parts are then bisque fired at low temperatures in order to drive off the binders and provide some mechanical strength. The second firing completes the mechanical bonding of the constituent material. Electrodes are applied to the desired surfaces. A final firing bonds the electrode material to the ceramic surfaces.

Activation of the piezoelectric ceramic properties on a macroscopic level occurs during the “poling” process. Poling occurs by applying a strong dc electric field. The piezoelectric dipoles will tend to align themselves parallel to the direction of the electric field, so that the material will have a permanent residual polarization as seen in Figure 3. After removal of the voltage the crystal structure is aligned along the dipoles and deformation can now occur along those lines with an applied voltage.

Piezoelectric materials are used in variety of common modern devices. They are used in telephones as the ringing mechanism, speakers as the driving mechanism for sound, electronic frequency modulators, flame igniters to create a spark for ignition, energy harvesting systems by converting mechanical energy to electrical, and ultra fine optic assemblies as the actuation mechanism for nanometer positioning devices.

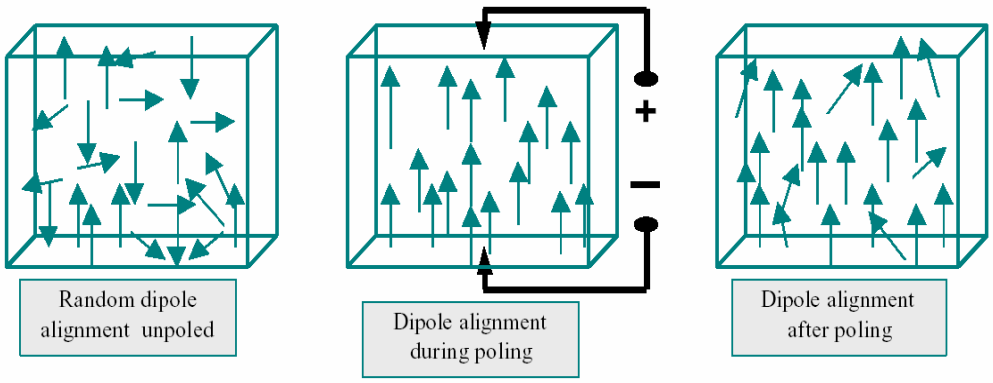

Figure 3. Poles in a piezoelectric material (Face Co., 2004).

A piezoelectric stack is composed of many layers of densely packed piezoelectric wafers separated from each other with thin layers of insulation. Figure 4 is a stack configuration where the displacement is the summation of the motion from each layer. Piezoelectric actuators can produce large forces and are used for high frequency applications. Some actuators are also known for their high stroke capabilities; however a decrease in stroke results if there is a load applied to the actuator. A decrease in stroke also occurs at higher frequency operations. Figure 5 shows the performance the THUNDER™ actuator compared to various other types of piezoelectric actuators. The THUNDER™ is the highest deflecting piezoelectric actuator; however its force characteristics are sacrificed in order to achieve the maximum displacement magnitude. Figure 6 shows a diagram of force-displacement characteristic of the THUNDER™ 5C actuator. Notice that as force is applied onto the piezoelectric ceramic, the ability to displace

is restricted due to loss of energy trying to maintain its form. Thus more voltage is required for a higher force-displacement point. If a piezoelectric ceramic becomes de-poled, the layer loses it's ability to deform because the crystal structure becomes misaligned. Figure 6 presents a working line, which shows a linear relationship between the force and displacement. Notice that the families of curves is broken up in terms of voltage applied per mil, which corresponds to the thickness of the ceramic. If operating along any line, force or displacement, either characteristic is sacrificed in order to gain the other.

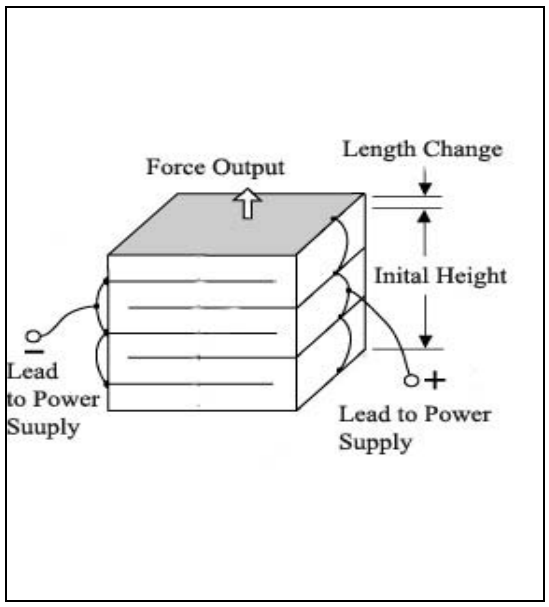

Figure 4. A piezoelectric stack actuator (Piezo Systems, 2004).

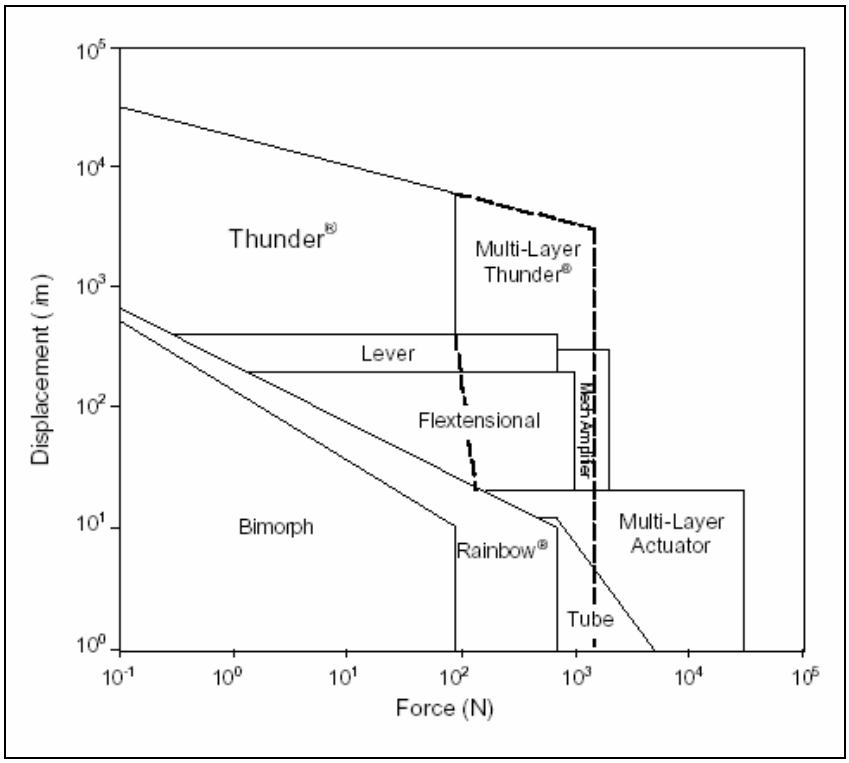

Figure 5. Displacement vs. force chart for various types of piezoelectric actuators (Dynamic Structure and Materials, 2004).

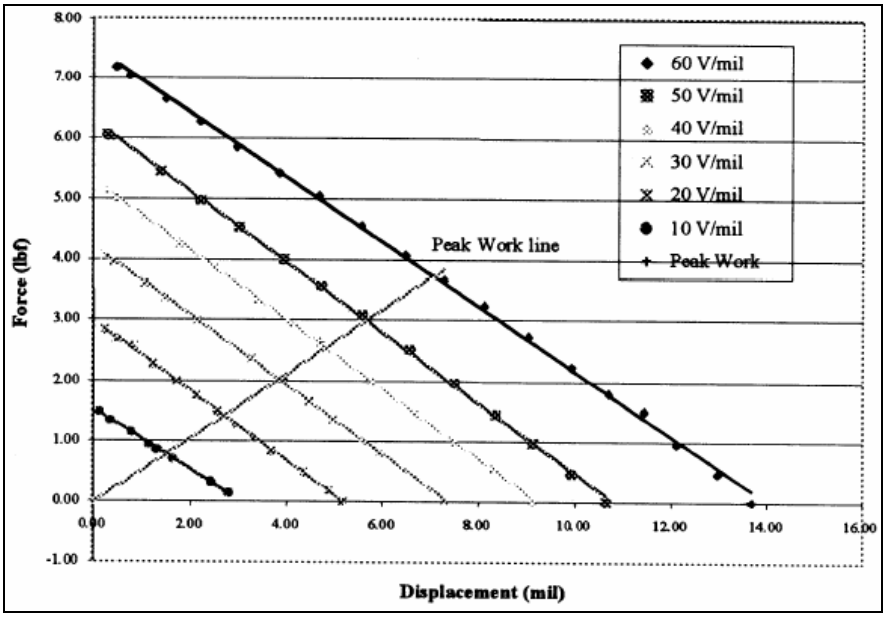

Figure 6. Displacement vs. force diagram of a piezoelectric actuator (Dynamic Structures and Materials, 2004).

2.3 PIEZOELECTRIC FLOW CONTROL VALVES

Piezoelectric valves have been considered for their quick response in fuel injection systems. This research determines the modulation in flow using static control instead of dynamic. Static control for each trial was obtained when the actuator was displaced a certain amount from a steady input voltage without the influence of frequency. Dynamic control, for example, would have involved driving the input voltage to actuate the actuator some at some frequency.

Some examples of piezoelectrically actuated flow control valves that exhibit a feedback control loop are starting to arise in of the literature (Li, 2002 and Lowrey, 2004). However since they are complex systems, differences originate, from the entire flow loop setup to the data acquisitioning technique, thus valves instead of systems were researched.

Maxtek, Incorporated has built, tested, and are distributing a piezoelectric actuated airflow control valve as seen in Figure 7 (Maxtek, 2004). This valve has a small footprint but it can only modulate air up to 1.4 SLPM (0.05 SCFM). The valve handles pressure up to 50 PSI (345 kPa). This valve was particularly useful to analyze how piezoelectric valves in the commercial market are manufactured. In addition, the orifice mechanism is shown in Figure 8 to show how small deflections in a ceramic can modulate flow. (Maxtek, 2004). This valve was particularly useful in that it could be adjusted to modulate flows to a higher degree at lower flows by adjustment of screw located at the bottom of the housing in Figure 8. When the preload is alleviated, by unscrewing the adjustment to relax the compression of the spring, the valve can achieve a higher flow rate, however the manufacturer strongly suggests not to do so in that the

piezoelectric bender element could become cracked or damaged from vibrations caused by the Teflon ball during operation.

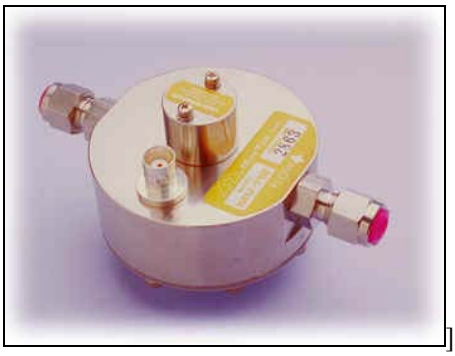

Figure 7. Photo of Maxtek's MV-112 piezoelectric flow control valve (Maxtek, 2004).

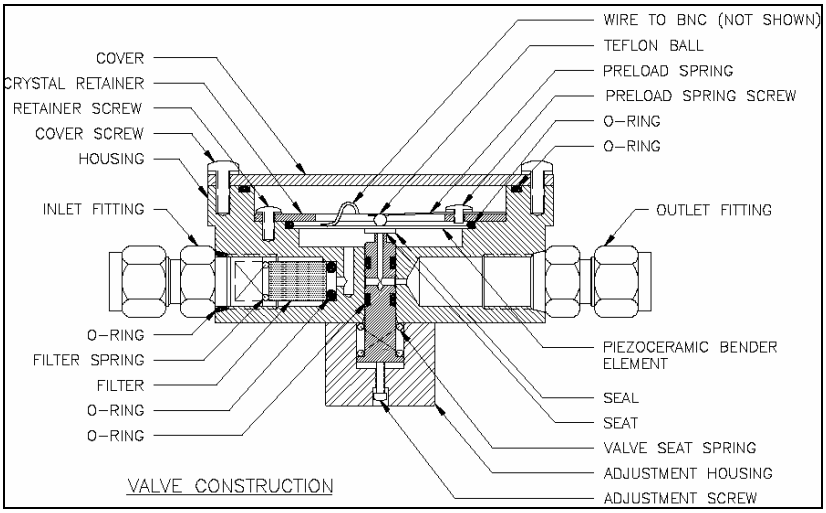

Figure 8. Drawing of Maxtek's MV-112 piezoelectric flow control valve(Maxtek, 2004).

Lee has created a piezoelectric air gas control valve operating up to 206.8 kPa or 30 PSI (Lee, 2004). At a smaller footprint than Maxtek's valve, Lee's valve (LFPA) operates up to 0.14 SLPM (0.005 SCFM), which are much lower flow regimes. To vary the valve's flow, a continuous voltage must be applied. The LFPA Series valve operates as an analog flow control device. Applied voltages vary between 80 Volts and -80 Volts, where the positive voltage

corresponds to opening the valve and negative voltage corresponds to closing the valve. The valve operates by completely shutting off the flow and then opening until the point at which the maximum specific flow rate is obtained.

Cedrat Technologies have created piezoelectric actuator using flexure amplification as seen in Figure 9 (Bouchilloux, 2002). Cedrat's flextensional design also allows for flow rates up to 17.8 SLPM (0.63 SCFM) and pressure inlets to 103.4 kPa (15 PSI). Cedrat's valve was attractive for the energy application by having the modulation mechanism and actuator based in a gas environment.

Table 2 summarizes the various commercial valves that were found. Thus by implementing a THUNDER™ actuated control valve, a new control valve using one actuator that could handle larger flows of 368.1 SLPM (13 SCFM) would be useful for the research in gas flow control valves. Since the THUNDER™ deflects the most and already has a curved form; it can be used as the actuator for the flow mechanism in a control valve.

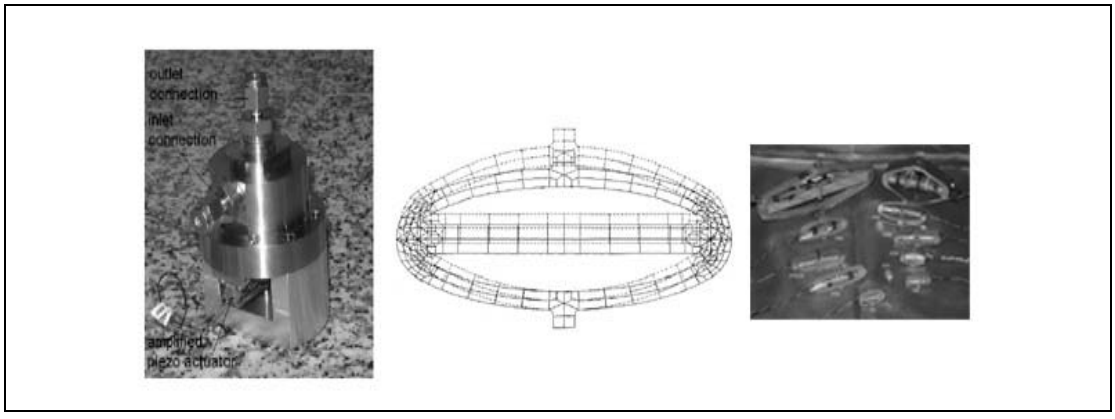

Figure 9. Amplified piezoelectric actuated flow control valve (Cedrat Technologies, 2004).

Table 2. Summary of commercial piezoelectric flow valves.

Valve	Footprint Size	Flow Range	Operating Pressure
Maxtek, Inc.	69.85 mm Diameter by 12.7 mm Length (2.75 inch Diameter by 0.5 inch Length)	1.4 SLPM (0.05 SCFM)	344.7 kPa (50 PSI)
Lee Co.	16.0 mm Diameter by 25.4 mm Length (0.63 inch Diameter by 1 inch Length)	0.14 SLPM (0.005 SCFM)	206.8 kPa (30 PSI)
Cedrat, Tech	63.5 mm Diameter by 76.2 mm Length (2.50 inch Diameter by 3 inch Length)	17.8 SLPM (0.63 SCFM)	103.4 kPa (15 PSI)

2.4 THE THUNDER™ ACTUATOR

The THUNDER™ actuator was developed in 1995 (Hellbaum et al, 1995). It originated from research completed on Rainbow Actuators (Haertling, 1994). The Thin-Layer Composite-Unimorph Piezoelectric Driver and Sensor was introduced as the highest deflecting piezoelectric actuator available. In addition to its mechanical behavior, the advantages of using the THUNDER™ include a tougher, more durable, lower voltage operation, low to moderate mechanical load capacity actuator with a low cost.

THUNDER™ actuators are manufactured by binding a thin layer of piezoelectric ceramic under hydrostatic pressure between a metal substrate and an aluminum electrode at 320° C or 608 °F (Face, 2004). The layers of the actuator can be seen in Figure 10.

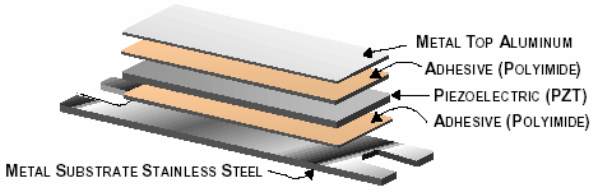

Figure 10. The THUNDER™ 8R construction (Face Co., 2004).

Prior to assembly, as shown in Figure 10, the THUNDER™ components are flat, but after assembly and allowed to cool to room temperature, the actuator's surface becomes curved as shown in Figure 11. The cooling process causes this because of the difference in the coefficients of thermal expansion between the layers thus resulting in a shallow dome shape (Ashford, 2002). The fabrication is completed after cooling by poling the ceramic in the direction perpendicular to its length as discussed in section 2.2, and shown in Figure 3.

Figure 11. The THUNDER™ 8R at room temperature with leads attached.

The actuator behaves in such a way that when voltage is applied, the actuator will flatten. When the polarity is switched on the applied voltage, the actuator will rise. The amount of deformation is directly dependent on the boundary conditions applied to the THUNDER™.

If a load is applied to the top of the actuator, the actuator will act like a spring and deflect under the load. In this thesis, the air pressure acting on the valve will be the load the actuator has to act against. As will be shown, the pressure restricts the valve's ability to modulate flow.

THUNDER™'s have been implemented into many systems, as discussed throughout the literature. Airplane wing simulations have been completed using the THUNDER™ actuator to alter airfoil trajectories (Pinkerton and Moses, 1997). Implementing the THUNDER™ into stretch tuning of optical fibers has been analyzed (Allison et al, 2000). THUNDER™'s have also been used to modify the geometry of membranes for biomedical testing (Clark and Wang, 2000, NASA, 2002). Moreover, active vibration isolation using THUNDER™'s has been investigated as well (Cheng et al, 2002).

At low frequencies, below the resonant frequency, THUNDER™ devices are capable of providing high displacements and forces of 0.30 inches (7.6 mm) and 30 lb-f (133 N) respectively (Face, 2004). Special caution should be taken when operating around resonance because large amplitudes of vibration could cause damage to the actuator. At frequencies above the resonant frequency, the THUNDER™ cannot be damaged and will continue to perform at levels less than or equal to that of the lower frequency operation (Mossi, 2002).

Therefore the applicability of the THUNDER™ in a flow valve is very appealing for its low cost, large stroke, low to moderate force, and its ability to be inserted into the chamber as both the actuator and the modulating mechanism in small valve incorporated into a high pressure air flow system. Doing so creates a potential mechanism for a gaseous control valve.

In addition to experimental testing, there was an interest in modeling the valve. One previous work in which the THUNDER™ actuation was modeled for various boundary conditions was found to be useful (Weinman, et al 2001). The Weinman model assumes perfect

linearity between voltage and deflection, thus at high drive levels of -200 to +400 volts, the model diverges significantly from measured experimental results. However, the model does not take into account forces acting on the surface; it only takes into account the THUNDER™'s material properties and the conditions at which the ends of the actuator are constrained.

Many articles in the literature present models to predict the shape of the THUNDER™ as a function of applied voltage (Hyer and Jilani, 1998, Mossi and Bishop, 1999). Models predicting the central axis dome height after the cooling phase of production were completed (Capozzoli et al, 2000 and Hyer and Jilani, 2004) as was a model top to predict height for various boundary conditions (Smith and Ouanies, 1999). Also models to approximate the central axis dome height using a change in the radius of the actuator were completed as well as dome height variations from applied voltages (Capozzoli et al, 1998, Hyer and Jilani, 2004). However there is not a model available that predicts the dome height as a function of input voltage and force.

An operational limitation of the THUNDER™ is that it should be limited to half of the piezoelectric ceramic's Curie temperature, which is around 125 °C (257°F). This is because when the piezoelectric is operated over time; degradation of the properties can be significant, thus causing a decrease in performance. Similar actuators to the THUNDER™'s room temperature shape and construction were built using other substrates and epoxies (Yoon et al, 2002), which could lead to better performing THUNDER™ actuated control valves in the future for these environments.

3.0 THUNDER™ VALVE DESIGN

The detailed CAD drawing can be seen in Figure 12. The valve was constructed of Plexiglas in order to monitor the behavior of the THUNDER™'s apex during flow modulation. The flow area variation occurs in at the apex of the actuator as shown in Figure 13. When the actuator height is varied by input voltage, the change in the orifice area causes a change in flow through the valve, which is the key to understanding the flow modulation technique. If a positive voltage is applied, the actuator deflects down and the orifice area increases causing an increase of the nominal flow through the valve. Moreover, if negative voltage is applied, the actuator deflects toward the top of the flow channel and the orifice area decreases causing a decrease of the nominal flow through the valve. Figure 14 shows a photograph of the airflow control valve. The fixed end for mounting the actuator is shown in Figure 13 and corresponds to the end in Figure 14 where the leads protrude from the Plexiglas housing. All schematics in this thesis shown the inlet into the valve from the left hand side as well as the outlet going to the right hand side. The valve could be rotated and still modulate flow, however the key to modulating the flow resides in the boundary conditions of the THUNDER™ itself. As long as the end of the actuator that is closest to the inlet of the valve is fixed while the other end is remained sliding, then the actuator can deflect properly to modulate the flow.

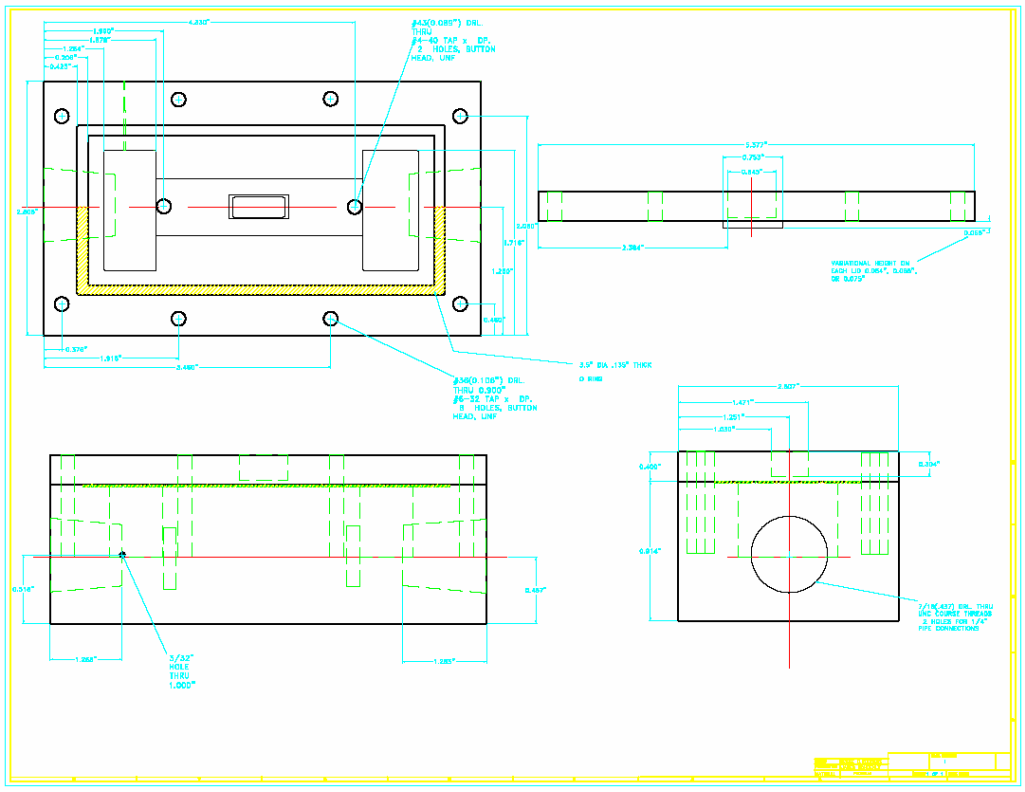

Figure 12. AutoCad Drawing of Control Valve.

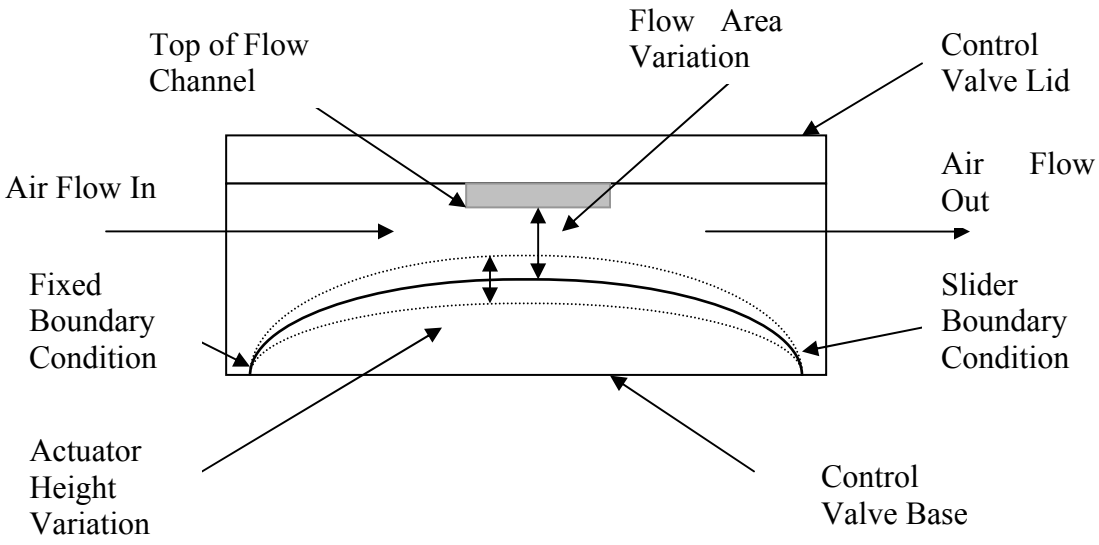

Figure 13. Side view schematic of flow channel in valve.

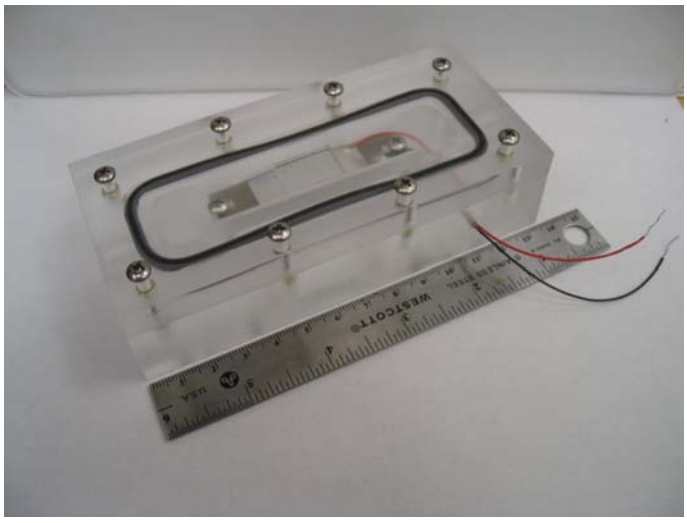

Figure 14. Photograph of control valve housing the THUNDER™ actuator.

.

Several orifice area geometries were implemented as shown in Figure 14. Manufacturing different lids and installing them on the control valve altered the initial orifice area prior to actuator influence. To extract the lid, the fastening screws must be removed, where one is shown in Figure 13. The o-ring would stick to the lid on occasion; therefore caution was taken during the testing of various lids under flow control operation.

To provide variability in the test conditions of the valve in the experimental loop, various lids were constructed for the valve flow chamber to create different orifice shapes for the flow to pass through. A total of five lids were constructed, each having a shape, as shown in Figure 15. Three lids had a rectangular shape (labeled lids 1, 2 and 3), one lids had a triagnluar shape (lid 4) and one lid had a concave shape to fir the profile of the THUNDER™ (lid 5).

The three rectangular lids had different depth of protrusion in the flow channel that crated different nominal heights of the flow orifice for conditions of no flow and no voltage applied to the actuator (Figure 16). All lid depths and corresponding nominal orifice heights are shown in

table 3. Prior to air inlet application, lid 1's channel protrusion is above the apex of the actuator, lid 2's channel protrusion slightly contacts the apex of the actuator, lid 3 actually preloads the actuator, lid 4's sharp profile preloads the actuator and lid 5's curved surface slightly contacts the apex of the actuator.

Table 3. Lid identification summary.

Lid Identification (ID)	Lid Depth	Nominal Orifice Height
1	1.372 mm (0.055")	0.015 mm (0.0004")
2	1.651 mm (0.065")	0.0 mm (0.0")
3	1.905 mm (0.075")	-0.015 mm (-0.0006")
4	1.905 mm (0.075")	-0.015 mm (-0.0006")
5	1.372mm (0.055")	0.0 mm (0.00")

All lids had a small volume of Plexiglas bored out to permit the photonic sensor head to measure the actuator deflection during operation. Dashed lines in Figure 15 represent the removed section since they are hidden from the view of the cross section.

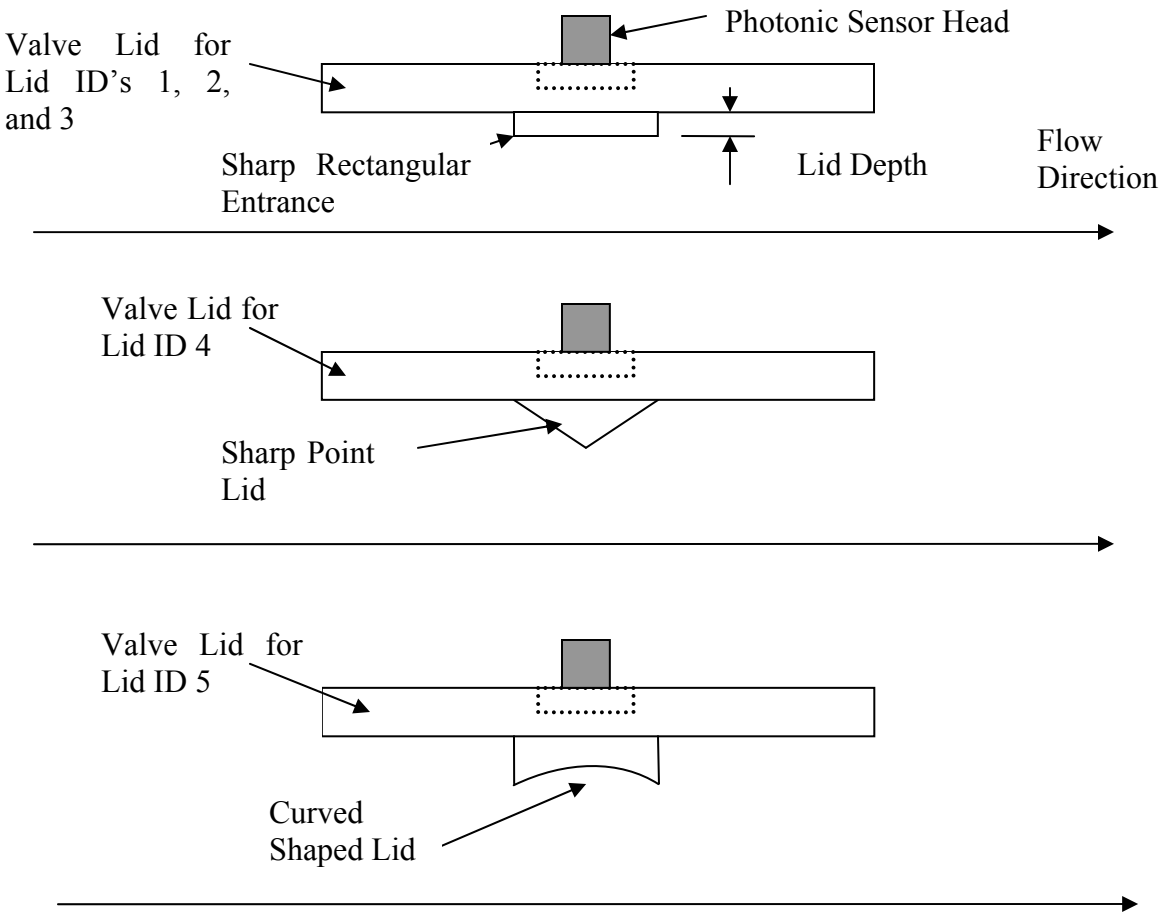

Figure 15. Cross sectional schematic for various orifice area shapes created by each lid during testing.

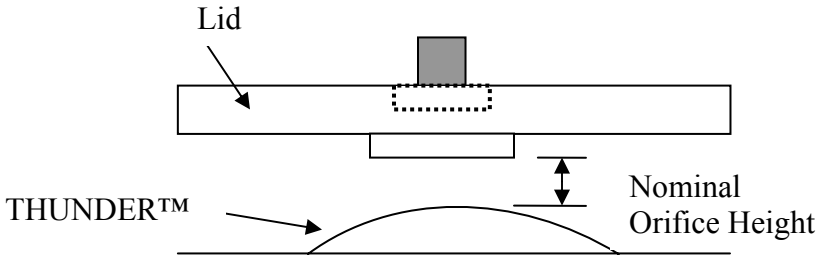

Figure 16. Schematic of flow channel showing nominal orifice height (no voltage applied to actuator and no flow).

4.0 EXPERIMENTAL TEST SETUP AND PROCEDURE

The following sections describe how each test was conducted, from the stand alone observations of the THUNDER™ actuator to its ability to effectively act as a prime mover in a gas control valve for both single and dual flow loop conditions. Moreover, their corresponding experimental setups are shown and explained.

4.1 BASELINE TESTS OF THE THUNDER™ ACTUATOR

Prior to conducting flow modulation tests, the THUNDER™ actuator's behavior was analyzed outside of the valve assembly. Measurement of the deflection and strain due to applied voltage and load were completed. In order to do so, a strain gauge was mounted to the bottom surface of the actuator to correlate deflection as a function of voltage and applied load (Dally et al, 1991). Figure 17 shows the location of the strain gauges on the substrate, particularly right at the apex of the actuator. The uniaxial strain gauge was used for strain acquisition. Figure 18 shows a photo of the experimental setup to measure strain and deflection. EA-06-125BZ-350 strain gauges from the Measurements Group, Incorporated were used to measure the strain, and a KD-300 photonic sensor from MTI, Inc. was used to measure the deflection of the actuator. A KEPCO BOP-1000M power supply from Kepco, Inc was used to apply the voltage into the actuator.

Prior to any testing, the calibration of the photonic senor was necessary. In order to obtain the calibration curve, the photonic sensor output voltage was monitored and plotted as a function of distance observed from the micrometer handle the sensor head is attached to. The location of the

head is shown in Figure 19 where B is the height of the apex of the actuator from which the deflection occurs. Results presented in this thesis are an average of 5 trials with their respective standard deviations.

In order to properly achieve deflection in a valve during operation, the actuator was constrained with fixed-sliding conditions. Fixed –sliding refers to one end of the actuator fixed with no ability to move, and the other end is constrained allowing the actuator to move laterally and with rotation at that point, but not transversely as shown in Figure 19. The actuator shown in Figure 11 is the same one in Figures 17 through 19 however the leads are defined by assigning the positive lead to the piezoceramic and the negative lead (ground) as the one attached to the stainless steel substrate.

To simulate applied force due to flows, small brass weights were suspended from the actuator. Figure 19 shows the experimental setup and the location of where the weights were hung.

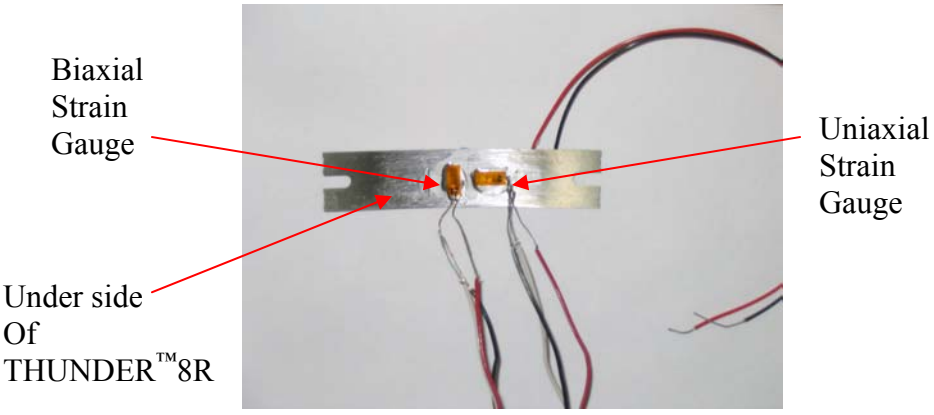

Figure 17. Strain gauges mounted to THUNDER™8R.

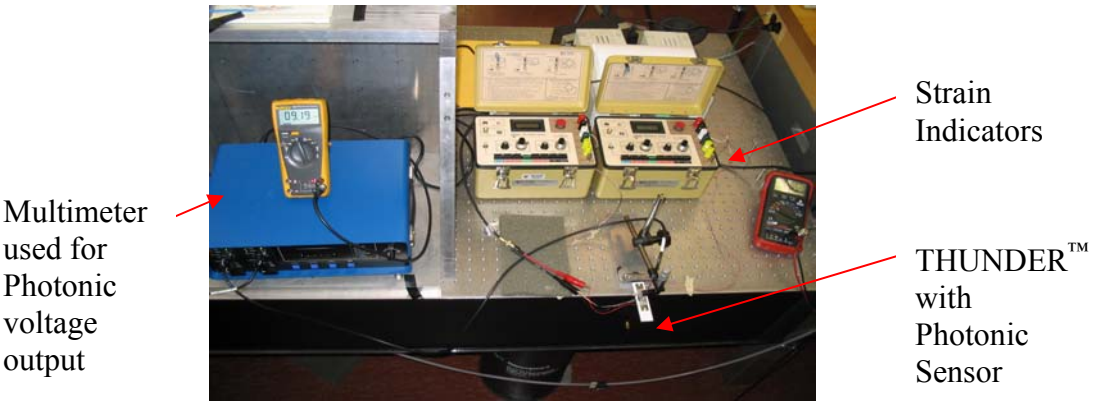

Figure 18. Experimental setup for THUNDER™8R analysis.

The first test observed the actuator's deflection and strain as a function of each voltage increment applied for the fixed-sliding imposed boundary conditions. By imposing fixed – sliding boundary conditions, the original apex height decreased from 3.83 mm (0.153 in) to 1.88 mm (0.074 in). The decrease in height results because fixing one end decreases the actuator's curvature and moves the apex lower to the table. For example, in Figure 19 the "B" dimension will be close to the base. The voltage range was based on the limits set forth by the manufacturer. For example, for a piezoelectric ceramic having an 8-mil (0.008 in) thickness, which is the case for this research, the maximum positive voltage applied is 60 volts per mil. Moreover, the maximum negative voltage applicable is 30 volts per mil. This leads to operational limits of -240 to 480 volts from the ceramic having an 8 mil (0.008 in) thickness. Since the experiments were repeated very regularly, more conservative limits of -200 to 400 volts were used.

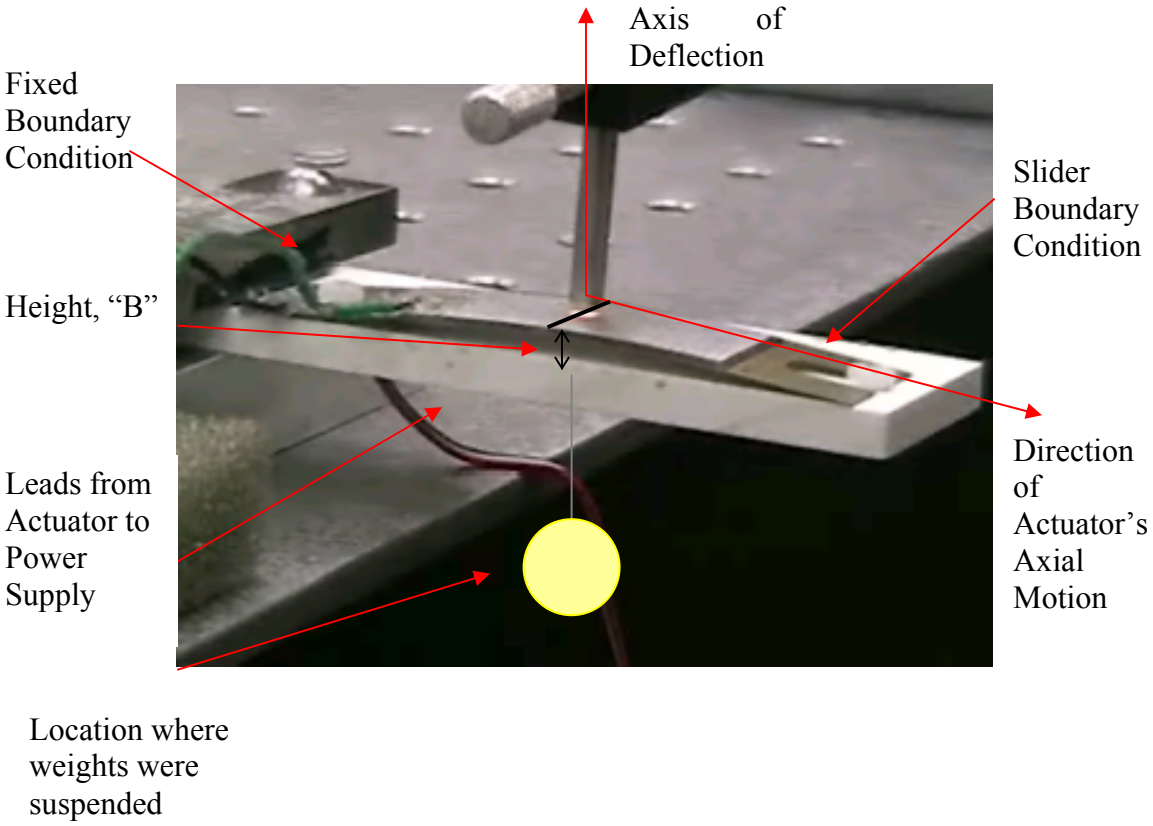

Figure 19. Close view of Photonic Sensor.

4.2 LOAD TESTING OF THE THUNDER™ ACTUATOR

The following test considers the behavior of the actuator as a function of weight applied to the apex. This was completed in order to simulate various forces acting on the actuator during operation. Notice that there are two forces acting on the actuator inside the valve that influence its deflection. The first force is from the air flowing across the surface of the actuator and putting

a load on it. The second influence is the voltage dependence on the deflection when the voltage is applied to control the flow, which was the basis for the initial testing.

Once the testing of the actuator was completed, the actuator was inserted into the valve assembly. By manufacturing the valve out of Plexiglas, the Photonic sensor could be used to measure the deflection of the actuator during operation. Thus the strain gauge approximation of actuator's apex deflection and the actual measured deflection were compared by observing the change in orifice height through the flow area.

4.3 FLOW LOOP TESTING OF THE VALVE

A flow loop was constructed for testing the control valve as shown in Figures 22 and 23. Flow is supplied by the 828 kPa (120 PSI) house air line, which is shown in Figure 22. The house air inlet passes through a filter and a regulator and enters the flow loop through Tygon tubing to the "T" split on the bottom left center side of the photo. The regulator was used to limit inlet pressure to the loop, which did not exceed 172 kPa (25 PSI) for any tests. After the "T" split in Figure 23, the two 6.35 mm (0.25 in) lines lead into downstream gate valves. These valves were placed to monitor the impact of pressure drop to obtain larger flow modulation and to ease in toggling from single to dual flow loop conditions. To perform baseline testing on the valve with a single flow loop, the bypass line was shut off with a gate valve, GV1. The dual flow loop setup was used to simulate the application in which flow balancing is required. After the downstream gate valves, Tygon tubing then leads to the corresponding flow meters. Each flow meter has an Omega pressure sensor on the exit end to measure the backpressure. Initially the output of the pressure transducers was minimal so AMP02E amplifiers were incorporated so that the output could be read with multimeters. The two flow meters used were King Instruments models 7520

rated at 113 to 1190 SLPM (4 to 42 SCFM) and the 7510 rated at 57 to 566 SLPM (2 to 20 SCFM). The 7510's higher resolution of 5.66 SLPM (0.2 SCFM) allowed for a more accurate change in flow measurement than the 7520 flow meter, which had a resolution of 7.07 SLPM (0.25 SCFM). The backpressure curves for each flow meter are shown in Figures 20 and 21. Obtaining the pressure correction factor, K_p from Figures 20 or 21, and inserting it into Equation [1], the true flow is obtained.

$$Q = K_p \cdot Q_{MeterReading} \qquad [1]$$

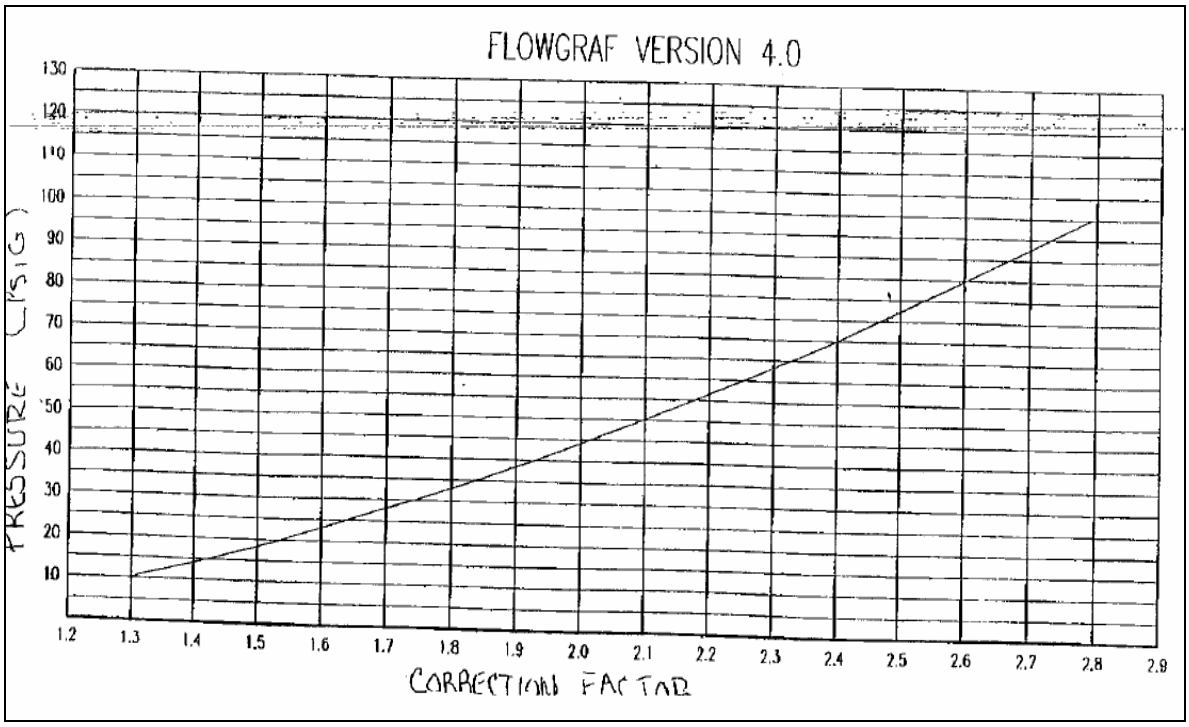

Figure 20. Back pressure curve for King Instrument Rotameter 7510.

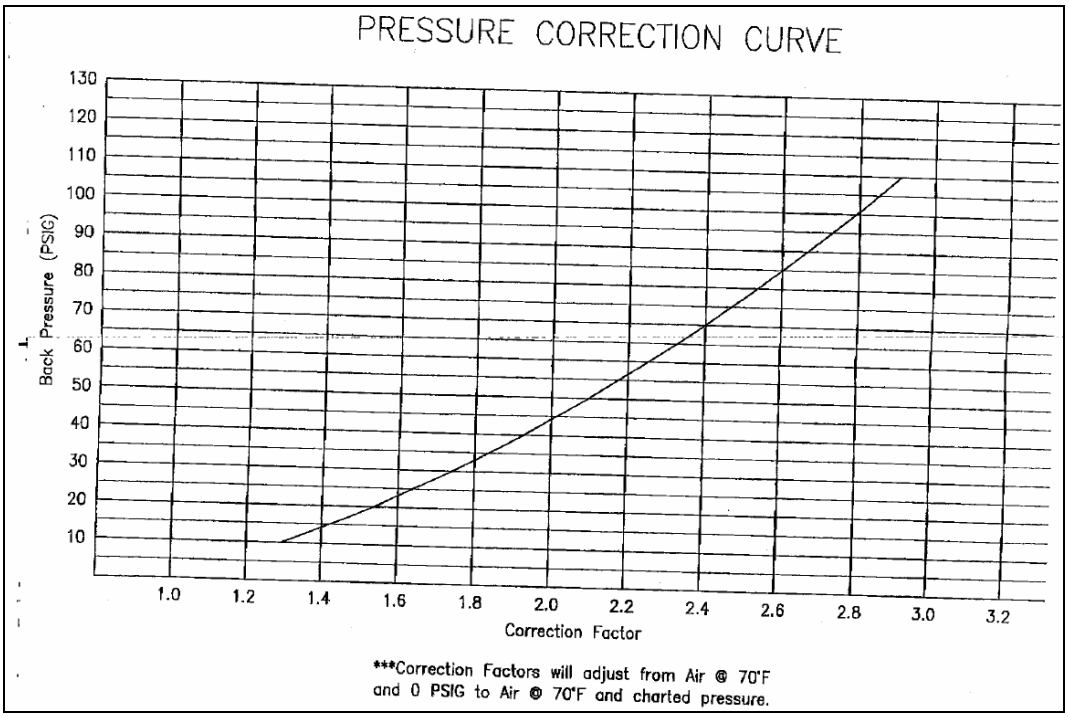

Figure 21. Back pressure curve for King Instrument Rotameter 7520.

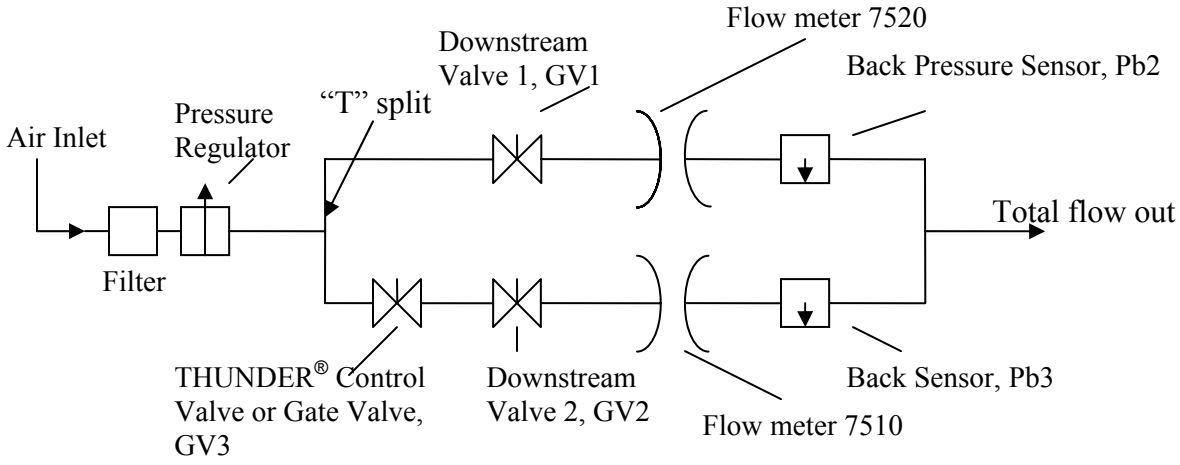

Figure 22. Schematic of flow loop for valve replacement and downstream control valve testing. .

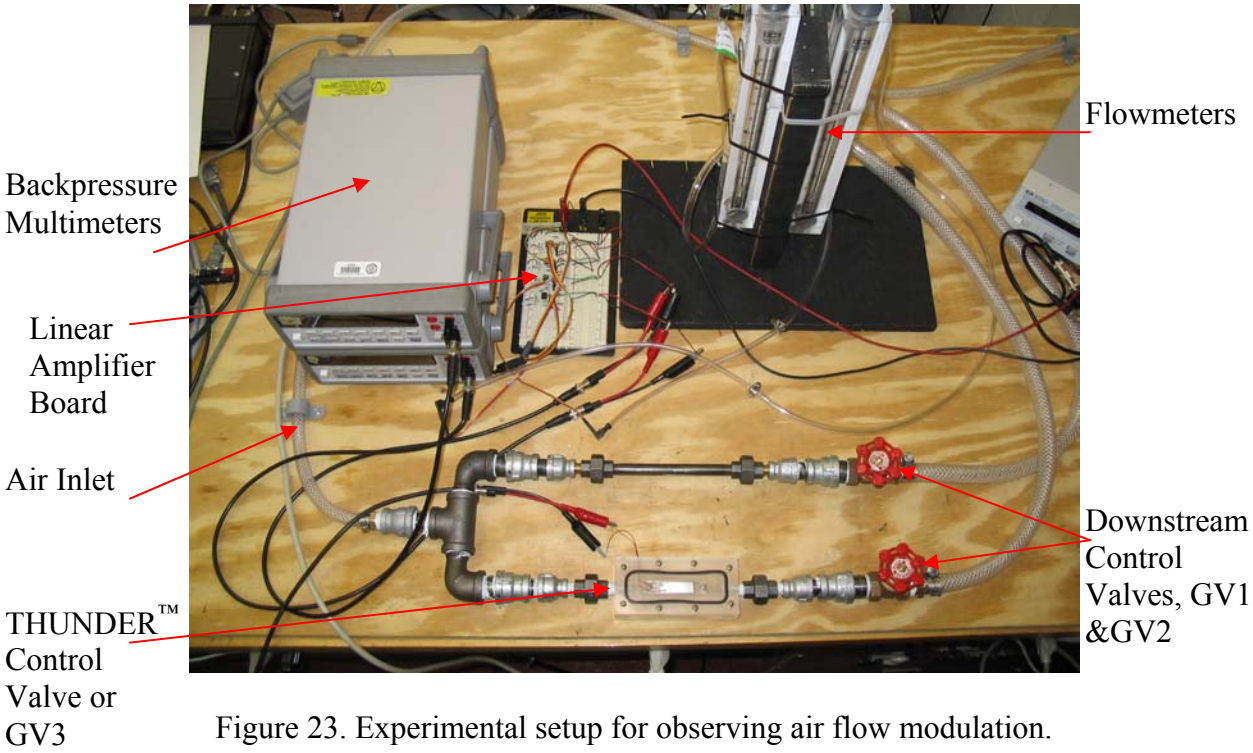

Figure 23. Experimental setup for observing air flow modulation.

The exit end of each flow meter was combined into a single output flow line as shown in Figure 22. Balanced flow can be achieved in Figure 22 if the THUNDER™ control valve is removed and both downstream gate valves, GV1 and GV2, are set equally open. Also in Figure 23, the THUNDER™ valve can be removed, and another valve (GV3), whose physical dimensions are identical to the other downstream gate valves (GV1 and GV2), can be installed to monitor it's (GV3) overall controllability in the flow loop. All loose tubing was secured to the base using clamps to eliminate any outside vibrations or resonance onto the control valve assembly.

Results were measured for an applied actuator voltage from 0 to 450 volts, and then recorded from 0 to -200 volts. The samples were not obtained from -200 volts to 450 volts for one cycle, or vice versa. This was completed to avoid any hysteresis from the actuator or the strain gauge during operation.

5.0 RESULTS

The results section will be divided into 5 sections. The first section contains the results from calibration and the deflection of the actuator as a function of voltage and strain. The second section presents the results of the actuator deflection as a function of an applied weight and strain. Section three shows an empirical model created for deflection as a function of strain and as a function of pressure once in the control valve. The results of the downstream control valves and flow modulation are summarized in the sections four and five.

5.1 PHOTONIC PROBE CALIBRATION

Before any deflection tests were done, the photonic probe had to be calibrated. Figure 24 is the calibration curve of the photonic sensor. The data were obtained by observing the output from the sensor head of the probe as a function of the gap increase. It shows that the head placement was varied from the point of just touching the actuator to the maximum output the sensor head will read from the reflective aluminum electrode of the actuator.

Notice that the midpoint of either linear region is the location at which one should operate to maximize the useful linear testing range. For the research of the actuator alone, the left most linear region is used (since the probe can be placed very close to the actuator). Since the valve lid places the probe away from the top layer of the actuator, the right most linear region

is used to measure the reflection of light through the Plexiglas in order to determine the deflection during flow tests.

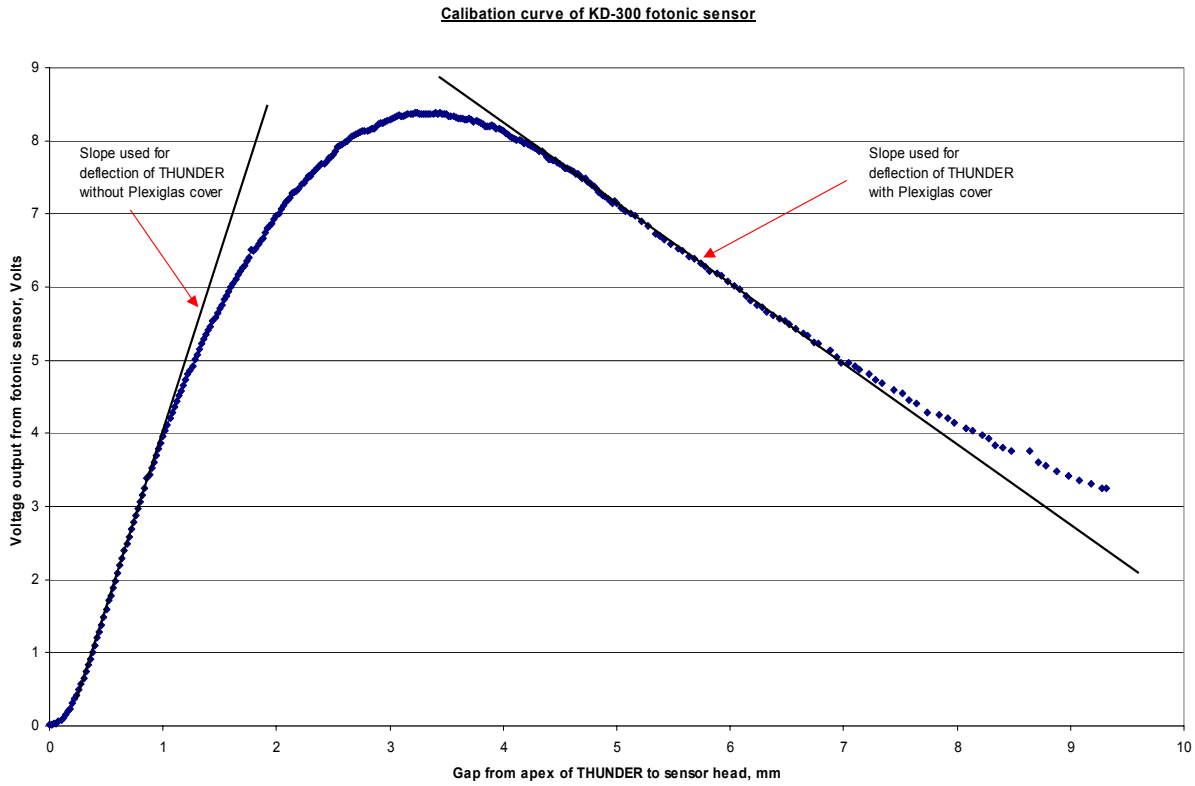

Figure 24. Calibration curve of photonic sensor.

5.2 MEASURING ACTUATOR DEFLECTION AS A FUNCTION OF VOLTAGE

Figure 25 shows the summary of the deflection and the strain obtained from the actuator under fixed sliding boundary conditions. The data were obtained by observing the output of the strain gauge and the photonic sensor as voltage was applied. The errors bar represents the standard deviation obtained from the 5 trials.

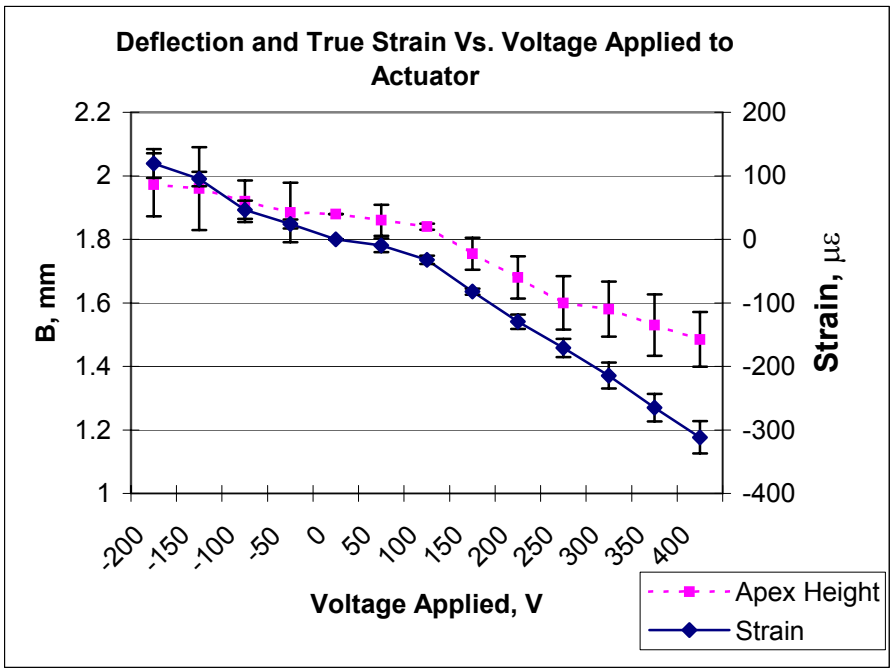

Figure 25. Summary of the actuator's height and strain characteristics per unit of voltage applied (Error bars represent standard deviation from 5 trial sample size).

5.3 MEASURING ACTUATOR DEFLECTION AS A FUNCTION OF FORCE

Figure 26 was obtained by placing weights on a string hung below the apex of the actuator and again observing the strain and deflection. The errors bar represents the standard deviation obtained from the 5 trials.

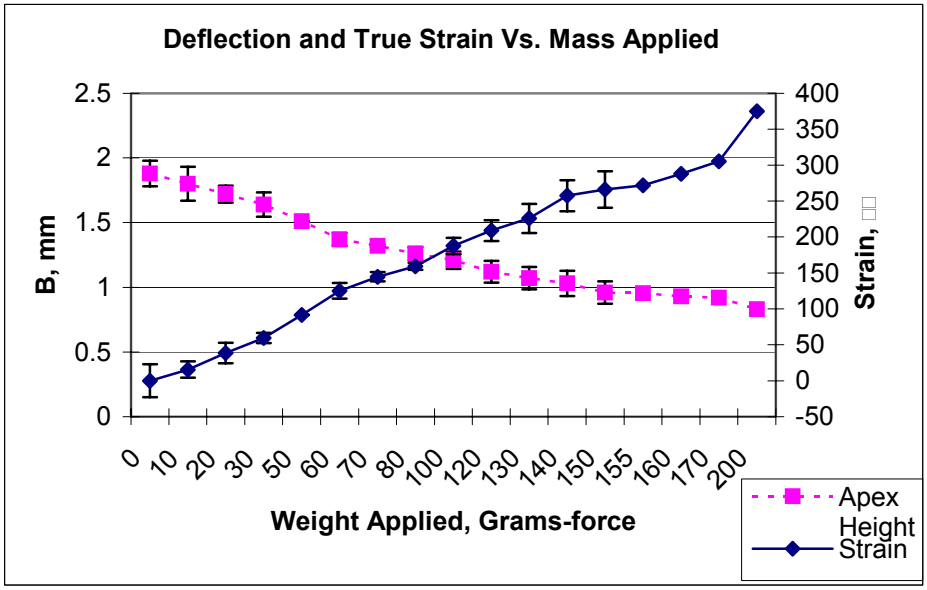

Figure 26. Summary of the actuator's height and strain characteristics per unit of weight applied (Error bars represent standard deviation from 5 trial sample size).)

5.4 EMPERICAL MODEL OF THE ACTUATOR

The control valve was constructed of Plexiglas. If the actuator is going to be placed in higher temperature environment, the Plexiglas material will have to be substituted with some other material that sustains higher temperatures such as steel or aluminum. A method for determining the deflection of the actuator inside an opaque valve was considered and analyzed but not used for the current valve analysis. Since the materials are opaque, the photonic sensor would not be useful for determining deflection so the empirical model was completed in order to estimate the valve deflection from the measured strain while monitoring the voltage applied. The relationship was first analyzed by converting the data observed in Figures 25 and 26 into one axis of strain versus a deflection axis. Figure 27 shows this conversion of plotting each strain versus deflection pair for every incremental point of voltage and weight applied. For example the first slope on the

left hand side of Figure 27 was obtained by observing the variation of the height "B" for each strain value from the voltage applied. In addition, the right hand side of Figure 27 was determined by observing the variation of the height "B" for each strain value from the applied weight. Then trend lines were fitted to each set of data to arrive at Equations [2] and [3].

$$Y_v = 0.0012\varepsilon_v - 0.0266 \quad [2]$$

$$Y_\varepsilon = -0.003\varepsilon_\varepsilon - 0.0823 \quad [3]$$

Equation [2] shows the relationship between the variations of the actuator height, Y_v, deduced from the strain as voltage is applied to the actuator, where ε_v is the strain measured in the actuator substrate as if it could be done during the modulation of air. Equation [3] shows the relationship between the variations of the actuator height, Y_ε, deduced from the strain as weight is applied onto the face of the actuator, where ε_ε is the strain resulting from applied weight. In actual flow testing, ε_ε would be the strain due to the initial air pressure applied to the apex of the actuator prior to activating the control valve with an input voltage. However, the equations are valid for all real values. In addition, there is no strain on the actuator, the actuator has not deflected.

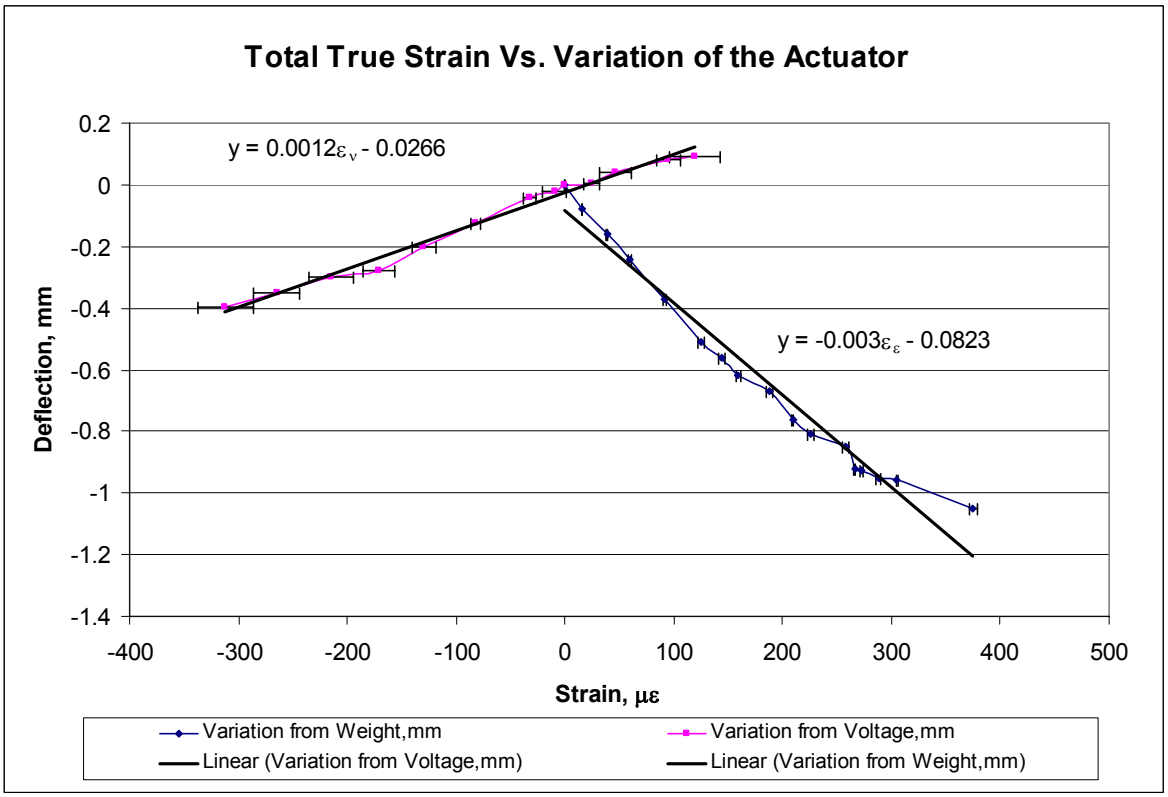

Figure 27. Summary of the actuator's true train with respect to dome height obtained from voltage and weight applied (Error bars represent standard deviation from 5 trial sample size).

Equation [4] is formed by superimposing both equations [2] and [3] to form a generalized empirical equation for the actuator height variation of the actuator shown in Figure 19. This approximation technique is only applicable if one has the initial strain due to the flow, ε_ε , and the final strain at which a known voltage is applied during flow modulation, ε_T .

$$Y_T = Y_\varepsilon + Y_V \qquad [4]$$

The assumption made when applying Equation [4], was that the final strain during flow modulation, ε_T , was the summation of the strain obtained from the voltage trial, ε_v , and the strain obtained during the weight trial, ε_ε . The method for deducing the validity of the empirical model was to observe the variation of the actuator deflection and strain for four applied weight cases

over the voltage range. Therefore, the final equation used for empirical to experimental comparison is Equation [5]. Note that $\varepsilon_T - \varepsilon_\varepsilon$ was substituted for ε_v in Equation [5] which allows for the Y_V to be omitted when figuring out the model as a function of initial deflection and the voltage applied during flow.

$$Y_T = -0.0042\varepsilon_\varepsilon + 0.0012\varepsilon_T - 0.1089 \qquad [5]$$

Weights of 15, 60, 135, and 160 grams (0.033, 0.312, 0.298, and 0.353 pounds respectively) were placed on the string in Figure 19. The variation of the actuator height for each weight case was referenced against the values from Equation [5]. The actuator variation results found from the weight analysis are shown in Tables 4 through 7. Figures 28 through 31 graphically represent the relationship of measured deflection with respect to Equation [5] from Tables 4 through 7. The results show that closer approximations are achieved at lower drive levels (lower voltage range). It is also noted that the percent difference is the deviation of the empirical equation, Eq [5], relative to the measured apex deflection of the actuator. If the percent difference is negative, then Equation [5] is lower than the measured apex variation. If the percent difference is positive, then Equation [5] is higher than the measured apex variation.

Table 4. Table of comparison of empirical Equation [5] to15-gram (0.033 lb) case.

Voltage Applied, V	Strain με	Ym From Eq [3], mm	Y_T From Eq [5], mm	Measured Variation, mm	Difference Of Eq [5] from Measured
-200	90	-0.15	-0.10	0.01	1018%
-150	75	-0.15	-0.12	-0.01	1196%
-100	60	-0.15	-0.14	-0.04	340%
-50	42	-0.15	-0.16	-0.06	260%
0	24	-0.15	-0.18	-0.10	171%
50	8	-0.15	-0.20	-0.14	129%
100	-10	-0.15	-0.22	-0.18	105%
150	-26	-0.15	-0.24	-0.25	71%
200	-40	0.15	-0.26	-0.30	56%
250	-53	0.15	-0.27	-0.36	40%
300	-66	0.15	-0.29	-0.42	27%
350	-76	0.15	-0.30	-0.47	17%
400	-86	0.15	-0.31	-0.53	6%

Table 5. Table of comparison of empirical Equation [5] to 60-gram (0.132 lb) case.

Voltage Applied, V	Strain με	Ym From Eq [3], mm	Y_T From Eq [5], mm	Measured Variation, mm	Difference Of Eq [5] from Measured
-200	187	-0.46	-0.42	-0.41	61%
-150	174	-0.46	-0.43	-0.43	58%
-100	159	-0.46	-0.45	-0.43	62%
-50	144	-0.46	-0.47	-0.49	47%
0	127	-0.46	-0.49	-0.50	48%
50	111	-0.46	-0.51	-0.53	43%
100	96	-0.46	-0.53	-0.57	35%
150	82	-0.46	-0.54	-0.63	23%
200	70	-0.46	-0.56	-0.69	12%
250	59	-0.46	-0.57	-0.73	5%
300	48	-0.46	-0.58	-0.79	-5%
350	40	-0.46	-0.59	-0.85	-15%
400	32	-0.46	-0.60	-1.01	-41%

Table 6. Table of comparison of empirical Equation [5] to 135-gram (0.298 lb) case.

Voltage Applied, V	Strain με	Ym From Eq [3], mm	Y_T From Eq [5], mm	Measured Variation, mm	Difference Of Eq [5] from Measured
-200	295	-0.82	-0.79	-0.76	28%
-150	284	-0.82	-0.81	-0.76	30%
-100	272	-0.82	-0.82	-0.80	22%
-50	260	-0.82	-0.83	-0.83	18%
0	247	-0.82	-0.85	-0.85	15%
50	234	-0.82	-0.87	-0.88	10%
100	222	-0.82	-0.88	-0.92	4%
150	211	-0.82	-0.89	-0.95	-1%
200	200	-0.82	-0.91	-1.00	-9%
250	192	-0.82	-0.92	-1.02	-12%
300	181	-0.82	-0.93	-1.03	-13%
350	173	-0.82	-0.94	-1.04	-14%
400	167	-0.82	-0.95	-1.04	-13%

Table 7. Table of comparison of empirical Equation [5] to 160-gram (0.353 lb) case.

Voltage Applied, V	Strain με	Ym From Eq [3], mm	Y_T From Eq [5], mm	Measured Variation, mm	Difference Of Eq [5] from Measured
-200	329	-0.94	-0.92	-0.80	35%
-150	320	-0.94	-0.93	-0.82	31%
-100	309	-0.94	-0.94	-0.85	26%
-50	298	-0.94	-0.96	-0.87	23%
0	287	-0.94	-0.97	-0.89	20%
50	276	-0.94	-0.98	-0.92	15%
100	266	-0.94	-1.00	-0.93	14%
150	257	-0.94	-1.01	-0.94	13%
200	247	-0.94	-1.02	-0.95	12%
250	238	-0.94	-1.03	-0.96	11%
300	227	-0.94	-1.04	-0.96	13%
350	219	-0.94	-1.05	-0.98	9%
400	211	-0.94	-1.06	-0.98	10%

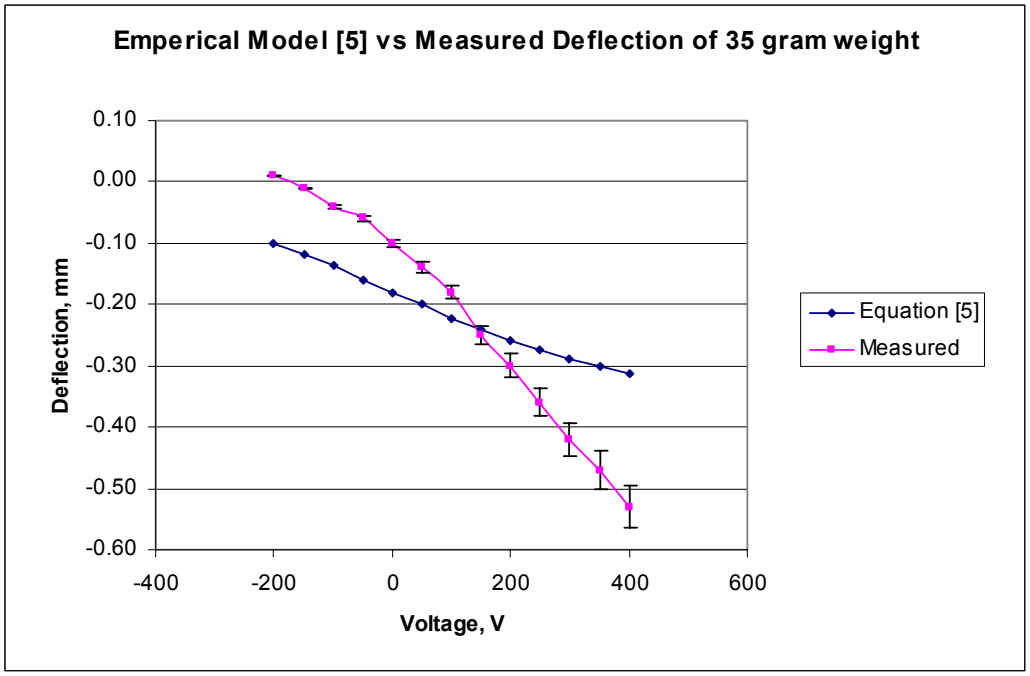

Figure 28.Measured deflection of actuator during operation compared to approximate deflection using equation [5] for a 35 gram weight (Error bars represent standard deviation from 5 trial sample size).

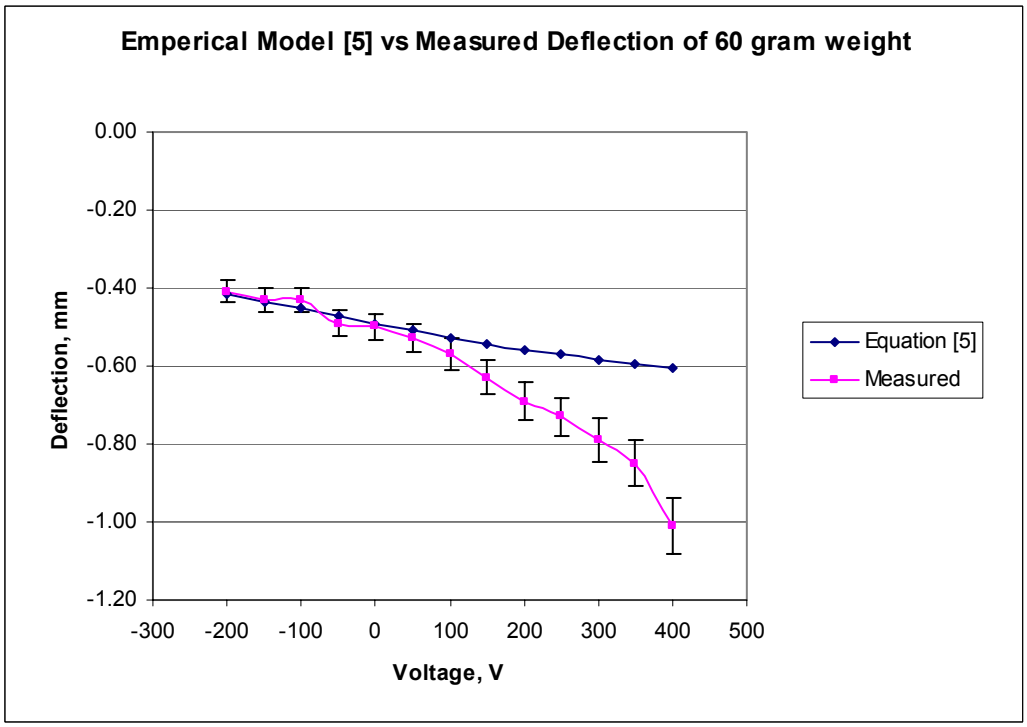

Figure 29.Measured deflection of actuator during operation compared to approximate deflection using equation [5] for a 60 gram weight (Error bars represent standard deviation from 5 trial sample size).

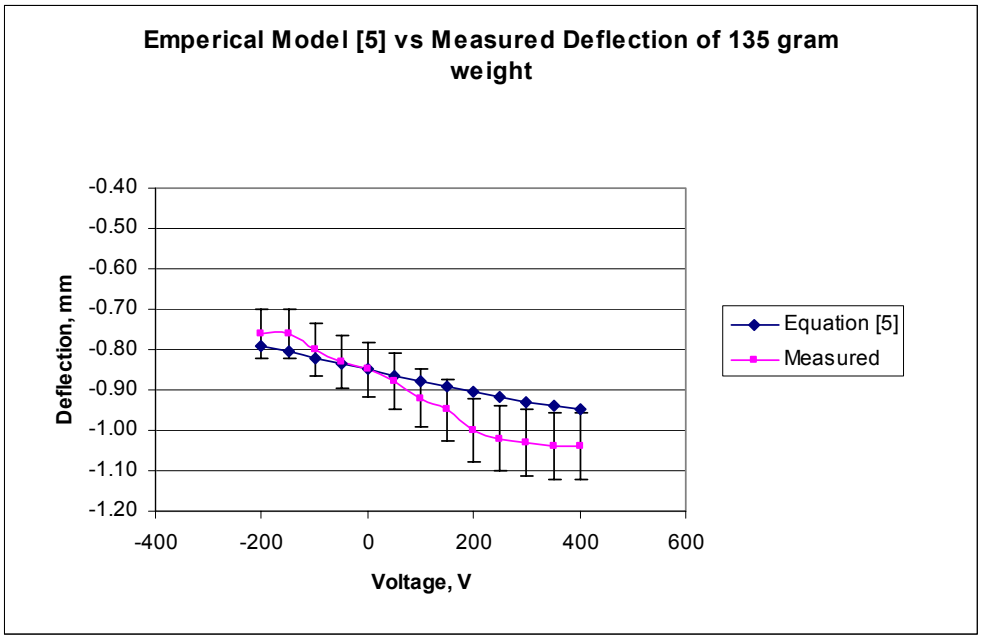

Figure 30.Measured deflection of actuator during operation compared to approximate deflection using equation [5] for a 135 gram weight (Error bars represent standard deviation from 5 trial sample size).

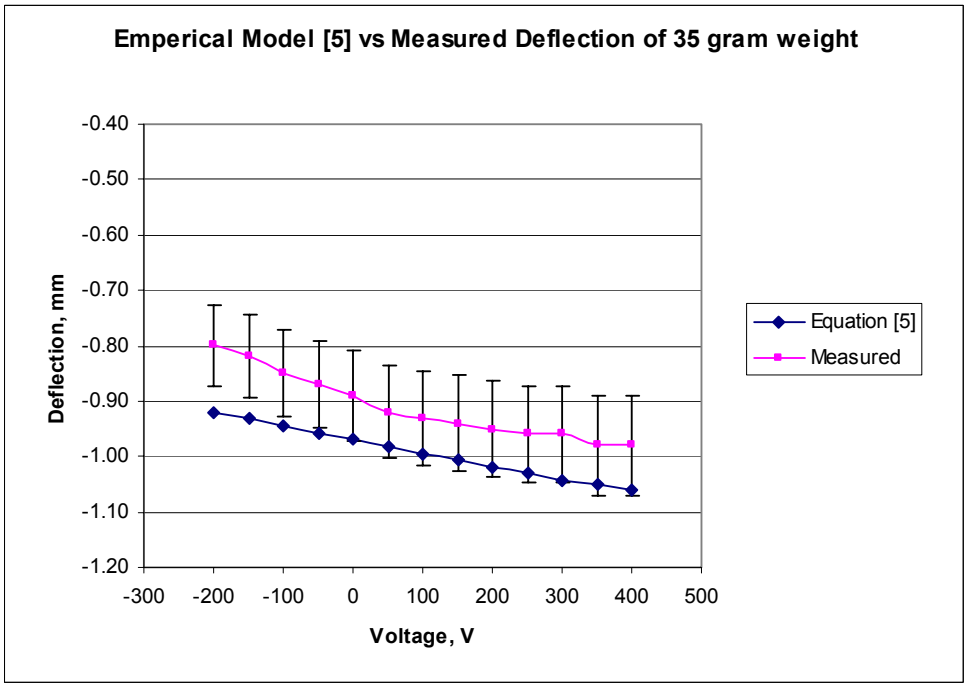

Figure 31.Measured deflection of actuator during operation compared to approximate deflection using equation [5] for a 160 gram weight (Error bars represent standard deviation from 5 trial sample size).

5.4.1 Additional models of the actuator

To observe the proper actuation behavior under a weight, a force versus displacement curve was created. The orientation of the displacement axes for the actuator can be seen in Figure 32. Figure 33 shows the force versus displacement curve of the actuator determined experimentally using the initial height shown in Figure 32. The data were obtained by driving the actuator within the maximum range for 4 different weights that were hung from the apex as in Figure 19. The weights act as the applied force while the actuator is deflected due to applied voltage.

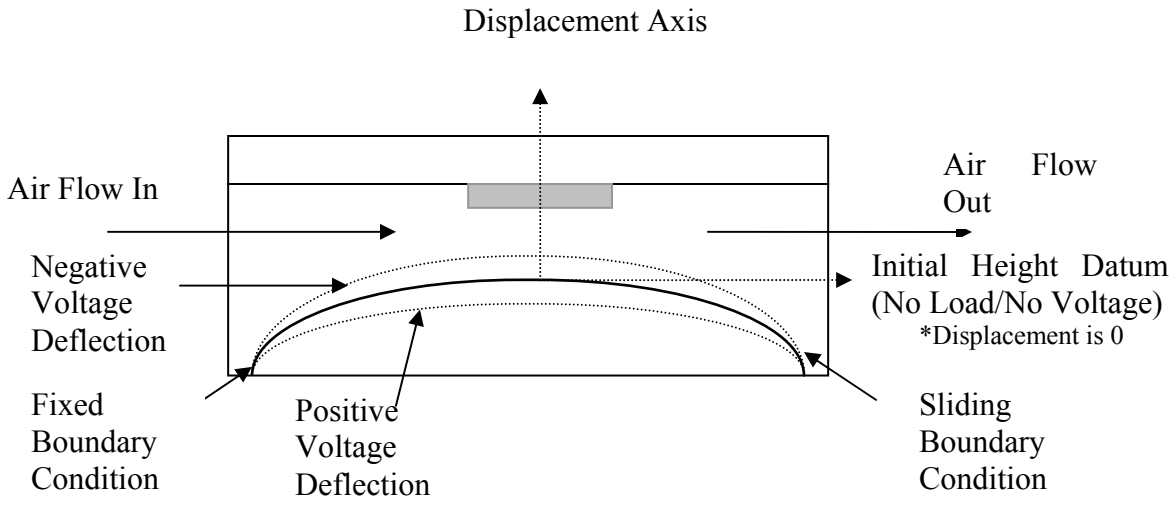

Figure 32. Schematic of no load/no voltage axis on actuator.

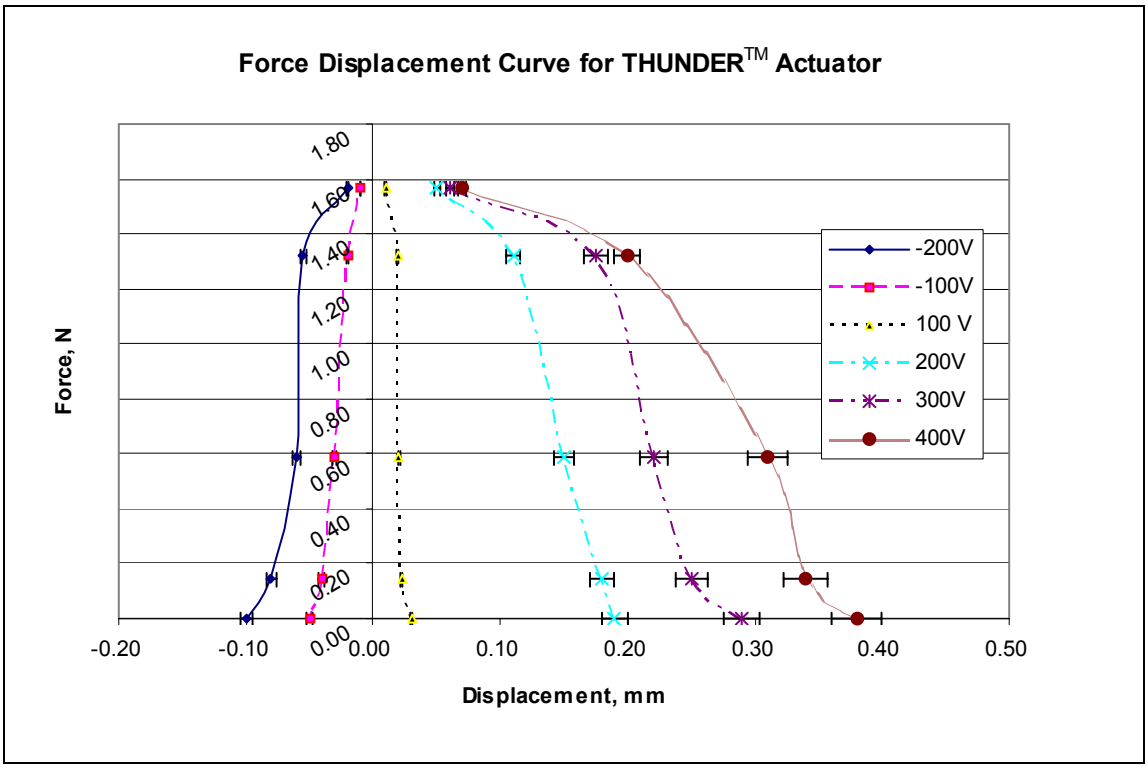

Figure 33. Displacement vs. force diagram of a THUNDER™ actuator (Error bars represent standard deviation from 5 trial sample size).

Another way to monitor proper performance involves the comparison of the experimental measurements obtained in Figure 25 to the measurements and the analytical model created by Weinman (Weinman 2001). Using a 5 trial average, standard deviations were determined and shown relative to the Weinman model. The experimental slope of 0.22 mils/volt (0.00022 in/volt) shows that the results, when compared to the work done by Weinman et al, were relatively close to some degree. The experimental setup and method for collecting the results in Figure 34 were the same as the method used for the results presented in Figure 26. Figure 34 shows that the approximation by Weinman was successful in that the experimental results we within %20 of each data point.

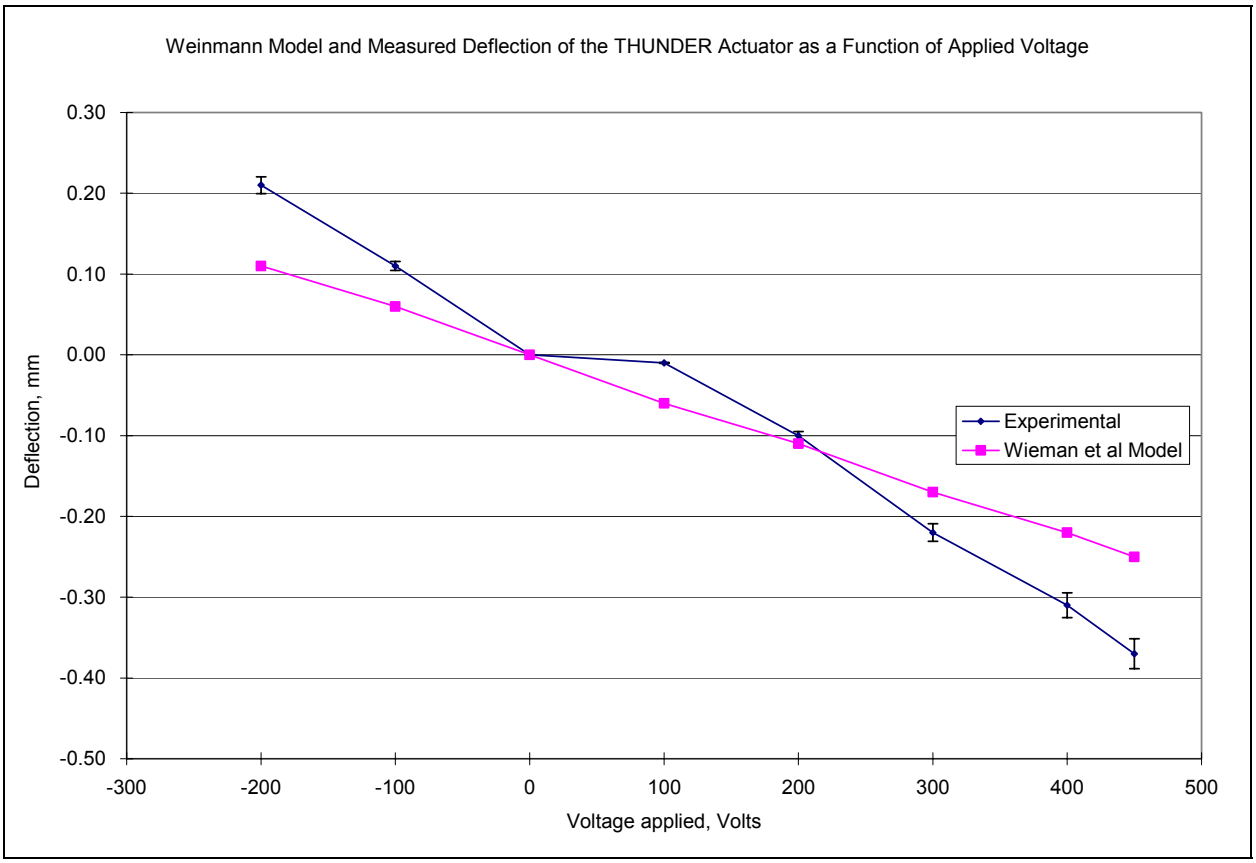

Figure 34. Weinman model compared to experimental results (Error bars represent standard deviation from 5 trial sample size).

After the THUNDER™ actuator's operating characteristics were determined; the actuator was inserted into the valve housing to create a flow control valve.

5.5 RESULTS OF VARYING THE DOWNSTREAM GATE VALVE SETTINGS

Once the detailed testing of the actuator was completed, testing the valve's flow modulation was completed. In order to compare to unbalanced flow, downstream gate valves were implemented to model unbalanced flow of the control valve. The first step was to determine just how the downstream gate valves would affect the performance of the THUNDER™ valve. In order to

determine what conditions to place the control valve in for testing, a third gate valve, GV3, was inserted at the location of the THUNDER™ control valve in Figure 22 and adjusted from its fully opened position to fully closed. The GV3 valve provided the best case flow control results since it had the ability to be completely shut off and also to allow for full flow when completely opened. This important characterization aided in determining the THUNDER™ control valve's performance and it's perspective to flow control. The acceptable region of operation is reliant on the impact of the pressure drop that occurs across a valve. As the pressure drop across a valve increases, a small amount of movement in the valve will have a greater impact on the flow modulation than when operating at a lower pressure drop. The pressure drop is determined by examining how much flow can be restricted when implementing a valve into a full flow environment. Intuitively, if full flow is going through the system in Figure 22 (both GV1 and GV2 are fully opened) and no control valve or GV3 is installed, the flow though each line is balanced. As soon as a control valve is inserted into the position specified in Figures 22 and 23, the flow becomes diverted to the line with less restriction. Balancing the flow loop was done prior to implementing the control flow valve and was not balanced afterwards. Figures 35 through 39 show the flow performance curve for the single and dual flow loops under a 137.9 kPa (20 PSI) inlet pressure. Single loop flow occurs when the bypass valve, shown in Figure 22 as GV1, is shut off completely. This is controlled by the amount of revolutions the valve control knob is turned in the direction of opening. For example, one revolution open is defined as from the fully closed position; GV1 or GV2 will be opened by turning the valve knob one full revolution to allow for an increase in flow. The area of importance in Figures 35 through 37 is the location where the flow can be changed significantly with small changes in the GV3 valve position. This is defined as the desirable operating range. The undesirable range is defined as

the range of flow in which any cross sectional change in flow orifice area will not lead to any significant change in flow.

Figures 35 through 37 show the performance curves of the replacement gate valve, GV3, during modulation tests in a dual flow loop under a 137.9 kPa (20 PSI) pressure inlet. Notice that regardless of the downstream gate valve (GV2) setting, the slopes of the GV3's controllability are similar. The bypass, GV1, along with the downstream gate valve, GV2, was opened for a variety of positions during dual flow loop tests to monitor the impact of the downstream gate valves onto the performance of the control valve (Figures 38 and 39). The flow through the bypass valve does decrease as more flow through GV3 increases. In addition, Figure 39 shows the balance flow that occurs when both flow lines are 226.5 SLPM (8.0 SCFM). Therefore, the actuated THUNDER™ control valve will always be controlled in a loop in which the downstream gate valve is fully open. As shown in Figures 36 and 37, adjusting GV2 will only scale the flow, not allow for better controllability as a function of pressure drop created. Several other inlet pressures were tested and the trends are similar. The flow control of the valve remains the same; only the flow rates decrease at lower pressures.

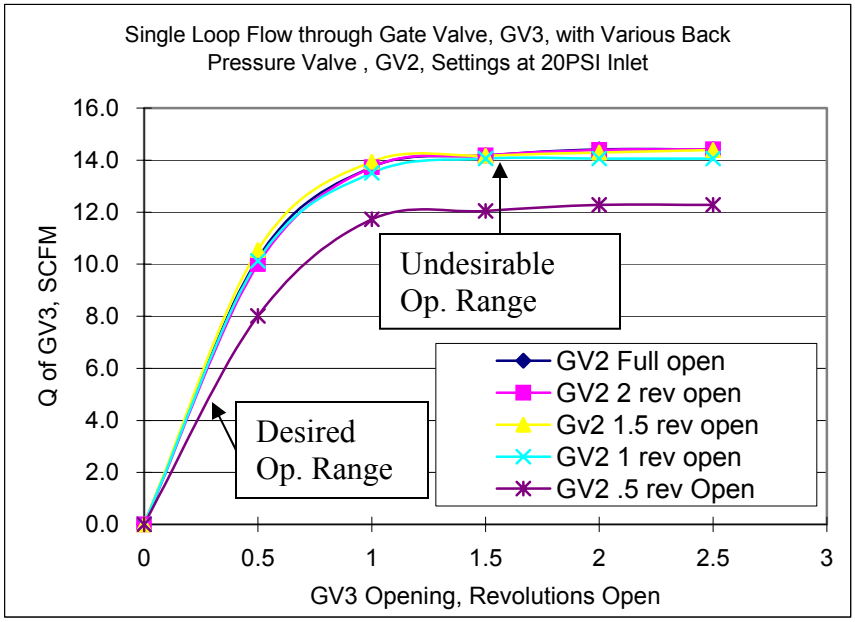

Figure 35. Replacement gate valve,GV3, performance curve under a 137.9 kPa (20 PSI) pressure inlet for single loop flow.

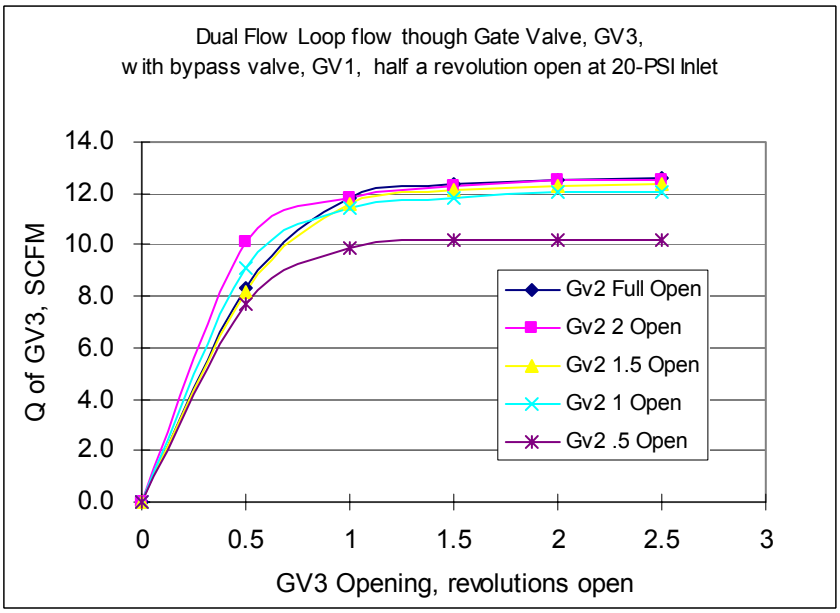

Figure 36. Gate valve, GV3, performance flow curve under a 137.9 kPa (20-PSI) pressure inlet with bypass valve, GV1, half a revolution open for dual loop flow.

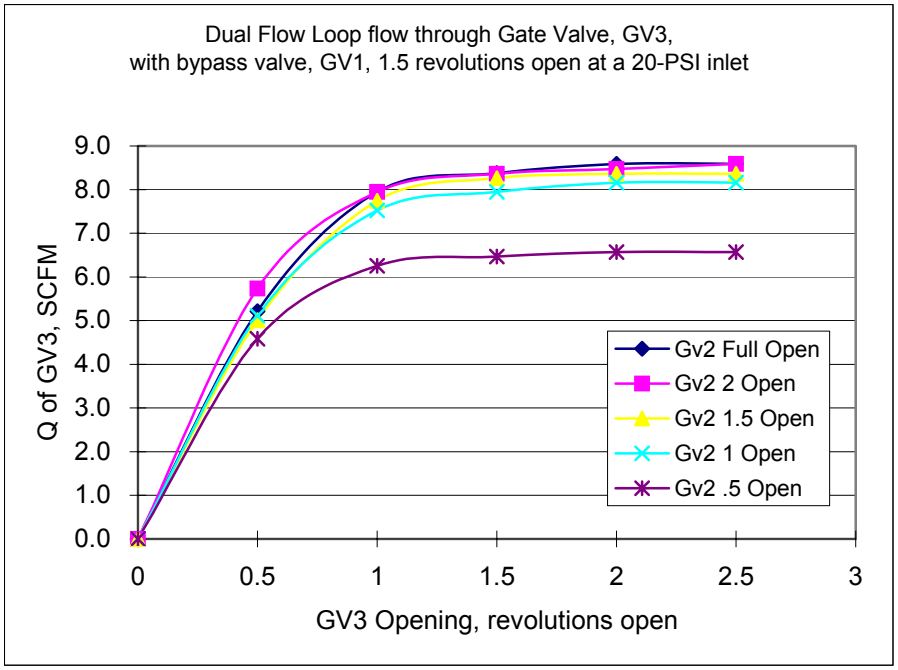

Figure 37. Gate valve, GV3, performance flow curve under a 137.9 kPa (20-PSI) pressure inlet with bypass valve, GV1, 1.5 revolutions open for dual loop flow. .

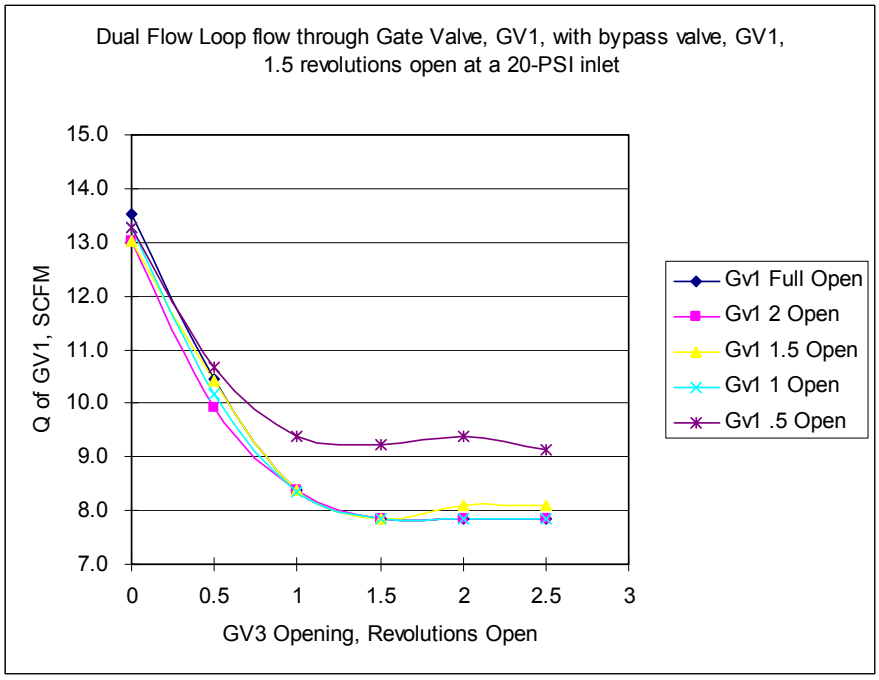

Figure 38. Gate valve, GV1, performance flow curve under a 137.9 kPa (20-PSI) pressure inlet with bypass valve, GV1, 1.5 revolutions open for dual loop flow.

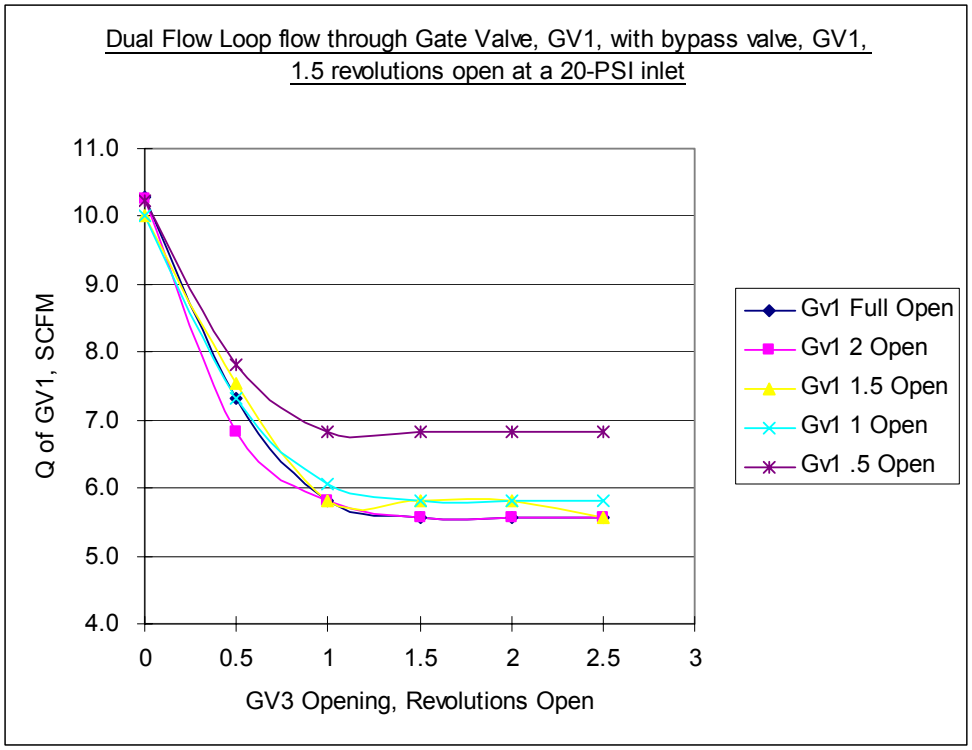

Figure 39. Gate valve, GV1, performance flow curve under a 137.9 kPa (20-PSI) pressure inlet with bypass valve, GV1, half a revolution open for dual loop flow.

5.6 THE CONTROL VALVE MODULATION RESULTS

Before presenting the flow control results, it is necessary to define the percent modulation term, which will be important in accurately describing the performance of the flow control system. Percent modulation of flow "%Q" or controllability will be mentioned throughout this thesis. In order to speak quantitatively of the magnitude of gas modulation, one must explain what exactly the term 'modulation' refers to. For the remainder of this thesis, the term percent modulation will refer to the change in flow rate for any applied voltage relative to the nominal flow rate determined Q_{nom}, where Q_{nom} is defined as the flow rate for no voltage applied. If Q is the flow rate at an arbitrary actuator voltage then the flow rate modulation is defined in Equation [6].

$$\%Q = \frac{Q - Q_{nom}}{Q_{nom}} \quad [6]$$

The results are presented for the maximum and minimum flow rates, which correspond to positive and negative percent modulation in flow.

5.6.1 Single flow loop

The flow modulation results for lids 1, 2, and 3 are summarized in Table 8 by the ability of each valve to modulate flow relative to a nominal flow in a single loop configuration. Table 9 compares the current design to that of the valves researched in the literature. Table 10 summarizes the modulation of the THUNDER™ valve in a dual flow configuration where both flow lines were set using GV1 and GV2 fully opened. This percentage was defined in Equation [6]. The modulation was measured by using the setup in Figures 22 and flow orifice orientations in Figures 13, 15 and 16.

Figure 40 summarizes just how much influence the initial air flow through the valve has for each individual lid from Table 3. Depending on which lid from Table 3 that is used, it may slightly contact the actuator or preload it prior to installation into the flow loop. Once the lid was installed on the control valve, it was then placed into the flow loop. Once the air entered the flow valve, the actuator deflected down a certain distance and the nominal flow was recorded. Table 8 shows the percent modulation of the flow that the control valve attained for various lids under various inlet pressures. For example, a 0.85 mm (0.033 in) initial deflection of the actuator occurs by using lid 3 at 103.4 kPa (15 PSI) of air. Under these conditions, the valve could modulate the flow by as much as -3% to 6% of the nominal flow.

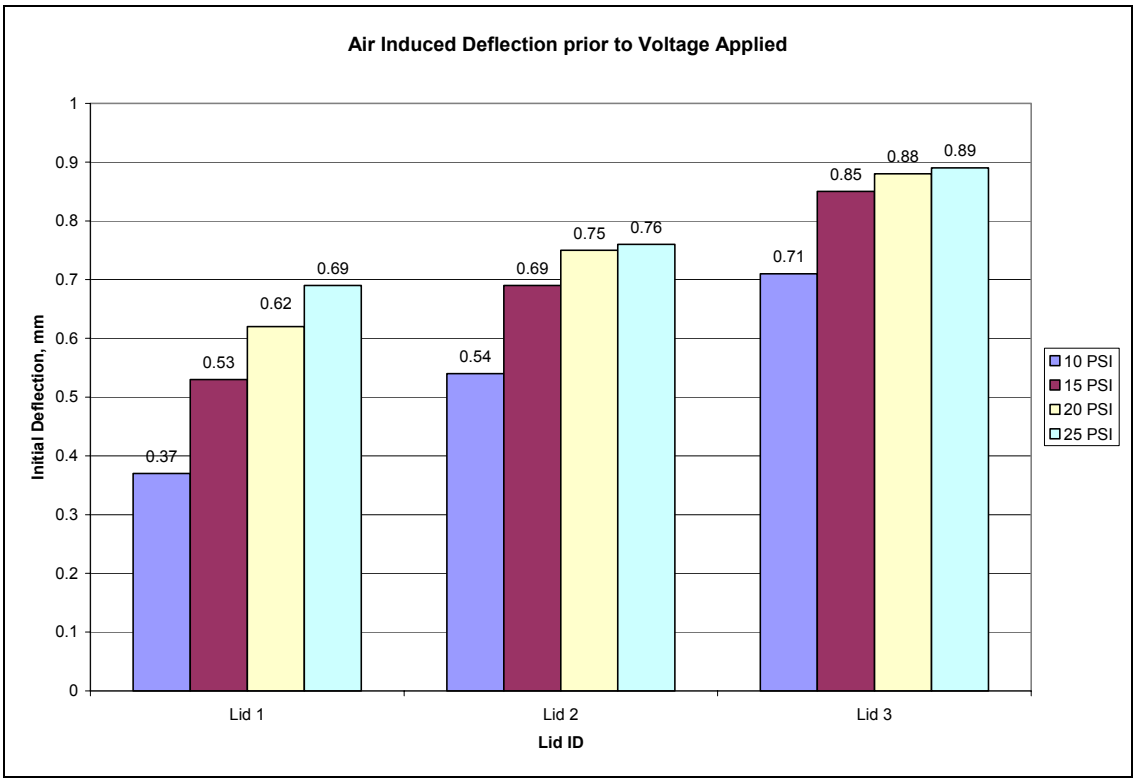

Figure 40. Initial flow induced deflections on THUNDER™ inside control valve for single loop configured system.

Table 8. Single flow loop summary of maximum percent modulation relative to nominal flow under various inlet pressures (Data shown is percent change from nominal flow).

Lid ID	Inlet Pressure 69.0 kPa 10 PSI	Inlet Pressure 103.4 kPa 15 PSI	Inlet Pressure 137.9 kPa 20 PSI	Inlet Pressure 172.4 kPa 25 PSI
1	-4, +6	-1, +5	-0, +4	-0, +3
2	-0, +12	-1, +8	-1, +3	-0, +4
3	-5, +11	-3, +6	-3, +5	-1, +4

Figure 41 shows the actual flow versus deflection data for lid 3 at 69.0 kPa(10 PSI). The extreme points of Figure 41 are used to calculate the data in Table 8. Lid 3 had the largest modulated performance curve for the single loop flow. With a total of 16% (-5, +11) modulation about a nominal flow of 124.6 SLPM (4.4 SCFM), as represented by a dashed line in Figure 41,

the valve's primary purpose of modulating the air flow was achieved. Relative to Table 2, Table 9 shows the relationship of this valves performance compared to other similar valves in the literature. The balance of all single loop flow versus deflection curves are found in Figures A1 through A12 located in the Appendix.

Table 9. Control valve comparison.

Valve	Footprint Size	Flow Range	Max Operating Pressure
THUNDER™ Valve	123 mm by 234 mm by 345mm/ 2.5 inch by 1.4 inch by 5.5 inch	0 - 356.8 SLPM (0 - 12.6 SCFM)	172.4 kPa (25 PSI)
Maxtek, Inc.	69.85 mm Diameter by 12.7 mm Length/ 2.75 inch Diameter by 0.5 inch Length	0 - 1.4 SLPM (0 - 0.05 SCFM)	344.7 kPa (50 PSI)
Lee Co.	16.0 mm Diameter by 25.4 mm Length/ 0.63 inch Diameter by 1 inch Length	0 - 0.14 SLPM (0 - 0.005 SCFM)	206.8 kPa (30 PSI)
Cedrat, Tech	63.5 mm Diameter by 76.2 mm Length/ 2.50 inch Diameter by 3 inch Length	0 - 17.8 SLPM (0 - 0.63 SCFM)	103.4 kPa (15 PSI)

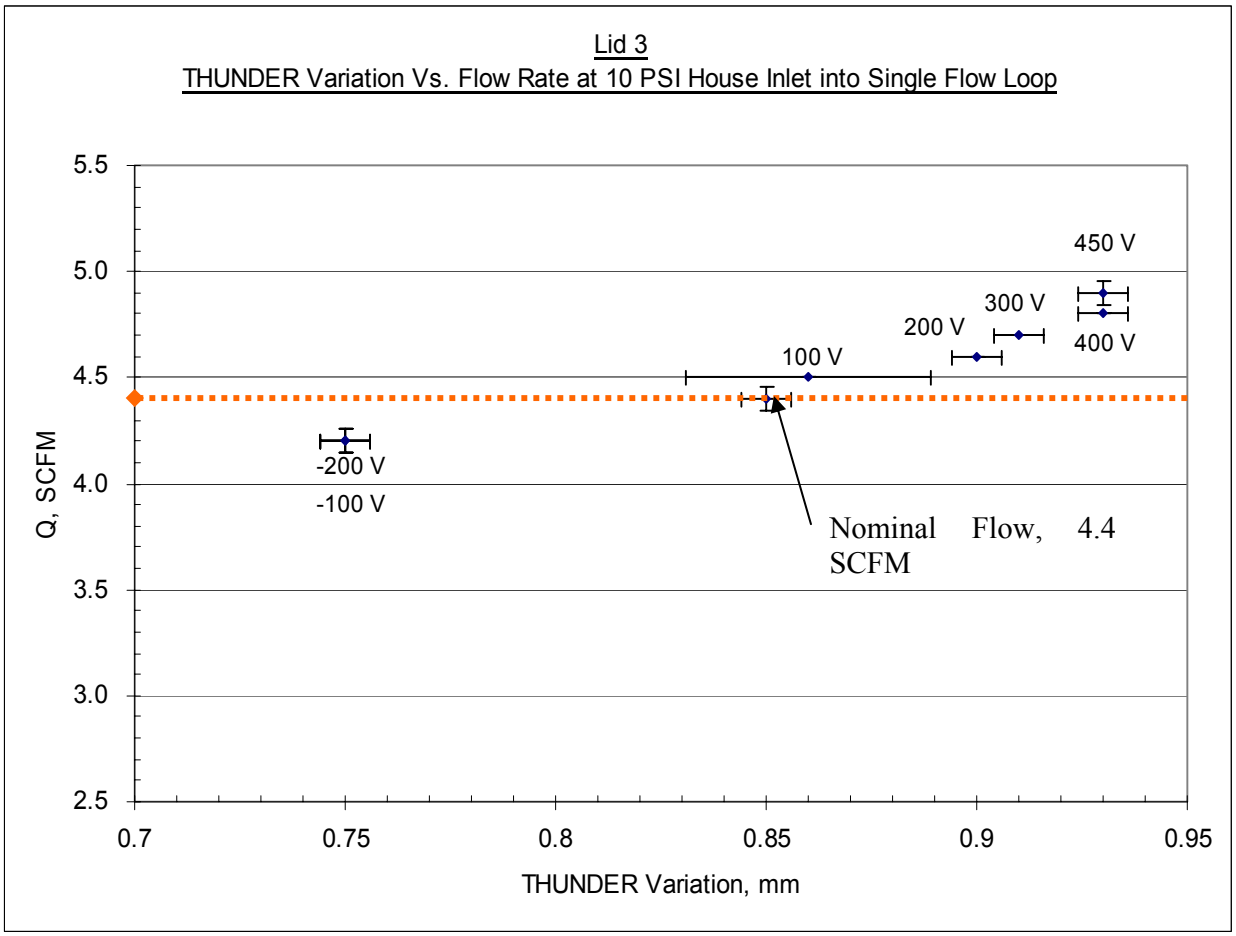

Figure 41. Flow curve for lid 3 at 124.6 SLPM (4.4 SCFM) nominal flow rate, 69.0 kPa (10 PSI) air pressure inlet for single loop flow (Error bars represent standard deviation from 5 trial sample size).

5.6.2 Dual flow loop

Table 10 summarizes the percent flow modulation obtained by operating in a dual flow loop. The actual setup for the dual flow loop remains the same as for the single flow loop, Figure 22, except the bypass valve (GV1) was fully open. With GV1 fully open, an unbalanced condition was obtained in the two paths of the flow loop, and the control valve could then be actuated to determine how much controllability it had over the unbalanced flow.

Table 10 shows the highest percent flow modulation resulted in lid 3 again. From Table 10 it is also seen that the data was insufficient for lids 2 and 3 at the 69.0 kPa (10 PSI) pressure inlet. This behavior was determined to be a result of the valve creating such a high pressure drop. The flow was below the zero limit of the flow meter but was never completely shut off as the float was fluctuating.

Table 10. Dual flow loop summary of maximum percent modulation relative to nominal flow under various inlet pressures (Data shown is percent change from nominal flow).

Lid ID	Inlet Pressure 69.0 kPa 10 PSI	Inlet Pressure 103.4 kPa 15 PSI	Inlet Pressure 137.9 kPa 20 PSI	Inlet Pressure 172.4 kPa 25 PSI
1	-8/+20	-6/+11	-2/+8	-3/+4
2	No Data	-6/+15	-4/+11	-3/+4
3	No Data	-4/+26	-3/+13	-4/+7

Figure 42 shows a 0.15 mm (0.006 in) initial deflection of the actuator at a 65.1 SLPM (2.3 SCFM) nominal flow occurs by using lid 3, and a total percent flow modulation of 30% was achieved for the 103.4 kPa (15 PSI) inlet case. The flow data for lid 3 under these conditions is shown in Figure 43, where the dashed line represents the nominal flow through the valve as well as each data point reflecting the applied voltage intervals. Figure 42 also shows lids 1 and 2 for the 103.4 kPa (15 PSI) inlet case have an initial deflection of 0.1mm (0.004 in) and 0.13mm (0.005 in) respectively.

Figures 44 through 49 show the overall flow performance of each lid and at various inlet pressures. In summary, as the inlet pressure increased, the flow increased. In order to get the highest flow modulation in the dual loop flow, the actuator was preloaded 0.015 mm (0.0006 in) by lid 3 and modulated to its highest capabilities. The standard deviation bars for each flow rate

corresponding to a 5 trial average for each applied voltage data point shown in Figures 44 through 49.

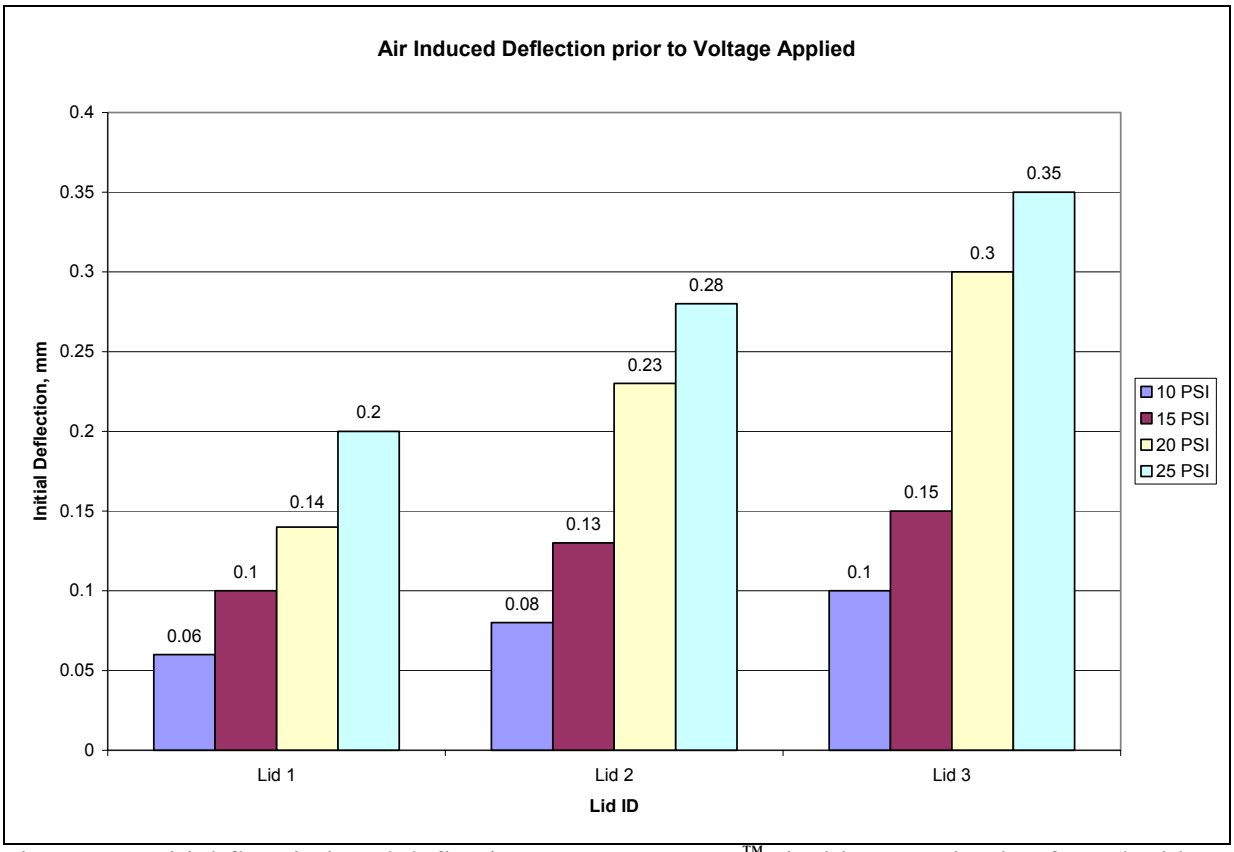

Figure 42. Initial flow induced deflections on THUNDER™ inside control valve for a dual loop configured system.

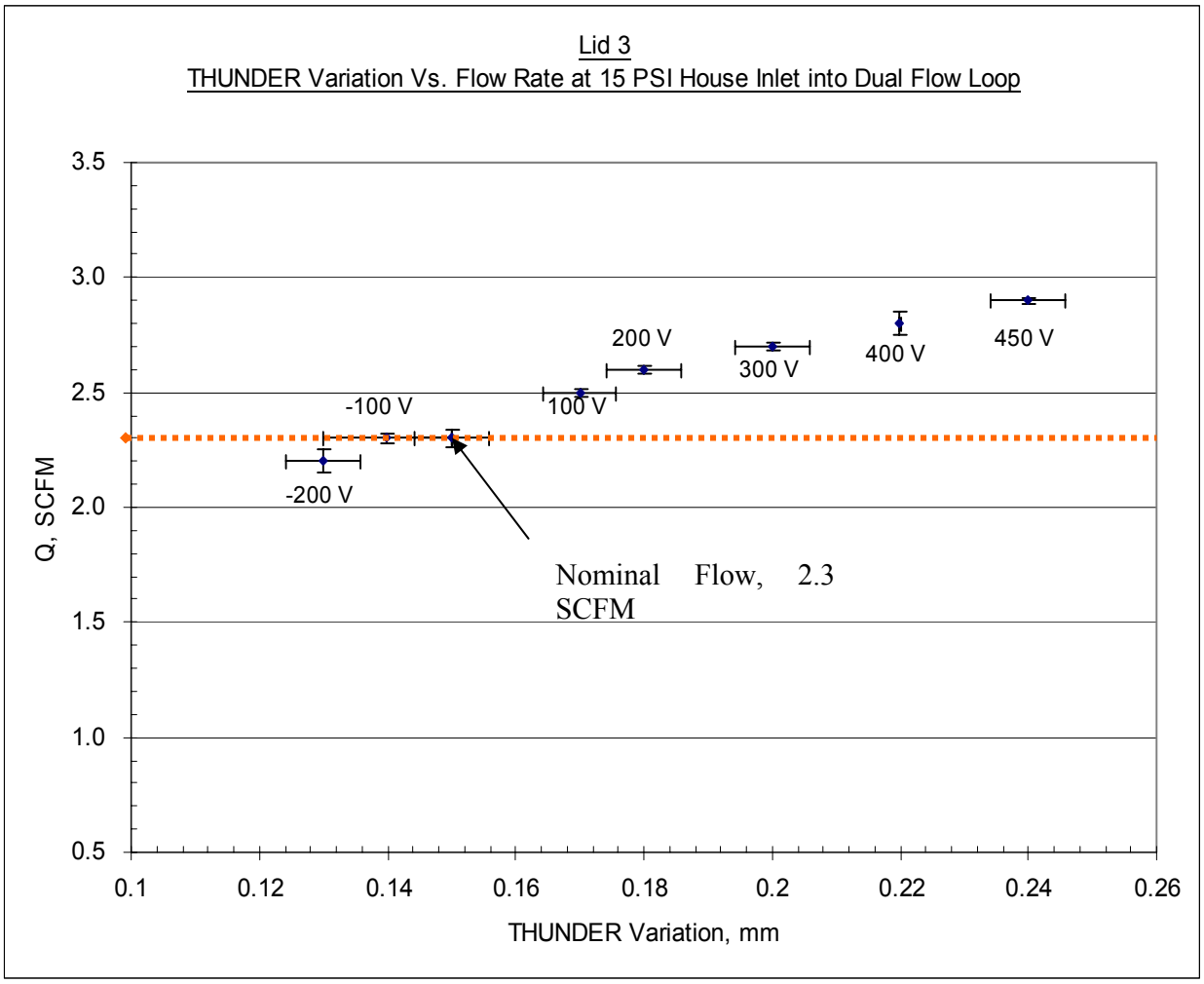

Figure 43. Flow curve for lid 3 at 65.1 SLPM (2.3 SCFM) nominal flow rate, 103.4 kPa (15 PSI) air inlet pressure for dual loop flow (Error bars represent standard deviation from 5 trial sample size).

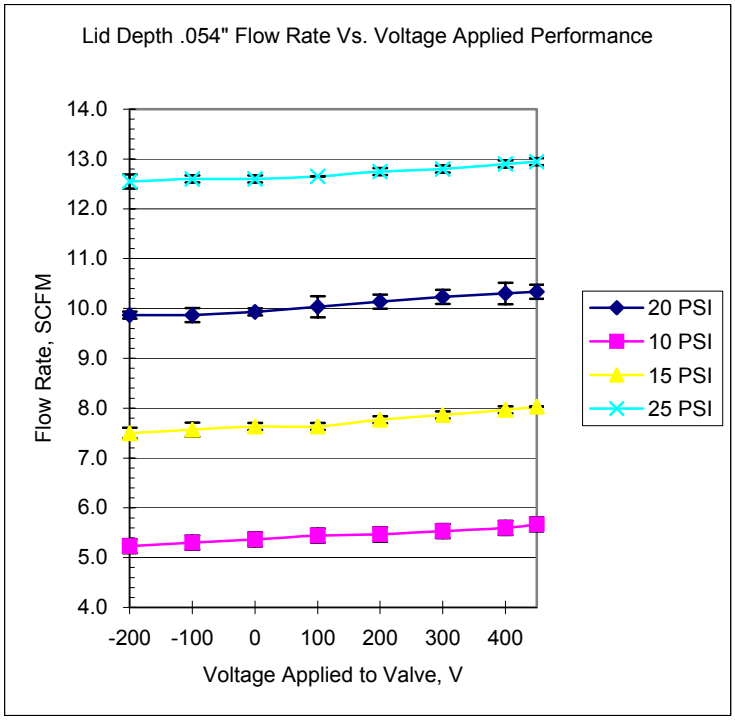

Figure 44. Valve modulation summary for lid 1 in single loop flow (Error bars represent standard deviation from 5 trial sample size).

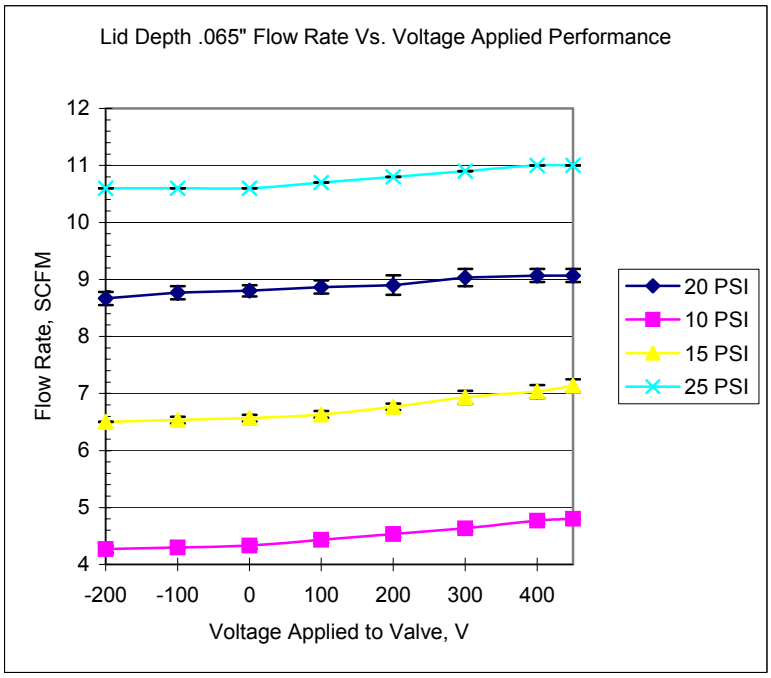

Figure 45. Valve modulation summary for lid 2 in single loop flow (Error bars represent standard deviation from 5 trial sample size).

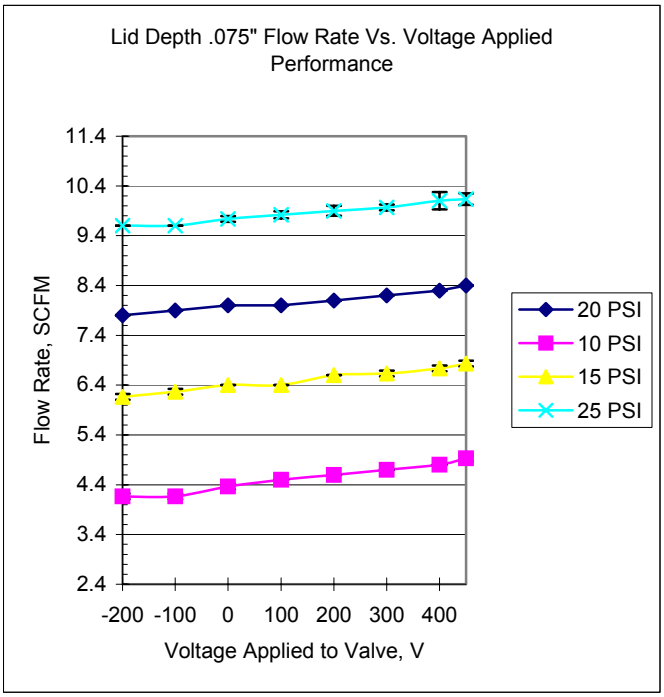

Figure 46. Valve modulation summary for lid 3 in single loop flow (Error bars represent standard deviation from 5 trial sample size).

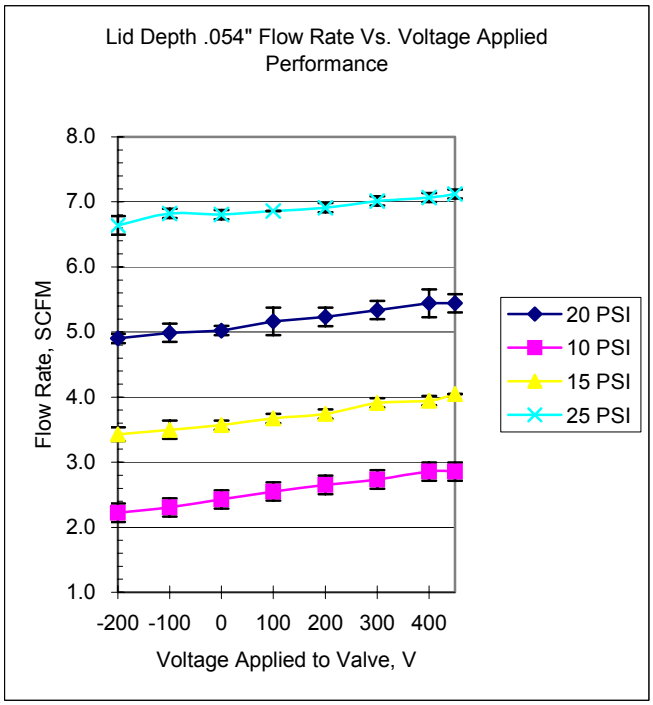

Figure 47. Valve modulation summary for lid 1 in dual loop flow (Error bars represent standard deviation from 5 trial sample size).

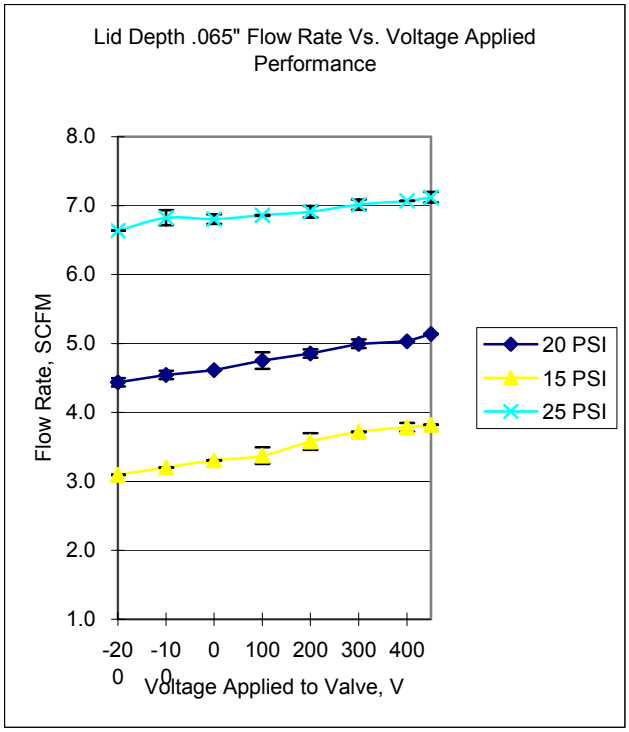

Figure 48. Valve modulation summary for lid 2 in dual loop flow (Error bars represent standard deviation from 5 trial sample size).

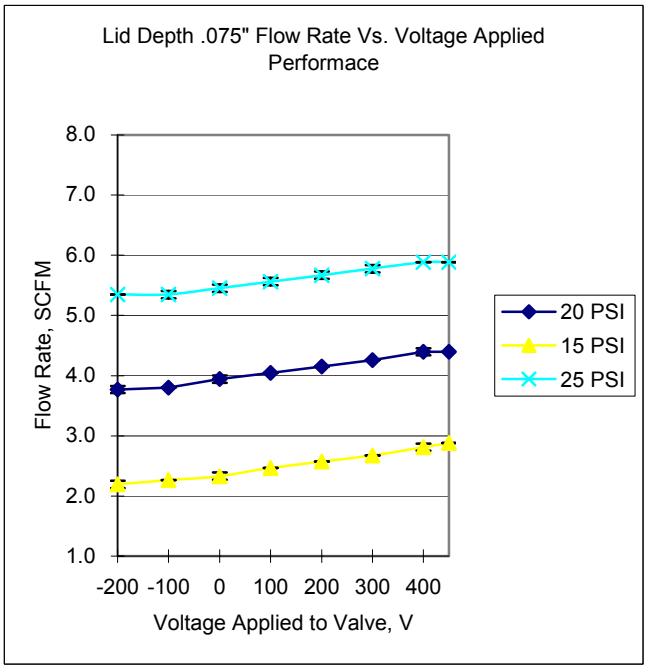

Figure 49. Valve modulation summary for lid 3 in dual loop flow (Error bars represent standard deviation from 5 trial sample size).

All flow measurements for both the single and dual flow loop cases are found in Figures A1 through A22 located in the Appendix. When reviewing Figures A1 through A22, the nominal flow rate occurs when no voltage is applied to the actuator. There is of course a deflection at zero voltage since the nominal flow rate is constant, this is represented as a dashed line on each Figures A1 through A22.

5.6.3 Alternate lid performance

After the results of the rectangular shaped lids in a dual flow loop were completed, two other lid geometries were tested in the dual flow loop setup. Their cross sections, as shown in Figure 15, use a sharp point profile and a curved profile. Their respective results are shown in Tables 11 and 12. Table11 shows changing the lid profile to a sharp point will not increase the total flow modulation from earlier testing. Table 12 shows that the curved surface could make an impact on increasing the overall performance. Both configurations use the initial orifice height of 0.015 mm (0.0006 in).

Table 11. Percent modulation of lid 4 having a sharp point cross sectional depth under various inlet pressures (Data shown is percent change from nominal flow).)

Lid ID	Inlet Pressure 69.0 kPa 10 PSI	Inlet Pressure 103.4 kPa 15 PSI	Inlet Pressure 137.9 kPa 20 PSI	Inlet Pressure 172.4 kPa 25 PSI
4	-4, +6	-3, +7	-4, +5	-1, +4

Table 12. Percent modulation of lid 5 having a curved cross sectional depth under various inlet pressures (Data shown is percent change from nominal flow).)

Lid ID	Inlet Pressure 69.0 kPa 10 PSI	Inlet Pressure 103.4 kPa 15 PSI	Inlet Pressure 137.9 kPa 20 PSI	Inlet Pressure 172.4 kPa 25 PSI
5	0, 0	-4, +22	-3, +21	-2, +6

6.0 DISCUSSION OF RESULTS

A discussion about the results obtained in section 5.0 by using the experimental setup and model implementation in sections 3.0 and 4.0 respectively are presented in the following sub sections.

6.1 ACTUATOR DEFLECTION AS A FUNCTION OF VOLTAGE

The deflection of the actuator as a function of voltage was determined and presented in Figure 25. Using the photonic sensor calibration slope from Figure 25, the apex height "B" (photo shown in Figure 19) decreased as a function of increasing voltage applied to the actuator. In terms of deflection, the positive voltage applied resulted in a deflection away from the probe tip. This was expected since the actuator manufacturer defined this behavior. Figure 25 shows that the actuator had a total deflection of 0.49 millimeters (0.02 inches). The total deflection is defined as the total travel distance resulting from the difference from the highest negative voltage applied at 1.95 millimeter (0.077 inches) to highest positive voltage applied at 1.46 millimeters (0.06 inches). This is of course without any external forces applied to the actuator. It can also be seen that there is some deviation at each data point. The strain deviations do hold a tighter error standard deviation (approximately 1%) than that of the deflection (approximately 5%). The standard deviation of the deflection increases at the extreme drive levels as well. One key feature of Figure 25 to observe is the behavior of the strain. Intuitively, strain should increase when the actuator deflects down, since the substrate is in tension when loaded on the apex. However, as shown in Figure 25, this is not the case. At 200 volts of induced voltage, the

actuator deflects down 0.3 millimeters (0.01 inches) however the strain decreases to –75 microstrain. Thus some non-intuitive relationship between the strain and the voltage applied exists, however the source was not determined.

6.2 ACTUATOR DEFLECTION AS A FUNCTION OF FORCE

Following the actuator's behavior of deflection as a function of input voltage, the behavior of deflection while under a load at the apex was completed and presented in Figure 26. Again, the probe must be calibrated as presented in Figure 24. Figure 26 shows that the height of the apex "B" naturally decreases as weight is applied while the strain increases as well. When weight is applied, the initial height of 1.87 millimeters (0.074 inches) can decrease down to 1.20 millimeters (0.05 inches) depending on the amount of weight applied at the apex. Moreover, as more weight is applied, the strain can increase to 375 microstrain. Contradictory to Figure 25, Figure 26 seems intuitive since the substrate is under tension when a weight is applied. Thus it was determined that the strain gage was properly applied to the actuator for testing. The actuator can still undergo more load however, the maximum of 200 grams (0.44 pounds) was chosen for flow simulation. For example, the highest flow regime applicable in testing never exceeded a total deflection of 1.20 millimeters (0.05 inches).

The strain deviations do hold a tighter standard deviation (approximately 0.5 %) than that of the deflection (approximately, 4%). This is an improvement from the analysis monitoring the deflection as a function of an applied voltage.

6.3 EMPERICAL MODEL OF THE ACTUATOR

The empirical model was useful in the sense that the procedure created could be applied to any other experiment using the output from a strain gage to detect deflection of an actuator in a valve. The measured deflection from the four weight cases compared to the prediction from Equation [5] is presented in Tables 4 through 7. The corresponding plots for each case are shown in Figure 28 through 31. By observing Tables 4 through 7, a significant difference of the measured deflection to the empirical approximation exists. In some instances an absolute difference of 5 to 340 percent exists however differences of up to 1196 percent as well. The larger percent differences are due in part to trying to fit a model very close to the zero variation point. When trying to fit a model to a number relative to zero, keeping the entire sample size is very difficult as it can skew the data. Moreover, it can be seen that as the measured deflection increases from the nominal zero point, regardless of direction from polarity, the overall difference from measured to experimental decreases and the model is more applicable. When observing the overall behaviors in Figures 28 through 31, the empirical approximation is considerably different regardless of the 5 percent error in the measured deflections. This translates to predicting to great of a deflection where a minute amount of deflection from the actuator exists.

Even though the approximation predicted the height and general deflection behavior within the equivalent order of magnitude, an alternative model will be needed if a better accuracy is desired. Possible ways for improving the model could be achieved by removing any outliers that significantly increase the error in approximation. Moreover, a non-linear curve fit may be attempted to see if higher order terms can approximate the deflection better. Since the behavior

of the flow valve summarized for the remaining of the research involved the photonic sensor, empirical modeling was not used.

6.3.1 Additional models of the actuator

Additionally, two deflection comparisons of the actuator were examined to compare the results obtained from published literature. Figure 33 does show the decrease in performance of the actuator when a weight is applied to the surface of the actuator. Note that Figure 33 is analogous to Figure 6, but created for the specific actuator used in this work. Figure 6 did not have any representation of a negative applied voltage. These are the curves to the left hand side of the force axis in Figure 33. Figure 33's work lines are not linear, however the overall behavior can be explained. The families of curves represent the magnitude of voltage applied to the actuator, regardless of polarity. As force is applied to the top surface of the actuator, regardless of the amount of voltage applied, the overall stroke will always decrease. Therefore, whenever the actuator accepts more than 1 Newton (0.22 lb) of force, the overall stroke of 0.49 millimeters (0.02 inches) can decrease to as much as .30 millimeters (0.01 inches). Further application of force causes the overall stroke to decrease more significantly until the point of no deflection is reached. The blocked force was not determined in this research for destruction of the actuator was a concern. Moreover, the standard deviation of the deflection was rather small at 3%. Also note that most of the control or lift capable of the actuator occurs at higher drive levels, but this is generally the region that is the first to lose it's capability of large deflections from an applied force. The steep slopes from the negative applied voltage families are a result of actuator's inherent properties. The highest negative applied voltage was –200 volts, as soon as an external

force is applied, the ability to oppose that force deteriorates fast since the ceramic doesn't have the inherent ability to lift large forces.

The Weinman model, as shown in Figure 34, was also useful in the sense of observing a linear behavior of deflection as a function of voltage. Weinman's model is valid for low drive, within the -100 to 150 volt range, under fixed – sliding boundary conditions. Weinman's test used the same actuator, model 8R, as implemented and tested in this research. Note that Figure 34 has the same slope of Figure 25 in that Figure 25 shows the height deflection relative from "B". By using the high drive level regime, 450 to -200 volt range, a slope of -0.00737 mm/volt (-0.00029 in/volt) was determined as compared to the -0.005588 mm/volt (-0.00022 in/volt) slope determined by Weinman. Relative to Wenmann is 24 percent different as shown in Figure 34. This can be attributed to the high drive levels where the separation from their respective displacements occurs.

6.4 RESULTS OF THE DOWNSTREAM GATE VALVES

Determining the effects of adjusting the downstream gate valves, GV1 and GV2 in Figure 22, was also useful in the sense that optimal operating conditions for the valves were determined. Downstream adjustability was also very helpful to transition between single and dual loop flow conditions. When considering the single flow case, Figure 35, each adjustment of GV2 had a minimal affect on the flow controllability performance of GV3. The only position of concern would be the case where the downstream gate valve, GV2, was opened for only a half revolution. The respective line had a lower slope than the rest of the data. This is even less desirable in that the same orifice area fluctuation for all data sets would yield a lower fluctuation in flow. For that reason, GV2 was set to full open (2.5 revolutions). When GV3 is removed and replaced by the

control valve, the goal is to create enough of a pressure drop to achieve a nominal flow in the desired flow range. This will assure adequate flow controllability. If the control valve implemented didn't create enough pressure drop, then the valve flow would be in the undesirable region and the change in orifice area wouldn't result in a change in flow. Figure 35 shows that a nominal flow rate of 124.6 SLPM (4.4 SCFM) for single loop flow is desirable since that is the location of the steepest portion of the control curve as determined by GV2. GV2 controlled the flow 100% since it could completely shut off air flow and allow for full flow when fully opened. Naturally, the control valve will be somewhere below this number. The important behavior to note is when GV3 varies from fully closed to 1 revolution open. 1 revolution open on this gate valve measures approximately 1 millimeter (0.04 inches) in height. Thus if the actuator in the control valve can modulate in the region of 1 millimeter (0.04 inches), substantial flow modulation is possible.

When dual flow loop conditions are considered, balanced flow was desired prior to analyzing the control valve and GV3. Setting GV1 and GV2 to full open, balanced flow is obtained by allowing maximum flow through each flow path. This was achieved by observing the behaviors in Figures 36 and 37. Figure 36 shows the maximum flow at approximately 339.8 SLPM (12 SCFM). The diversion path (Figure 38) was also decreased from a maximum flow of 291.7 (10.3 SCFM) to 170 (6 SCFM). However, this is for the case where GV1 is half a revolution open where its corresponding curve was much less than the balance of the family of curves which was undesirable. With GV1 at one and a half revolutions opened, the maximum flow is reduced to 226.5 SLPM (8 SCFM) in Figure 37, with the bypass line (Figure 39) deceasing from 382.3 SLPM (13.5 SCFM) to 226.5 SLPM (8 SCFM). This is the condition at which balanced flow is achieved. The flow rate through GV2 decreased due to the diversion

effect, but the slopes in Figures 36 and 37 are still similar to the single flow loop case shown in Figure 35. The reciprocating flow effect is inherent in parallel flows, each individual line is added to arrive at the total flow. Therefore, a change in flow on one line will result in the reciprocal change in the other.

To better understand the desired operating range, Figures 44 through 49 can be compared to the controllable regions within Figure 35 and 37 respectively. For single loop flow (Figures 44 through 46), flows range from 110.4 SLPM (3.9 SCFM) to 368.1 SLPM (13.0 SCFM). Figures 44 through 47 showed that some of these flows may be operating in the undesirable region in Figure 35 which is a concern and would need to be addressed. For dual loop flow (Figures 47 through 49), flows ranged from 62.3 SLPM (2.2 SCFM) to 198.2 (7.0 SCFM) which is near the base of the undesirable region in Figure 36. This was caused by the orifice height becoming large enough to allow for a maximum flow through the valve. Even though the downstream valves (GV1 and GV2) were left a full open, perhaps their settings could have been adjusted (0.5 revolutions open) to see if the flow could have be forced to operate in the desirable flow region.

6.5 THE CONTROL VALVE MODULATION RESULTS

With the control valve implemented into single and dual loop flow conditions, a discussion about each case in conjunction with the different lids implemented is presented.

6.5.1 Single loop flow

Even though 1 millimeter of stroke under flow conditions from the control valve was the goal, a maximum deflection of 0.2 millimeters (0.008 inches) still showed desirable flow modulation results as shown in Figure 41. The greatest flow performance of the control valve used lid 3 for

both single and dual flow loops. All percent modulation results can be seen in Table 8 in relation to each corresponding lid. In Table 3, lid 3 was defined as having an orifice height of 0.015 mm (0.0006 in) into the flow channel. Thus prior to applying any inlet pressure, lid 3 reduced the initial apex height of 1.880 mm (0.074 in) to 1.63 mm (0.064 in) as shown in Figure 42. Thus, lid 3 produced 16, 9, 8 and 5 percent modulation from nominal for each incremental air inlet pressure of 69.0, 103.4, 137.9 and 172.4 kPa (10, 15, 20 and 25 PSI), respectively. The bypass gate valve, GV1, was completely shut off so no flow rate was observed. During operation, numerous vibrations occurred inside the valve. This could attribute to loose boundary conditions on the exit end of the valve. Regardless, the vibration was ignored during operation because with such unrepeatable performance, fine-tuning was not possible.

6.5.2 Dual loop flow

For dual loop flow lid 3 produced 0, 30, 16 and 11 percent modulation for each incremental air inlet pressure of 69.0, 103.4, 137.9 and 172.4 kPa (10, 15, 20 and 25 PSI), respectively. As the orifice area increased, the percent modulation decreased for both single and dual loop flow conditions, except for the 69.0 kPa (10 PSI) inlet. The performance for lids 1 and 2 were less than that of lid 3. All flow curves, Figures A1 through A22, contain the nominal flow point at zero voltage applied. This can be seen as the 3rd data point from the left hand side of each figure. The voltage point for each case from the left hand side is –200, -100 and 0 respectively. Thus, by examining all flow curves in detail, the initial deflections as well as the modulating performance for each flow loop and lid are available in the Appendix.

At lower inlet pressures, the air flow control valve has greater flow modulation than that of higher inlet pressures. Thus for higher inlet pressure and nominal flow rates, the stroke of the actuator is suppressed and then the total modulation is suppressed as well. Take note of lid 3's

highest total flow modulation at 30% (Table 10). This occurs at the lowest air inlet pressure of 103.4 kPa (15 PSI), which was the lowest recordable point since 69.0 kPa (10 PSI) wasn't obtained. The optimum sensitivity in flow through the cross section occurs when a preload is applied prior to voltage application. Thus a preload on the actuator increases the pressure drop across the valve and allows the nominal point of operation to be even closer to half way up the linear portion of the desirable operating range shown in Figure 37. The total percent modulation falls roughly 60% for pressure inlets of up to 172.4 kPa (25 PSI).

The flow through GV1 was not recorded during testing due to the 7520's resolution, but the overall behavior was intuitive as shown in Figures 38 and 39.

6.6 ALTERNATE LID PERFORMANCE

In addition to the rectangular cross sections, two other lids were implemented as discussed in section 5.6.3. Even though the lid 3 height was the only height tested for these concepts, the overall performance was acceptable in that flow modulation was achieved, however the magnitude was not larger than lids 1 through 3 except for one area of interest. Table 12 shows that under a 137.9 kPa (20 PSI) inlet pressure a 24 percent flow modulation of a nominal flow rate of 110.4 SLPM (3.9 SCFM) are achieved. This is significantly higher than it's respective point in Table 10.

6.7 SUMMARY

Thus the control valve allowed for higher flow to be controlled than that of the current piezoelectric valves available in open literature. Table 9 shows that the footprint and operating

pressure are still in the equivalent pressure range, however neither Maxtek, Lee, or Cedrat can come close to operating in such a high flow environment of 356.8 SLPM (12.6 SCFM).

6.8 SCALING

Initially it was determined that house air would be used for testing. After air testing was complete, scaling on the current model was done to determine the equivalent flow of other gases that may be used. An example is given to scale for methane.

Equation [7] shows the volumetric flow conservation law for gaseous media. In this case, it is air with respect to methane (CH_4).

$$VolumetricFlowRate = \rho_{Air} Q_{Air} = \rho_{CH_4} Q_{CH_4} \quad [7]$$

Equation [8] shows Equation [7] in terms of solving for the equivalent flow rate of methane. Equation [8] determines the actual magnitude of methane achieved in flow environments of room temperature and pressure of 172.4 kPa (25 PSI). Note that the density of methane is roughly 50% less than that of air so naturally the flow of methane will be greater than that of air.

$$Q_{CH_4} = \left(\frac{\rho_{Air}}{\rho_{CH_4}} \right) Q_{Air} \quad [8]$$

$$Q_{CH_4} = \left(\frac{1.22 kg/m^3}{0.66 kg/m^3} \right) \frac{12.6 ft^3}{\min} = 23.85 \text{ SCFM Air} \quad [9]$$

With the current range of airflow at 121.8 SLPM (4.3 SCFM) to 356.8 SLPM (12.6 SCFM), an equivalent methane flow range of 223.7 SLPM (7.9 SCFM) to 675.4 SLPM (23.8 SCFM) can be achieved.

7.0 CONCLUSIONS AND FUTURE WORK

In conclusion, a gas flow control valve incorporating a high deflecting piezoelectric actuator called the THUNDER™ was presented and proved to be a success in the quest for producing a compact valve that could operate in a moderate pressure and high flow environment. With deflections as high as 0.2 millimeters (0.01 inches) inside the chamber during operation and flow modulations as high as 30% in a dual loop flow, the next goal would be to achieve a higher flow modulating performing actuator in an elevated temperature environment.

When considering the empirical model created in section 5.4, the model could be improved since percent differences fluctuated from to 5% to 213% but could be eliminated if further analysis is done to eliminate outliers (areas where percent differences that were greater than 500%) or increase the equation's order of magnitude. Depending on accuracy requirements of the user, the percent differences displayed in Tables 4 through 7 might be too great thus each individual point was listed for future modeling approximation. Moreover, the blocked force, which is not shown in Figure 33, could have been determined and compared to that of the manufacturer's publish data.

Even though the actuator has low force generation seen during the control valve testing, this actuator can be configured to increase force by instituting a stacking technique. Stacking the THUNDER™ in layers will allow for more force generation, however the displacement should not change, although some decrease may be exhibited depending on how well the stack is produced. Figure 51 is a photo of an experimental setup of how to construct a stack actuator

using THUNDER™ 7R's. Thus performing deflection analyses on a stacked THUNDER™ alone would be grounds for possible improvement. Implementing a stacked THUNDER™ into a control valve should be advantageous. Using a stacked configuration to achieve high force ability on the actuator would enable deflection at higher inlet pressure where the current valve can not operate.

It has been concluded that lid 3 had the highest flow modulation percentage. However as shown in Table 12, the curved orifice surface does have some impact on increasing the total flow modulation since 24 percent at a 137.9 kPa (20 PSI) inlet was higher than that of the 16 percent obtained for the same inlet pressure in Table 10 for the dual flow loop case. Further increasing the depth of the lid into the flow channel could be a source of improved performance, particularly for the curved cross-sectional profile. Several of the nominal flow rates were in the undesirable flow control region as shown in Figures 35 and 37 in conjunction with the results from Figures 44 through 49. 0.5 revolution open settings of GV1 and GV2 may be investigated to monitor the impact of the lids at higher inlet pressures. In addition, the bypass flow, GV1, can be recorded to monitor the bypass flow line behavior during dual flow loop testing. The bypass line flow, GV1, was not recorded during dual flow loop testing once the down stream gate valve fully opened setting was chosen. The behavior was observed as behaving normal as shown in Figures 38 and 39, but not recorded since the 7520 flow meter's resolution wasn't low enough to record a precise value.

Another orifice geometry to consider would be one that has a Venturi shape entrance as the one shown in Figure 50.

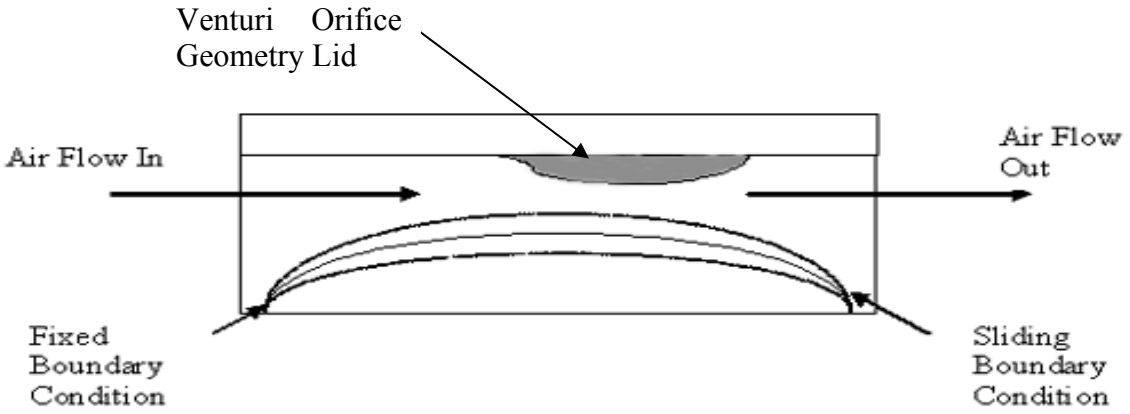

Figure 50.Venturi shape orifice lid geometry.

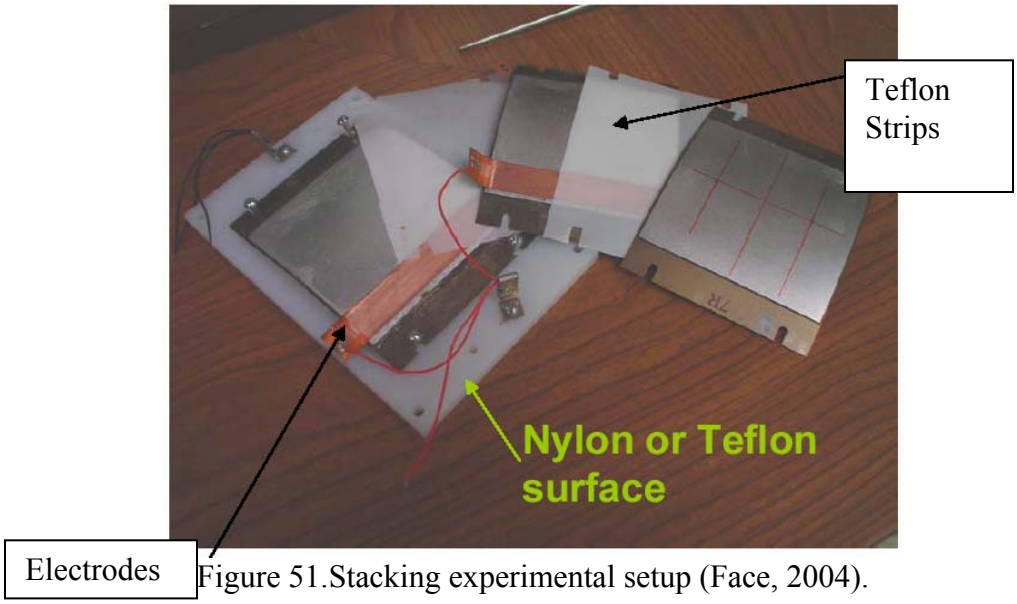

Figure 51.Stacking experimental setup (Face, 2004).

Attaching pressure ports into the inlet and outlet of the cross sectional area within the control valve would be beneficial as well. One could calculate the valve coefficient, C_v, and adjust the desired cross section accordingly and achieve more controllability.

Temperature testing of the THUNDER™ actuator itself could be done. Only one paper was found on high temperature testing of this actuator however the actuator was a different model and mounted differently (Mossi, 2002). In this research, the mountings were always fixed-sliding where as Mossi implemented fixed-free cantilever mounting, which leads to an obvious different performance since cantilever loading has the ability to deflect much higher but can generate lower force.

The last area of research could be spent on scaling the system of flow in order to determine which area of operation one would need to implement such a valve. Even though this valve operates at room temperature with only flow modulation for various inlet pressures, the valve could be optimized for custom design where an optimal point could be determined. This optimal point could be requested for higher modulation at lower inlet pressures or low modulation at higher inlet pressures. If scaling was taken into account, the valve could be tested at room conditions for simulation and later on at the actual conditions of implementation. The advantage of this involves safer testing as well as more available resources as opposed to high temperature conditions, chambers, and various gas supplies.

This is the first control valve using the THUNDER™ actuator. By instituting this actuator in a control valve and completing the test set forth in this thesis, literature is now readily available to aid in the research for manufacturing piezoelectric flow control valves for various gas applications.

APPENDIX

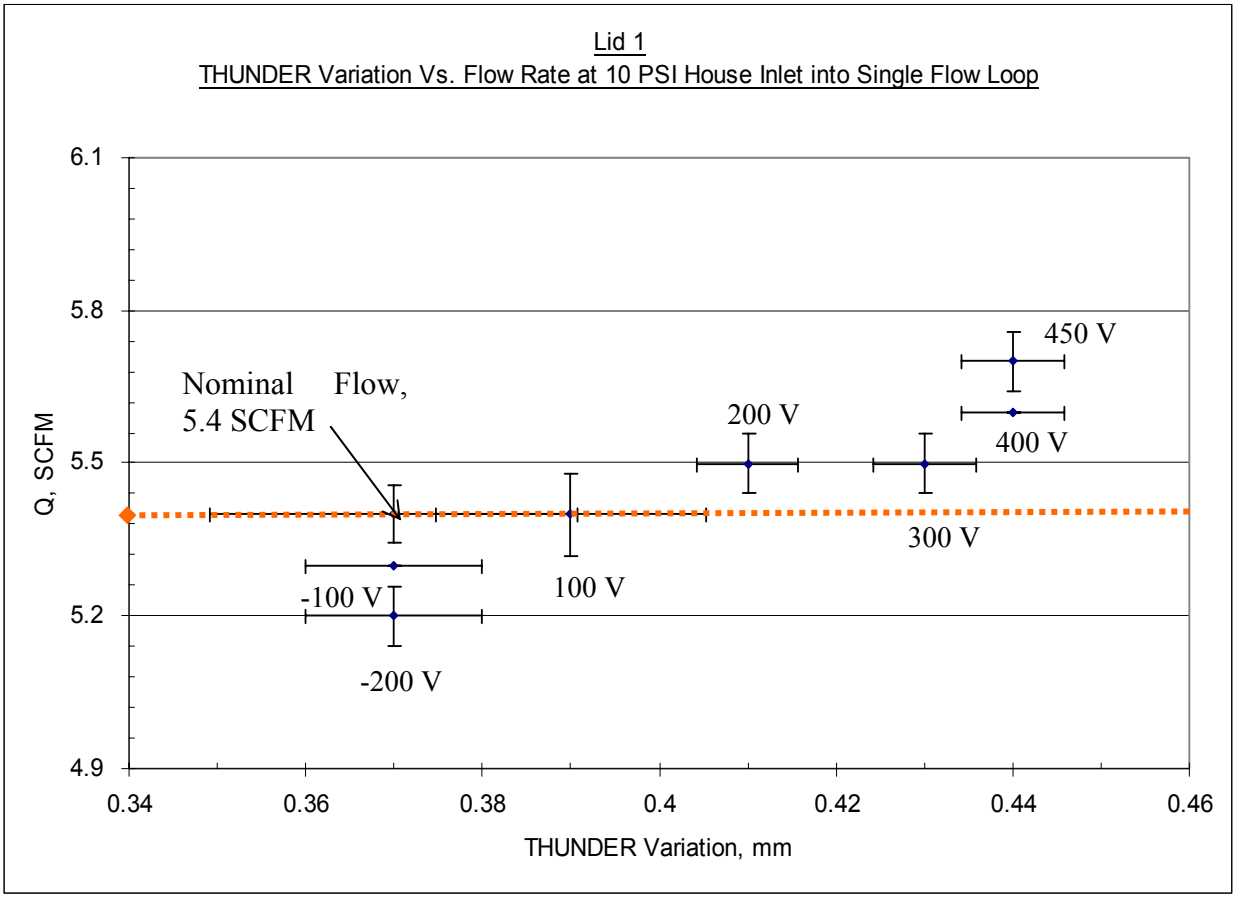

Figure A1. Flow curve for lid 1 at 152.9 SLPM (5.4 SCFM) nominal flow rate, 69.0 kPa (10 PSI) air inlet pressure for single loop flow (Error bars represent standard deviation from 5 trial sample size).

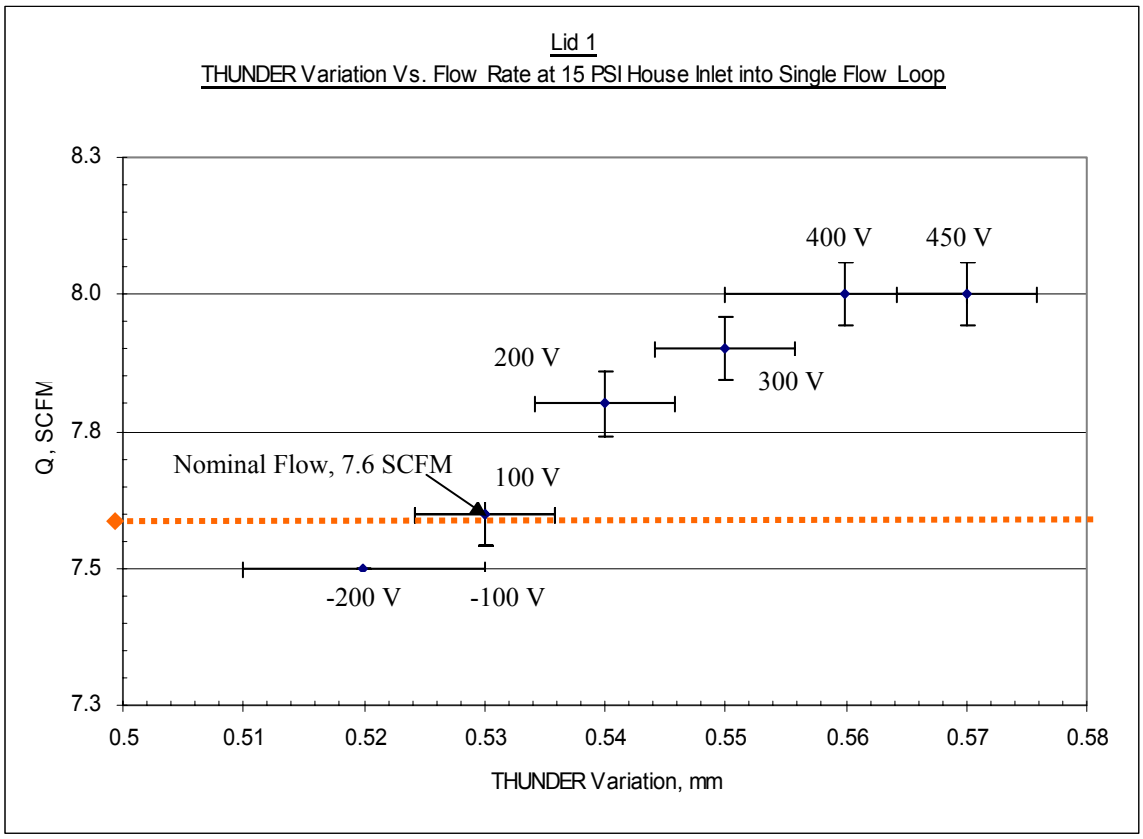

Figure A2. Flow curve for lid 1 at 215.2 SLPM (7.6 SCFM) nominal flow rate, 103.4 kPa (15 PSI) air inlet pressure for single loop flow (Error bars represent standard deviation from 5 trial sample size).

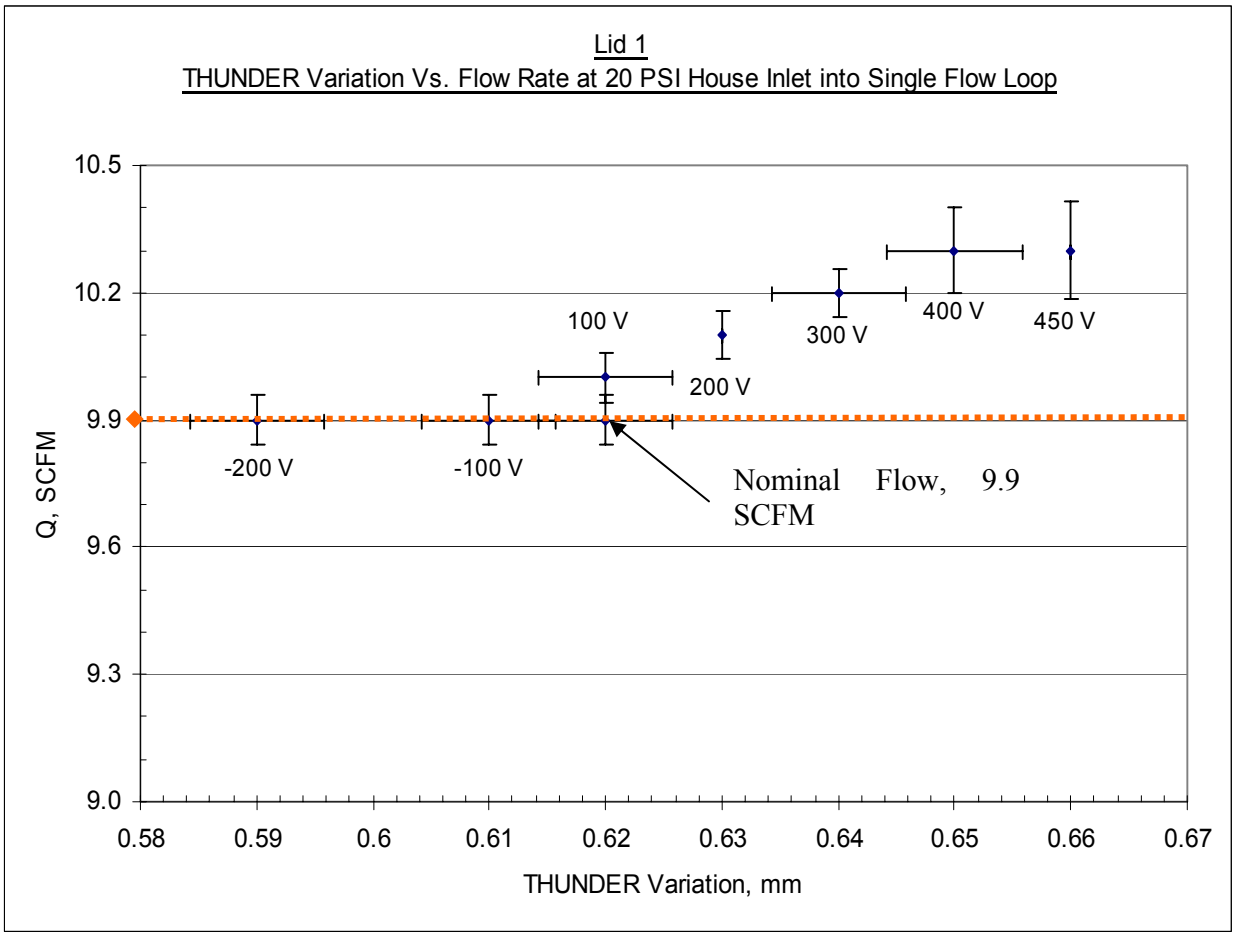

Figure A3. Flow curve for lid 1 at 280.3 SLPM (9.9 SCFM) nominal flow rate, 137.9 kPa (20 PSI) air inlet pressure for single loop flow (Error bars represent standard deviation from 5 trial sample size).

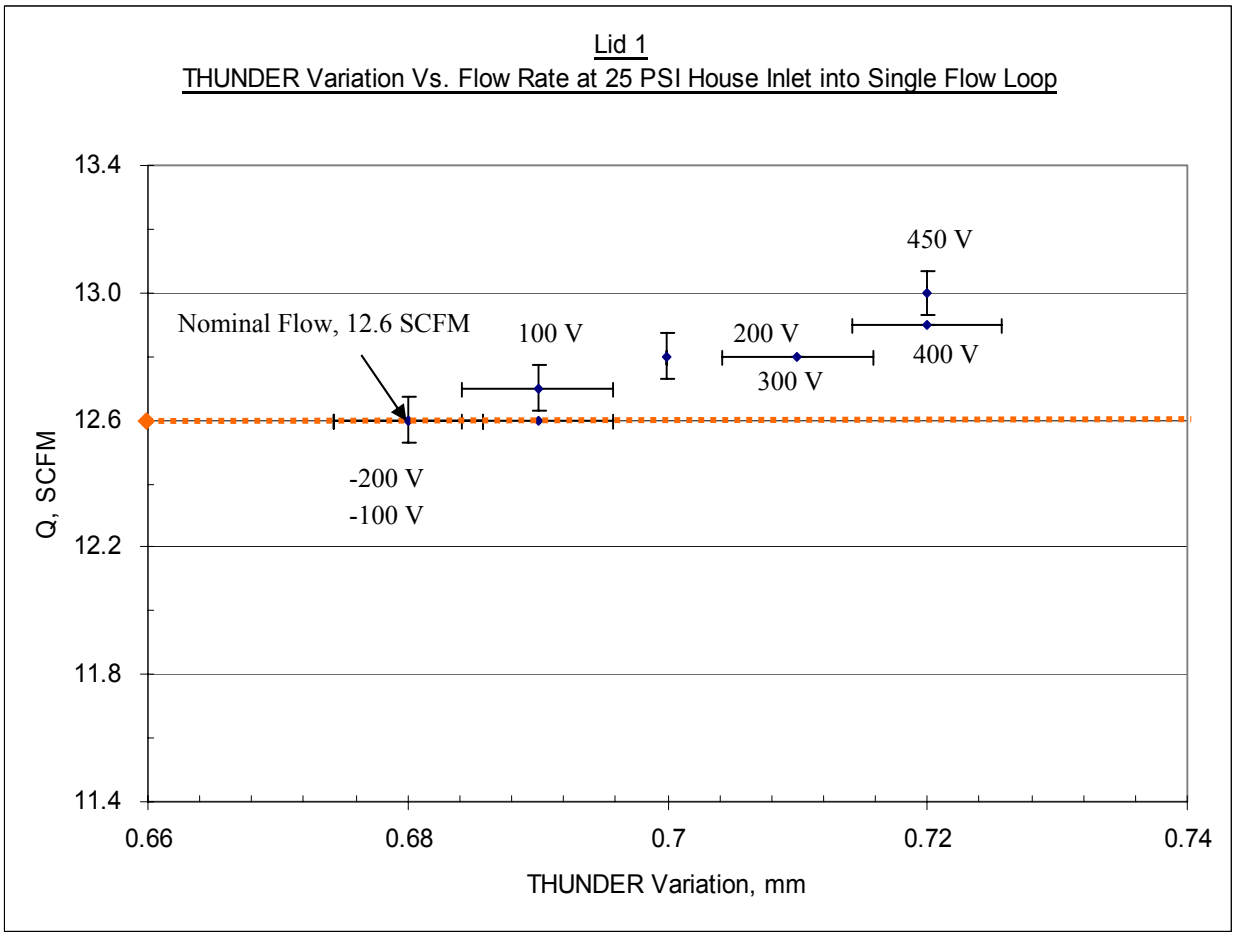

Figure A4. Flow curve for lid 1 at 356.8 SLPM (12.6 SCFM) nominal flow rate, 172.4 kPa (25 PSI) air inlet pressure for single loop flow (Error bars represent standard deviation from 5 trial sample size).

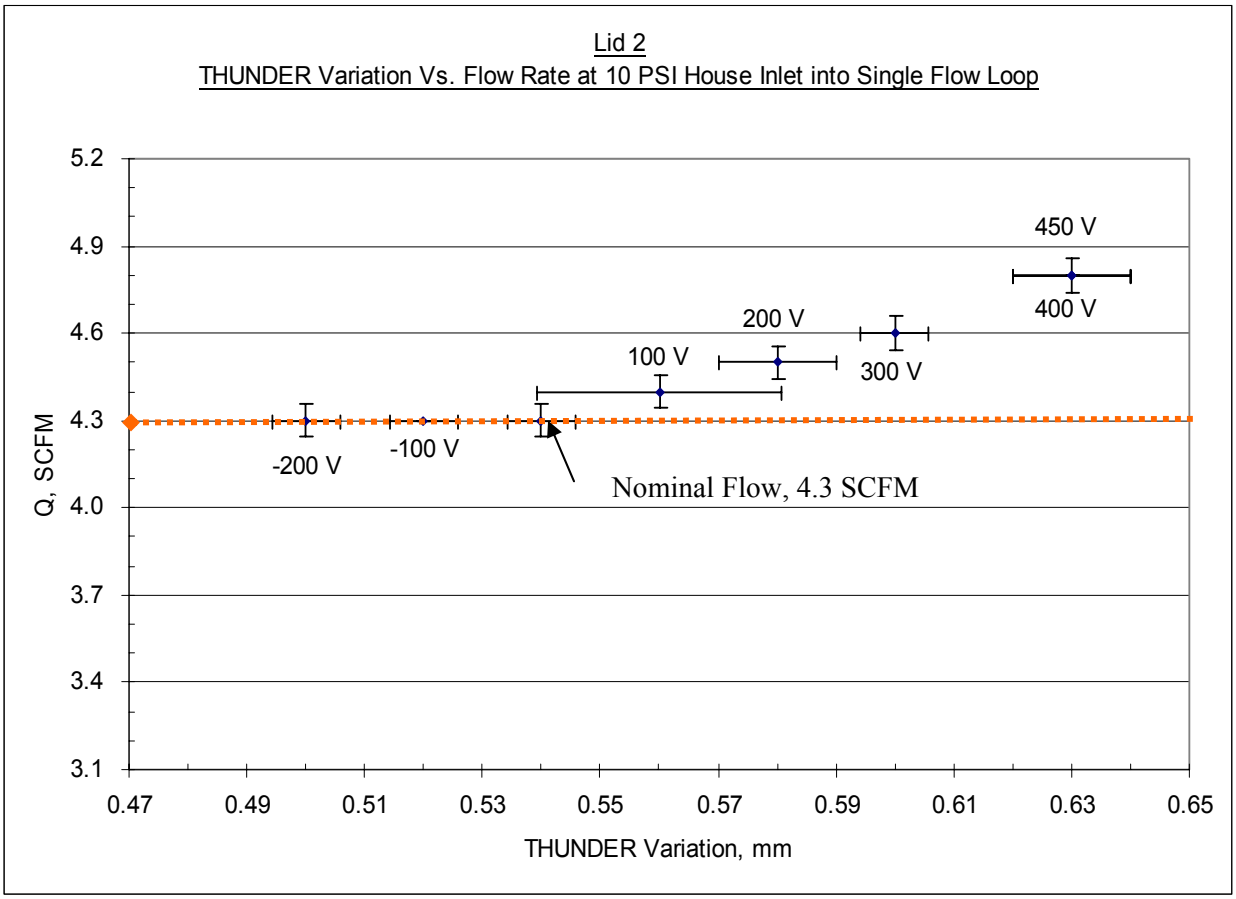

Figure A5. Flow curve for lid 2 at 121.8 SLPM (4.3 SCFM) nominal flow rate, 69.0 kPa (10 PSI) air inlet pressure for single loop flow (Error bars represent standard deviation from 5 trial sample size).

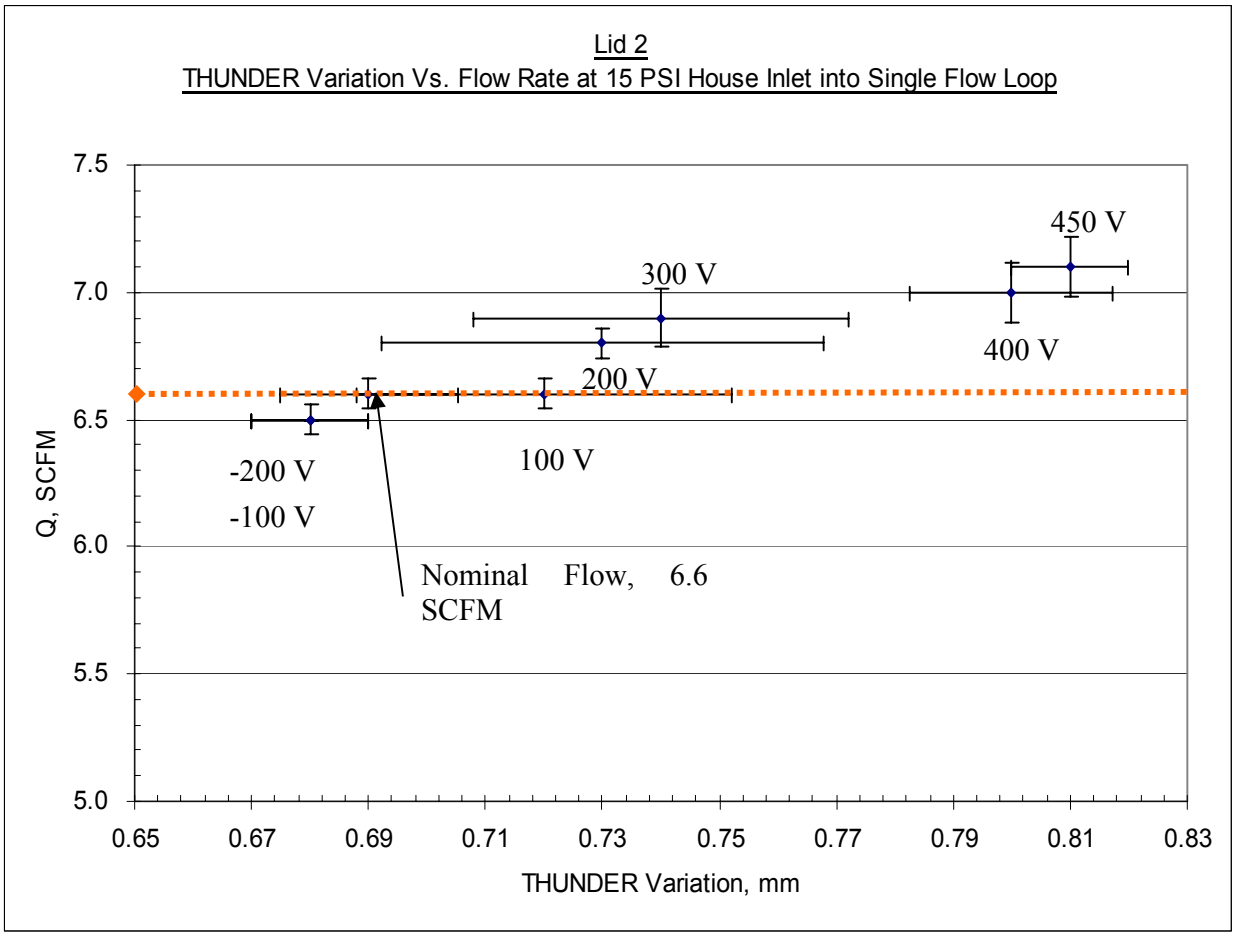

Figure A6. Flow curve for lid 2 at 186.9 SLPM (6.6 SCFM) nominal flow rate, 103.4 kPa (15 PSI) air inlet pressure for single loop flow (Error bars represent standard deviation from 5 trial sample size).

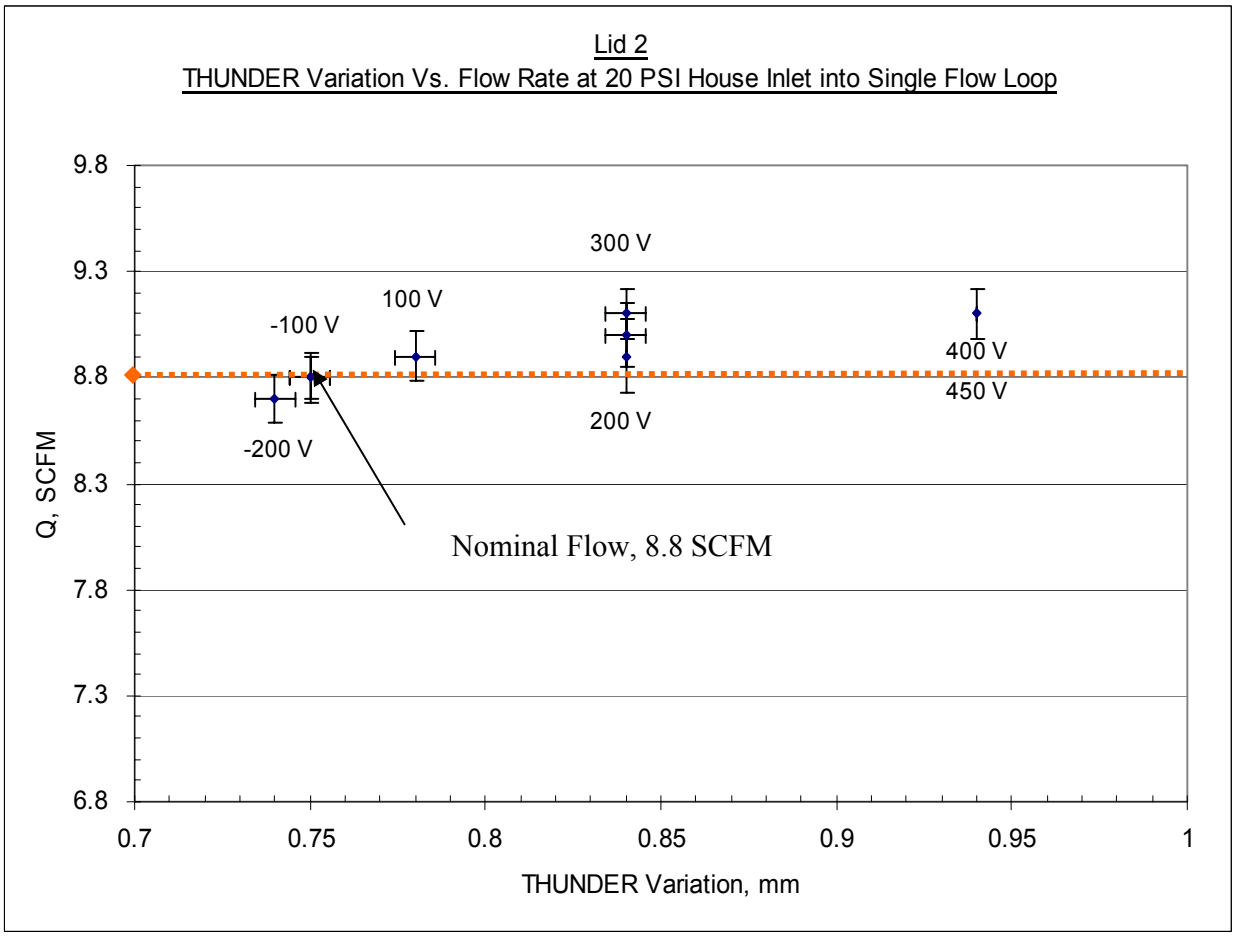

Figure A7. Flow curve for lid 2 at 249.2 SLPM (8.8 SCFM) nominal flow rate, 137.9 kPa (20 PSI) air inlet pressure for single loop flow (Error bars represent standard deviation from 5 trial sample size).

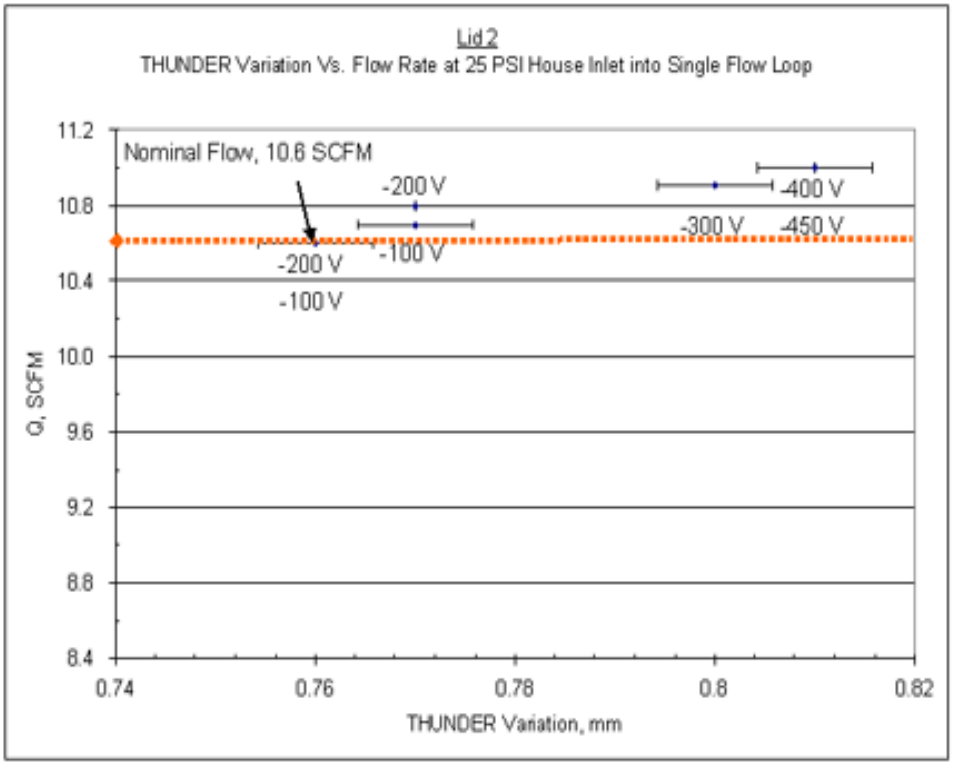

Figure A8. Flow curve for lid 2 at 300.2 SLPM (10.6 SCFM) nominal flow rate, 172.4 kPa (25 PSI) air inlet pressure for single loop flow (Error bars represent standard deviation from 5 trial sample size).

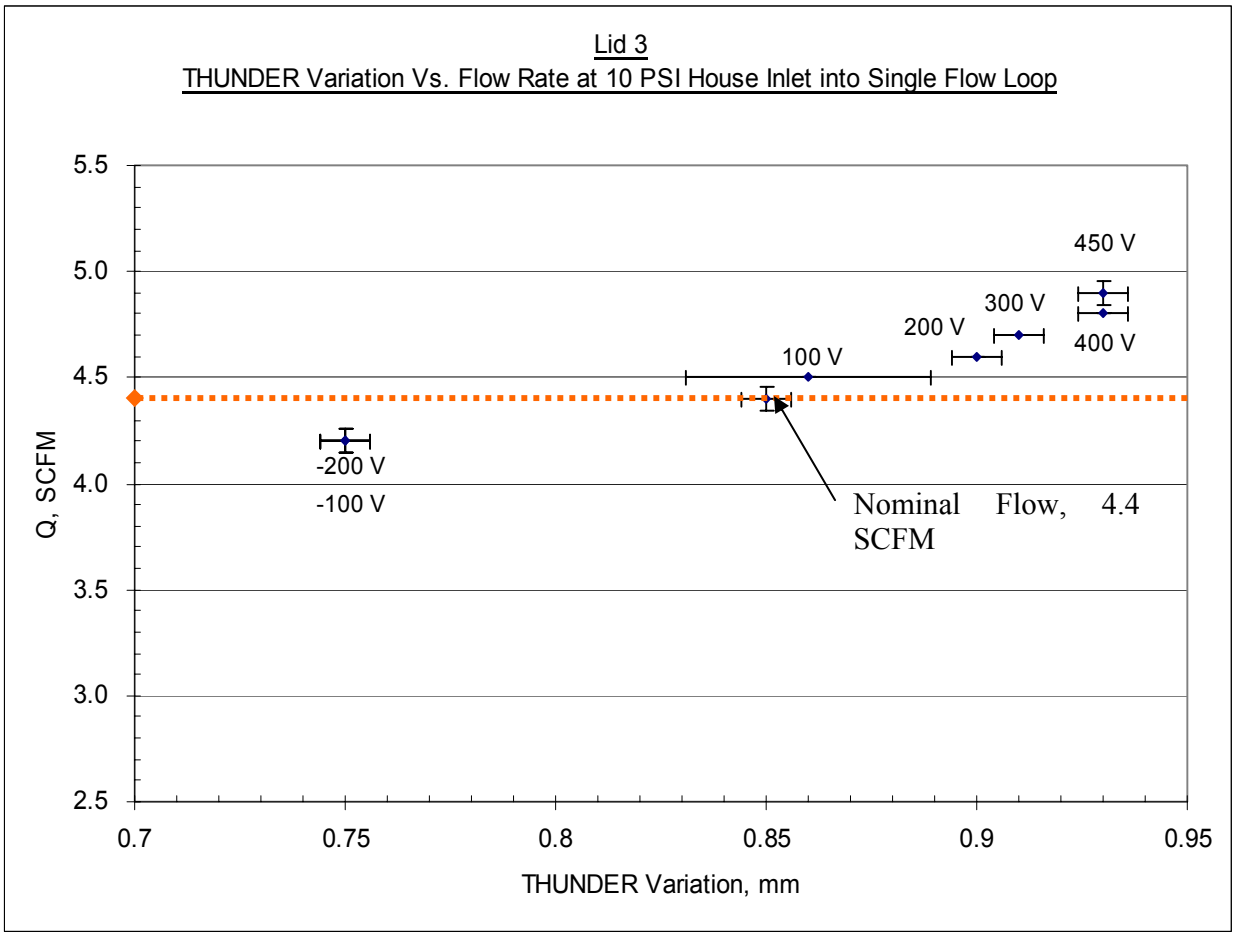

Figure A9. Flow curve for lid 3 at 124.6 SLPM (4.4 SCFM) nominal flow rate, 69.0 kPa (10 PSI) air inlet pressure for single loop flow (Error bars represent standard deviation from 5 trial sample size).

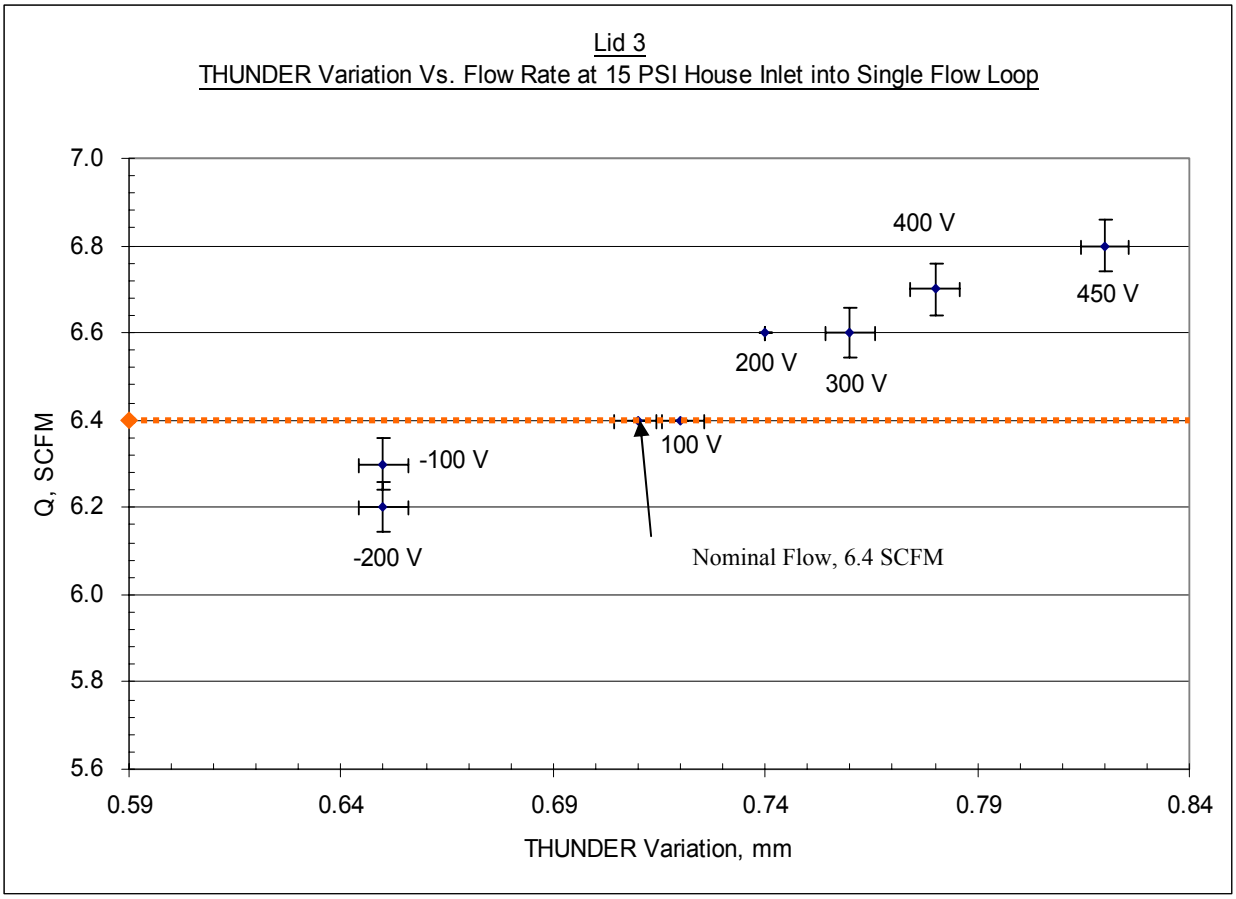

Figure A10. Flow curve for lid 3 at 181.2 SLPM (6.4 SCFM) nominal flow rate, 103.4 kPa (15 PSI) air inlet pressure for single loop flow (Error bars represent standard deviation from 5 trial sample size).

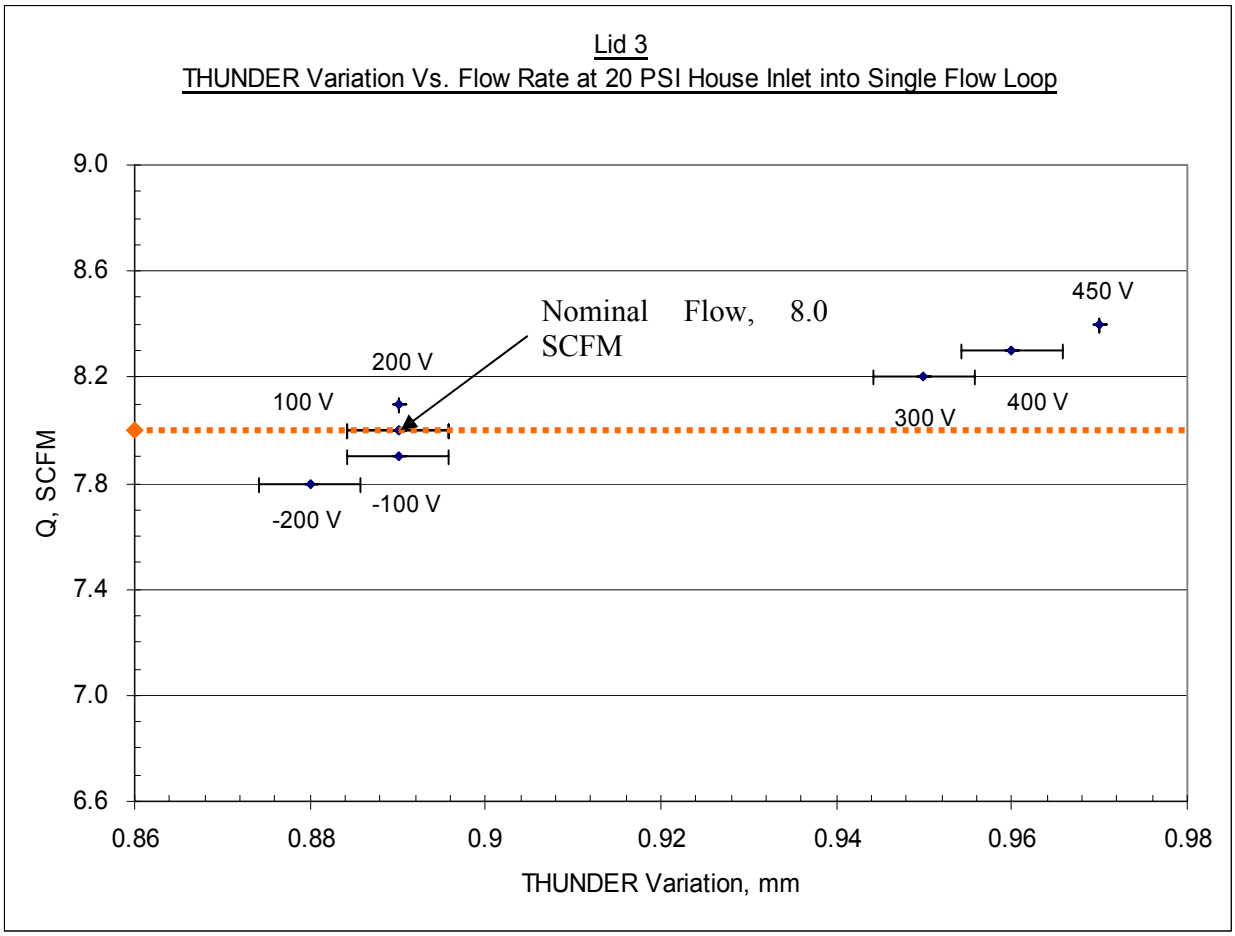

Figure A11. Flow curve for lid 3 at 226.5 SLPM (8.0 SCFM) nominal flow rate, 137.9 kPa (20 PSI) air inlet pressure for single loop flow (Error bars represent standard deviation from 5 trial sample size).

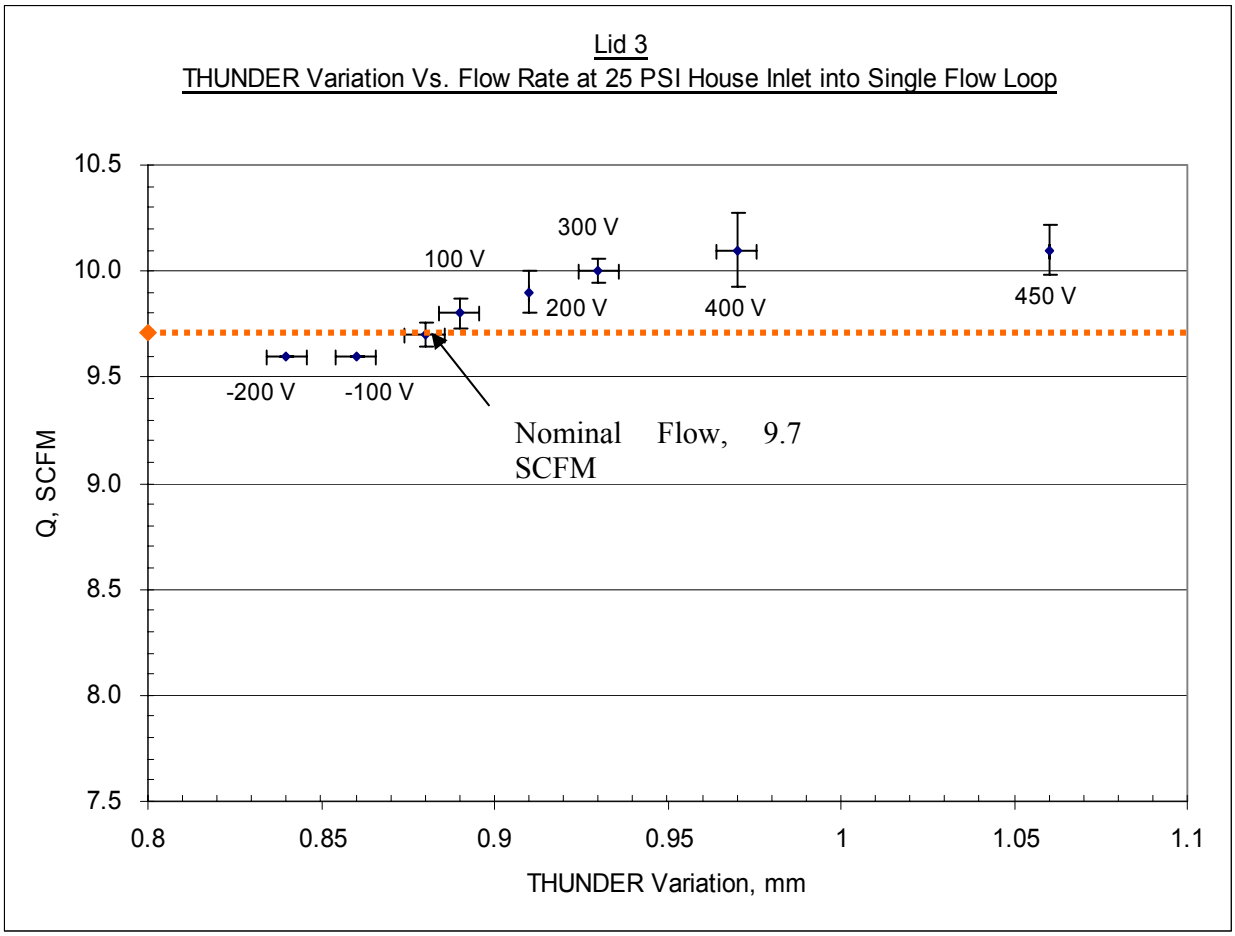

Figure A12. Flow curve for lid 3 at 274.7 SLPM (9.7 SCFM) nominal flow rate, 172.4 kPa (25 PSI) air inlet pressure for single loop flow (Error bars represent standard deviation from 5 trial sample size).

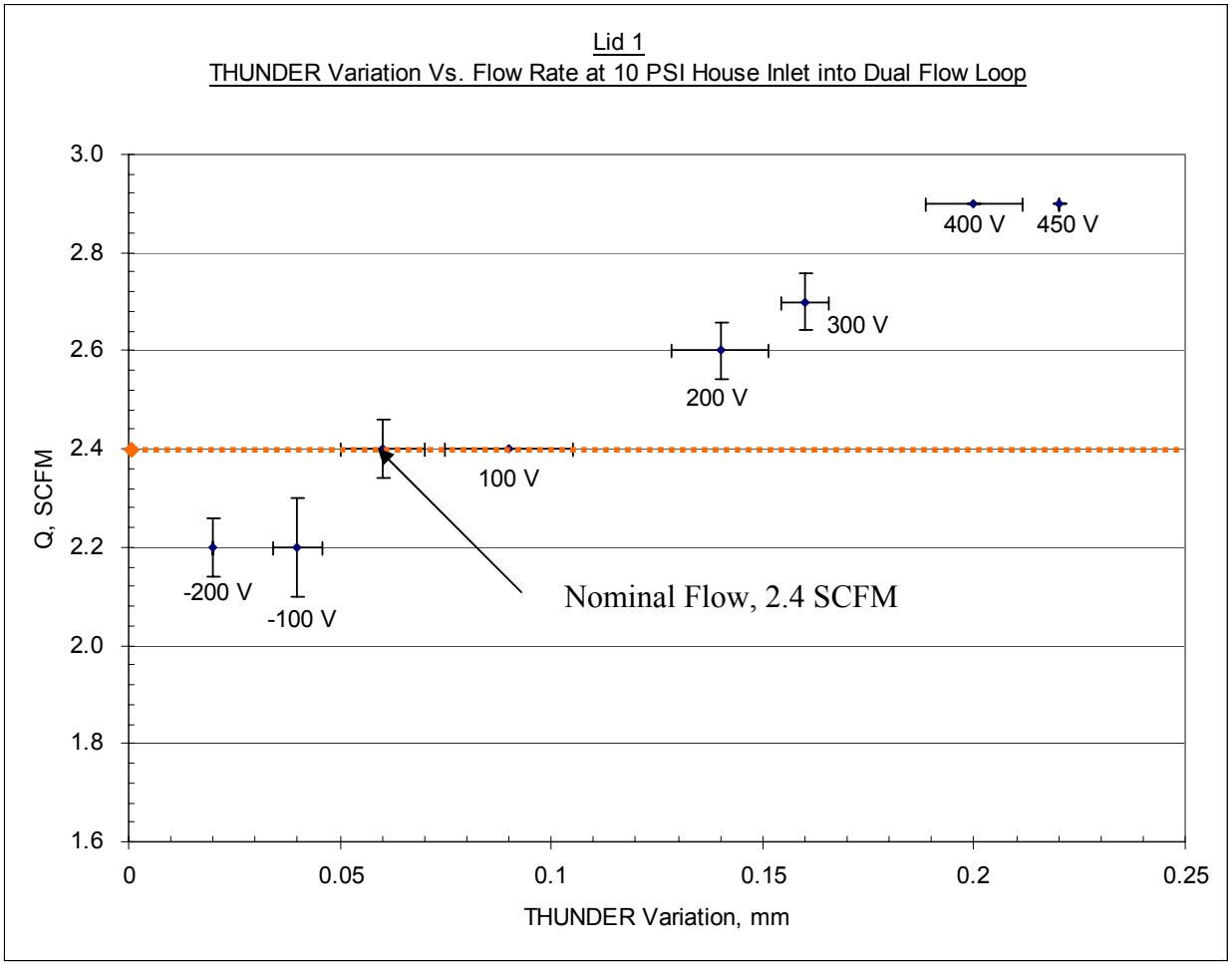

Figure A13. Flow curve for lid 1 at 68.0 SLPM (2.4 SCFM) nominal flow rate, 69.0 kPa (10 PSI) air inlet pressure for dual loop flow (Error bars represent standard deviation from 5 trial sample size).

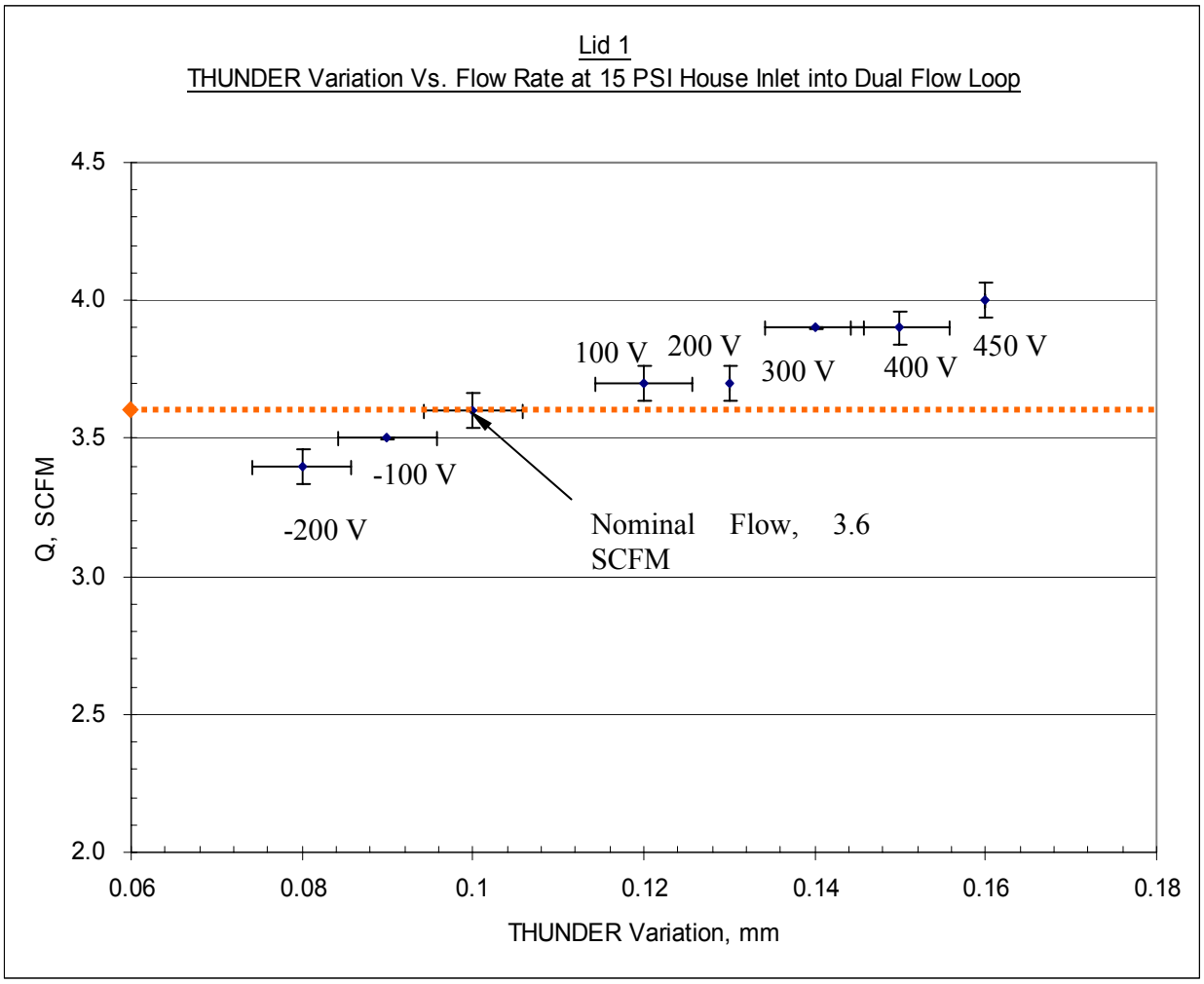

Figure A14. Flow curve for lid 1 at 101.9 SLPM (3.6 SCFM) nominal flow rate, 103.4 kPa (15 PSI) air inlet pressure for dual loop flow (Error bars represent standard deviation from 5 trial sample size).

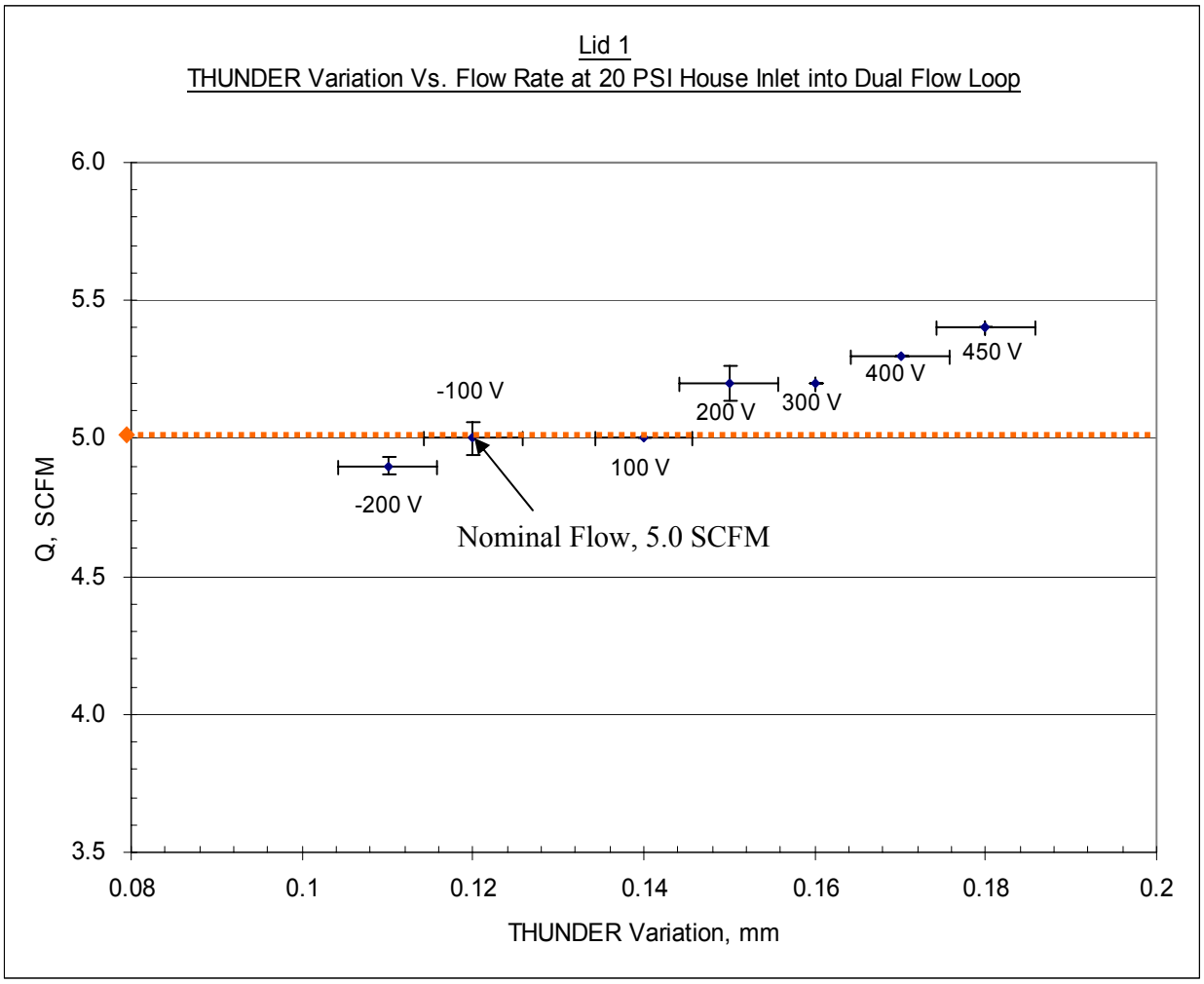

Figure A15. Flow curve for lid 1 at 141.6 SLPM (5.0 SCFM) nominal flow rate, 137.9 kPa (20 PSI) air inlet pressure for dual loop flow (Error bars represent standard deviation from 5 trial sample size).

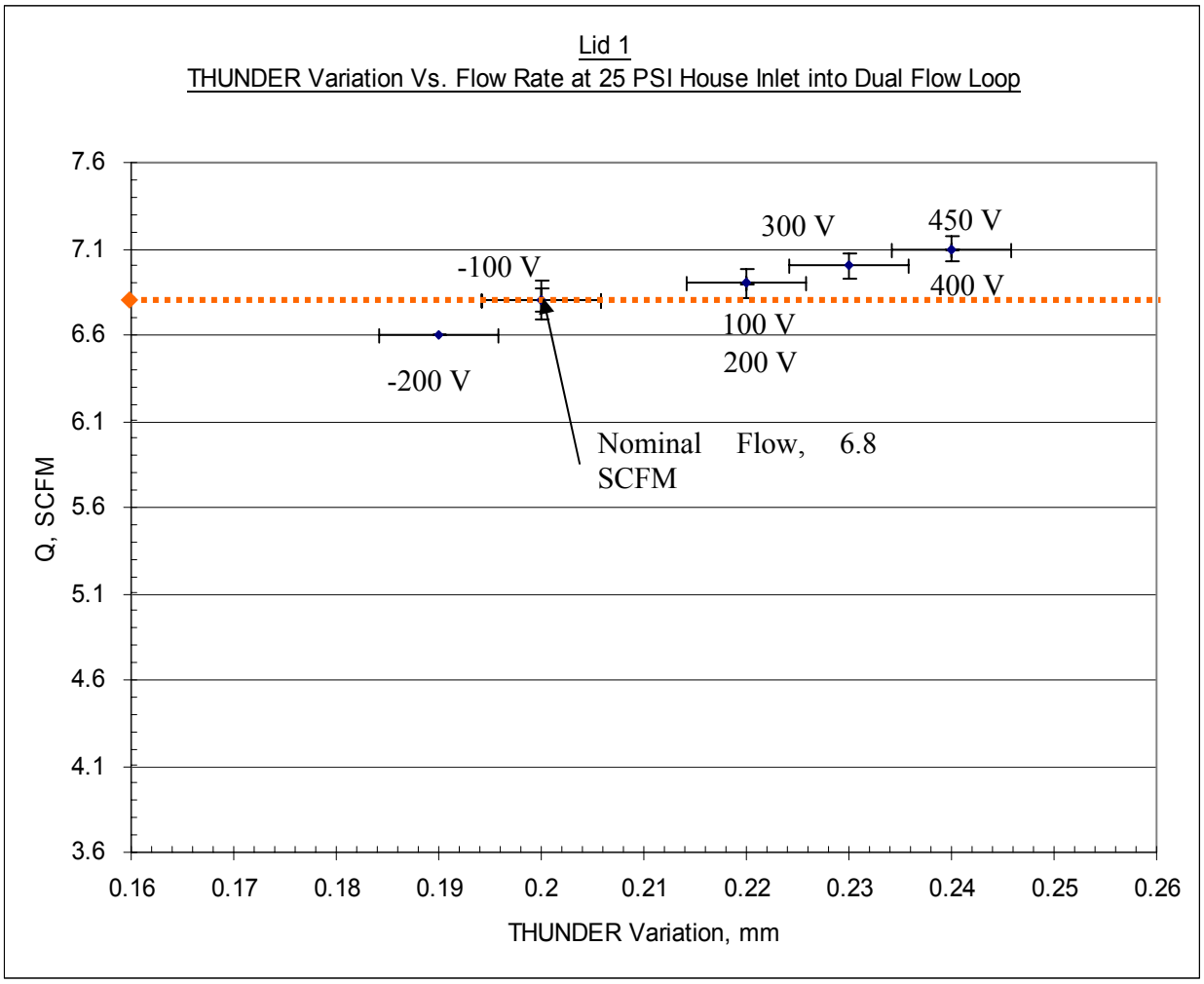

Figure A16. Flow curve for lid 1 at 192.6 SLPM (6.8 SCFM) nominal flow rate, 137.9 kPa (25 PSI) air inlet pressure for dual loop flow (Error bars represent standard deviation from 5 trial sample size).

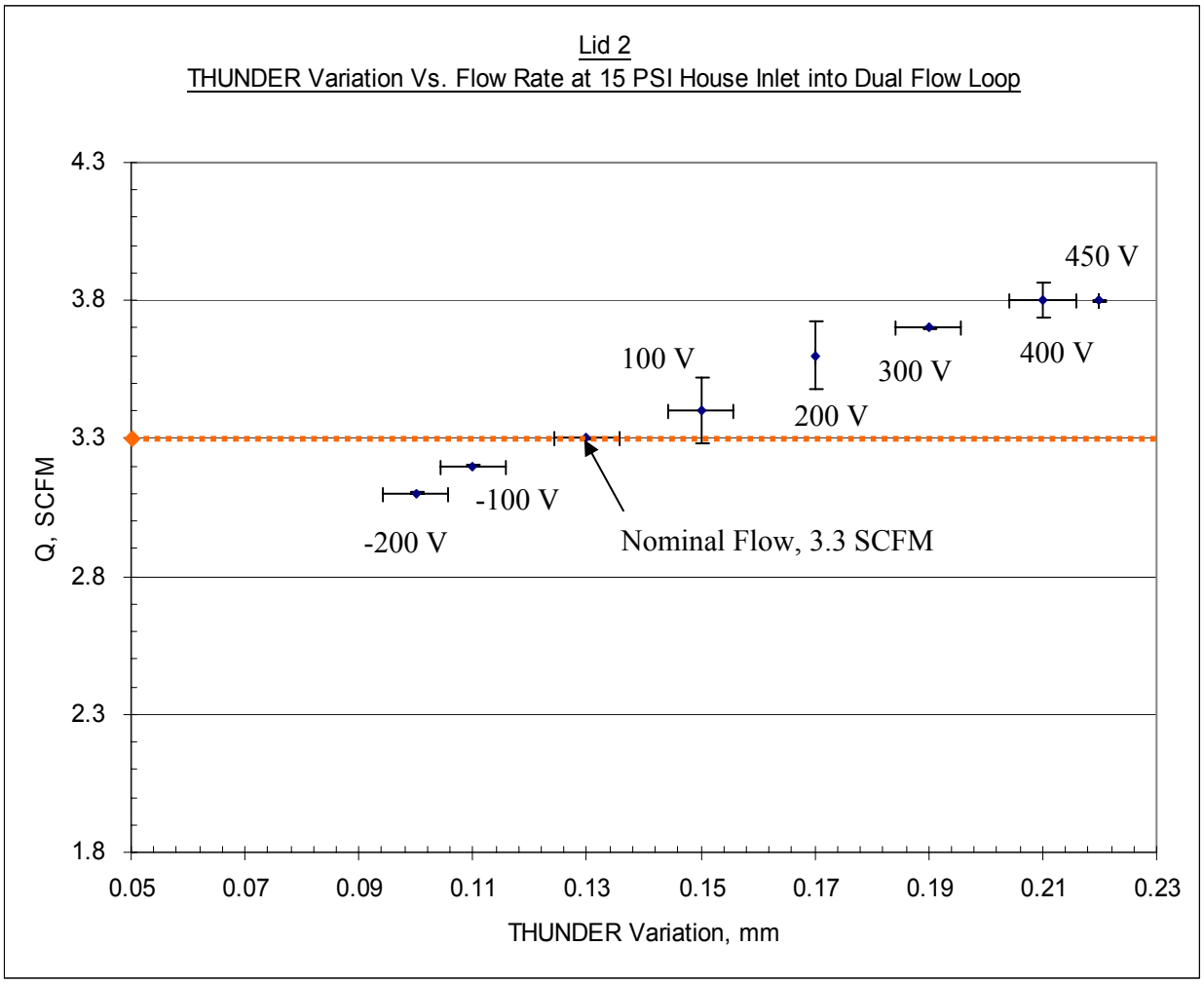

Figure A17. Flow curve for lid 2 at 93.4 SLPM (3.3 SCFM) nominal flow rate, 103.4 kPa (15 PSI) air inlet pressure for dual loop flow (Error bars represent standard deviation from 5 trial sample size).

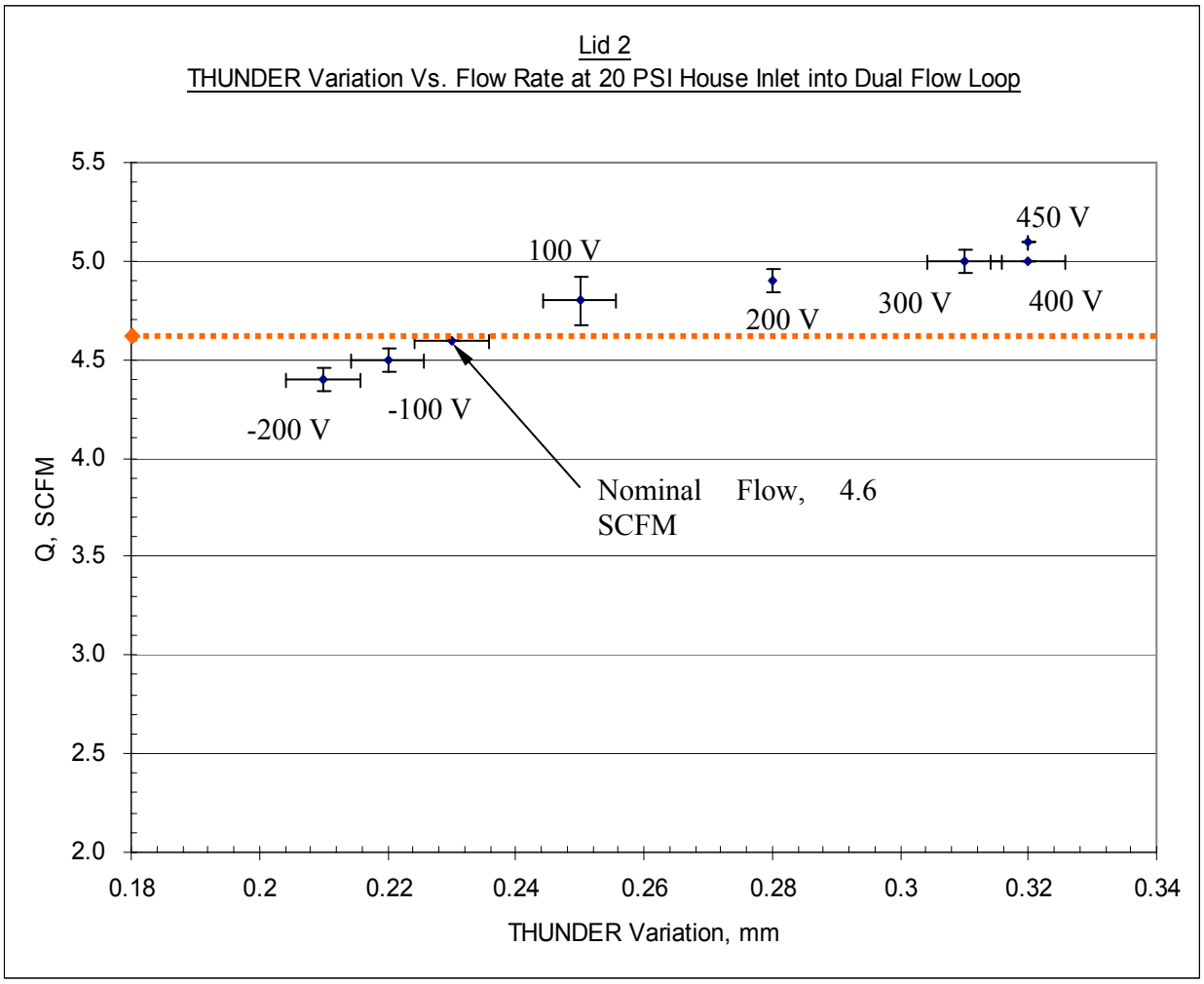

Figure A18. Flow curve for lid 2 at 130.3 SLPM (4.6 SCFM) nominal flow rate, 137.9 kPa (20 PSI) air inlet pressure for dual loop flow (Error bars represent standard deviation from 5 trial sample size).

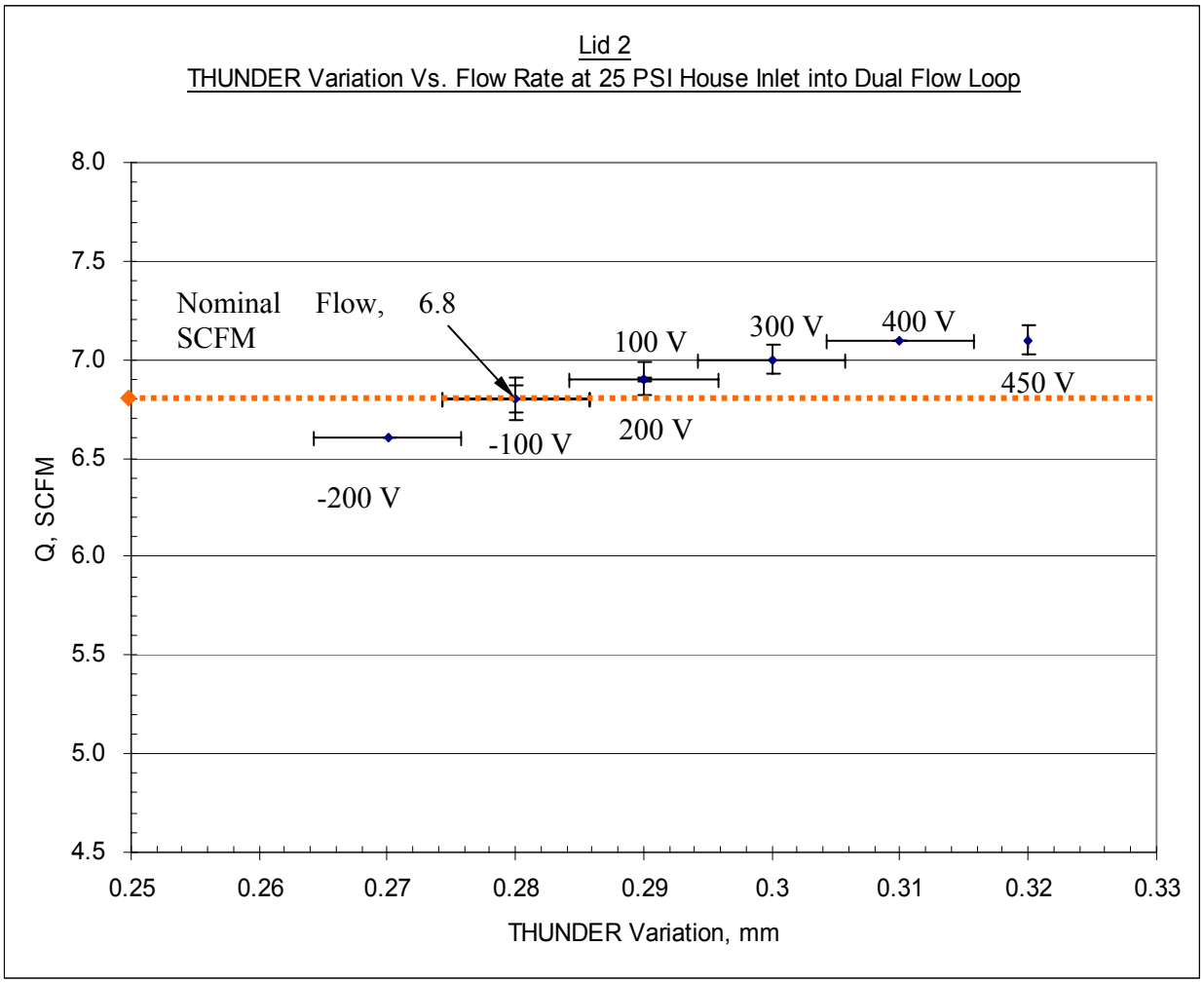

Figure A19. Flow curve for lid 2 at 192.6 SLPM (6.8 SCFM) nominal flow rate, 172.4 kPa (25 PSI) air inlet pressure for dual loop flow (Error bars represent standard deviation from 5 trial sample size).

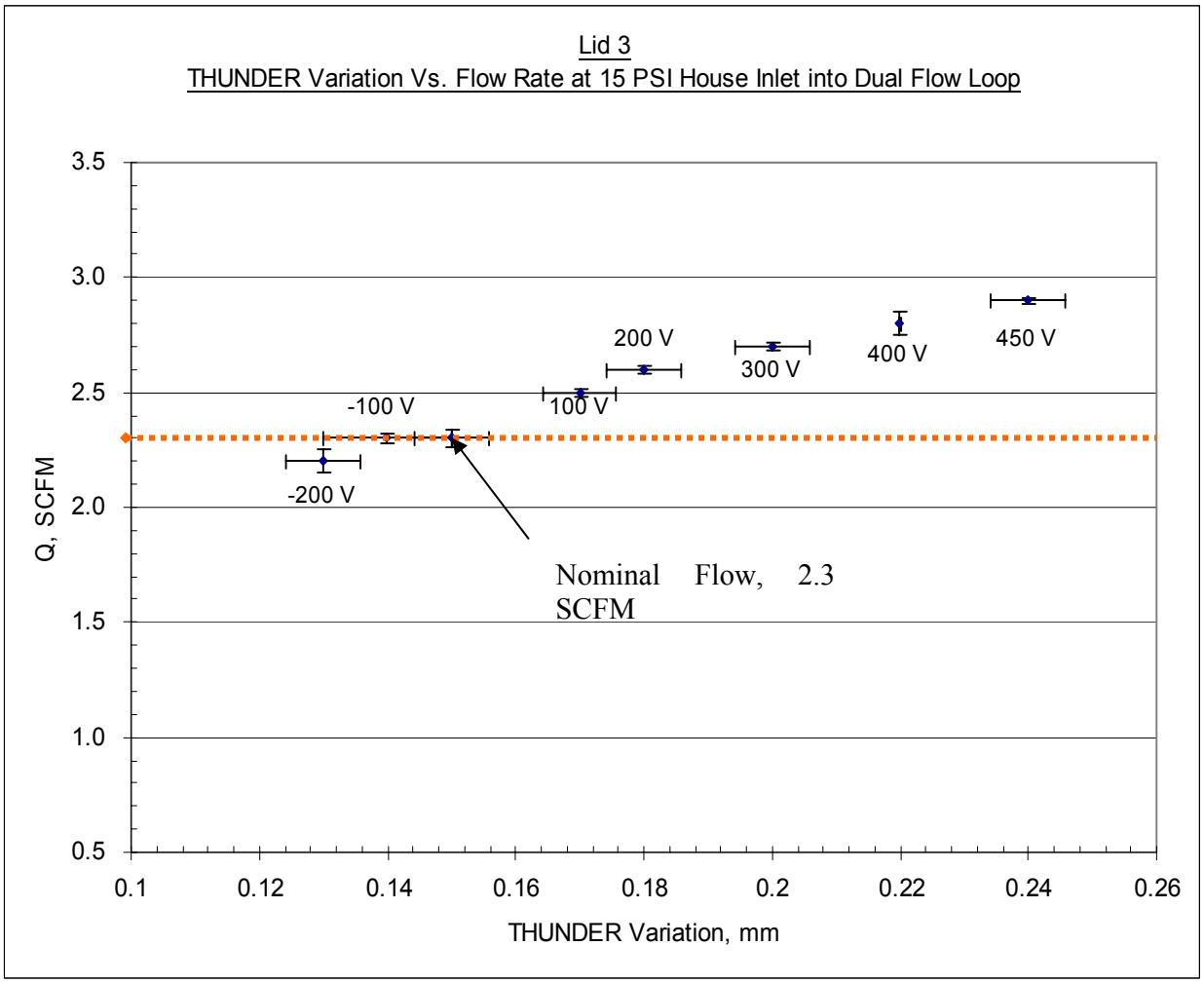

Figure A20. Flow curve for lid 3 at 65.1 SLPM (2.3 SCFM) nominal flow rate, 103.4 kPa (15 PSI) air inlet pressure for dual loop flow (Error bars represent standard deviation from 5 trial sample size).

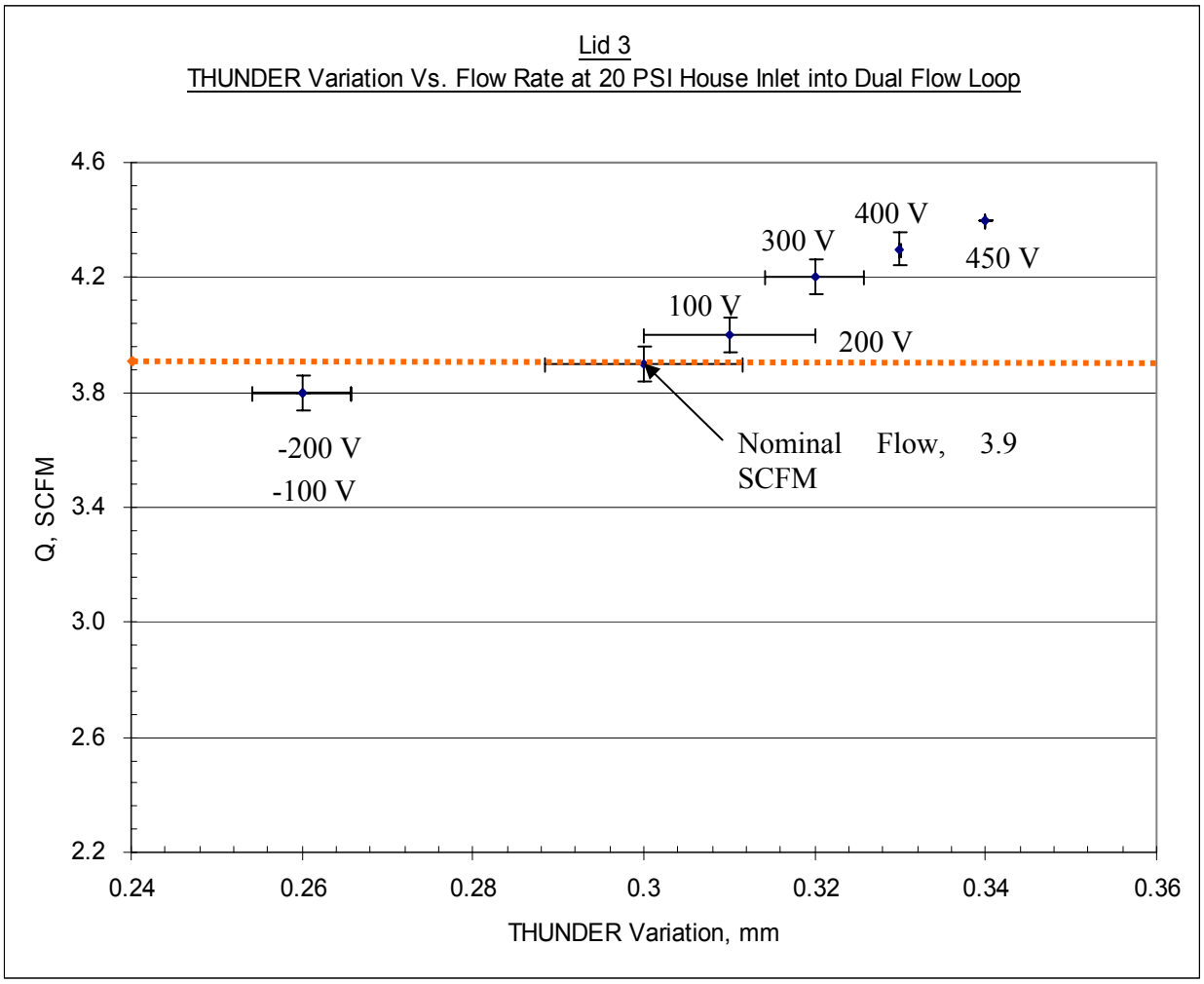

Figure A21. Flow curve for lid 3 at 110.4 SLPM (3.9 SCFM) nominal flow rate, 137.9 kPa (20 PSI) air inlet pressure for dual loop flow (Error bars represent standard deviation from 5 trial sample size).

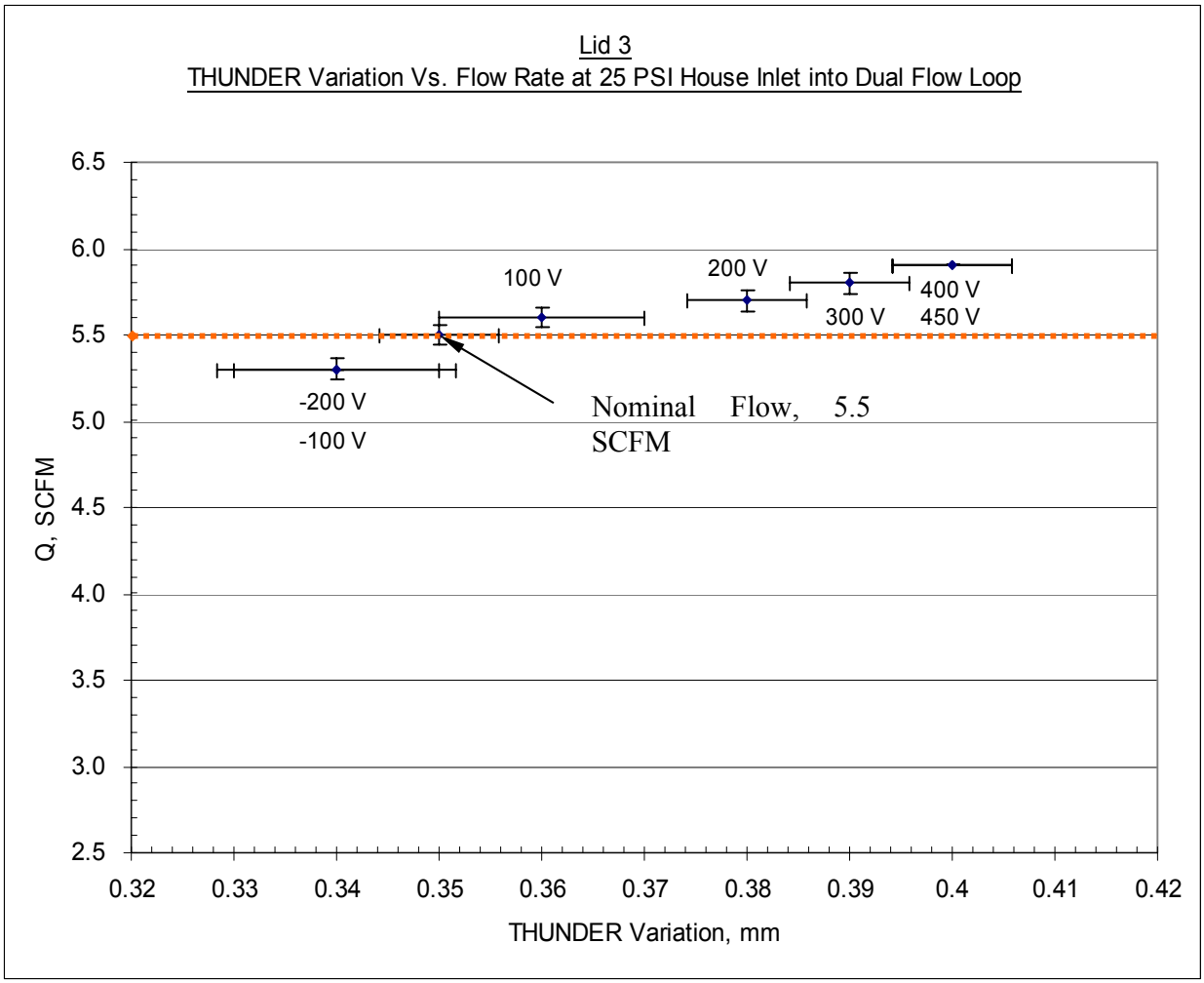

Figure A22. Flow curve for lid 3 at 155.7 SLPM (5.5 SCFM) nominal flow rate, 172.4 kPa (25 PSI) air inlet pressure for dual loop flow (Error bars represent standard deviation from 5 trial sample size).

BIBLIOGRAPHY

1. Allison, S.G., Fox, R.L., Froggatt, M.E., Childers, B.A., "THUNDER piezoelectric actuators as a method of stretch-tuning an optical fiber grating", Proc. of SPIE for Smart Structures and Materials, Vol. 3991, March 2000.

2. Ashford, Gevale R., "THUNDER Actuator", Proc. Of Research Presentations for SCCUR, Cal-Tech, California, 2002.

3. Bouchilloux, P., Letty, R. LE., Lhermet, N., Doucet, E., Lang, M., " Valves Based on Amplified Piezoelectric Actuators", Proc. of 8th International Conference on New Actuators, Actuator 2002, Germany, 2002.

4. Capozzoli, M., Gopalakrishnan, J., Hogan, K., Massad, J., Tokarchik, T., Wilmarth, S., "Modeling Aspects Concerning THUNDER Actuators", Proc. of Industrial Mathematics Modeling Workshop, July 24th, 2000.

5. Cheng, L., Marouze, J. P., "A feasibility study of active vibration isolation using THUNDER actuators", Journal of Smart Materials and Structures, Vol 11, 2002, pp. 854.

6. Clark, William W., Wang, James, "A Piezoelectrically-Actuated Cell Stretching Device", ASB 2000 Annual Conference, ASB, 2000.

7. Dally, James W., Riley, William F., Experimental Stress Analysis, (Third Edition; Knoxville, Tennessee; College House Enterprises, 1991), pp. 164 – 207.

8. Electro-Ceramic Products, EDO Ceramics, "What is Piezoelectricity?", Cooperation Product Literature, Salt Lake City, Utah, 2004.

9. Face International Cooperation, Dr. Alfredo Vazquez Carazo, Thunder White Paper Product Literature, Norfolk Virginia, 2004.

10. Hellbaum, Richard F., Bryant, Robert G., Fox, Robert L., 1995, Thin layer composite unimorph ferroelectric driver and sensor, U.S. Patent No. 5,632,841.

11. Henry, Keith., Nolan-Proxmire, Don., NASA Research Center Public Release No. 96-154, "NASA Rolls Out Award Winning "THUNDER"", Oct 6, 1996.

12. Hyer, M. W., Jilani, A., "Predicting the Deformation of Characteristics of Rectangular Unsymmetrically Laminated Piezoelectric Materials", Proc. of Smart Materials and Structures 2004, Vol. 13, pp 384-392.

13. King Instrument Company, Technical Support Office, Product Literature, Garden Grove, CA, 2004.

14. Lee Company, Chicago Customer Support Office, LFPA Product Literature, Chicago, IL, 2004.

15. Maxtek, Inc., Sales Engineering Support, MV-112 Product Literature, Santa Fe Springs, CA, 2004.

16. Mossi, K. M., Bishop, R. P., "Characterizatioin of Different Types of High Performance THUNDER Actuators", Proc. of SPIE Conference, Newport Beach, CA, March, 1999.

17. Mossi, Karla, Ounaies, Zoubeida, Smith, Ralph, Ball, Brian, "Pre-stressed Curved Actuators: Characterization and Modeling of their Piezoelectric Behavior", Proc. of SPIE for Active Materials, Vol. 5053, 2003.

18. Munday, David, Jacob, Jamey, "Active Control of Separation on a Wing with Conformal Camber", Proc. Of 39th AIAA Aerospace Sciences, Reno, NV, 2001.

19. Ounaies, Z., Mossi, K., Smith R., Bernd, J., "Low-field and High-field Characterization of THUNDER actuators", NASA/CR-2001-210859 ICASE Report No. 2001-9, April 2001.

20. Smith, Ralph C., Ounaies, Zoubeida, "A Domain Wall Model for Hysteresis in Piezoelectric Materials", NASA/CR-1999-209832 ICASE Report No. 99-53, December, 1999.

21. Weinman, Robert, Smith, Ralph C., Kackley, Tyson, Ounaies, Zoubeida, Bernd, Jeff, "Displacement models for THUNDER actuators having general loads and boundary conditions", NASA/CR-2001-211061 ICASE Report No. 2001-25, September 2001.

22. White, Frank M., Fluid Mechanics, 3rd Edition, New Jersey, McGraw-Hill, 1994.

23. Yoon, K. J., Park, K. H., Lee, S. K., Goo, N. S., Park, H. C., "Analytical design model for a piezo-composite unimorph actuator and its verification using lightweight piezo-composite curved actuators", Journal of Smart Materials and Structures, Vol. 13, 2004.